12-2005

Study of The N = 77 Isotones Near The Proton-drip Line; Isomeric Decays of ^{140}Eu, ^{142}Tb, ^{144}Ho, and ^{146}Tm

Mohammed Noor Tantawy
University of Tennessee, Knoxville

To the Graduate Council:

I am submitting herewith a dissertation written by Mohammed Noor Tantawy entitled "Study of The N = 77 Isotones Near The Proton-drip Line; Isomeric Decays of ^{140}Eu, ^{142}Tb, ^{144}Ho, and ^{146}Tm." I have examined the final electronic copy of this dissertation for form and content and recommend that it be accepted in partial fulfillment of the requirements for the degree of Doctor of Philosophy, with a major in Physics.

Carrol R. Bingham, Major Professor

We have read this dissertation and recommend its acceptance:

Lee Riedinger, Witold Nazarewicz, Lawrence Townsend, Krzysztof Rykaczewski

Accepted for the Council:

Carolyn R. Hodges

Vice Provost and Dean of the Graduate School

(Original signatures are on file with official student records.)

To the Graduate Council:

I am submitting herewith a dissertation written by Mohammed Noor Tantawy entitled "Study of The $N = 77$ Isotones Near The Proton-drip Line; Isomeric Decays of ^{140}Eu, ^{142}Tb, ^{144}Ho, and ^{146}Tm." I have examined the final electronic copy of this dissertation for form and content and recommend that it be accepted in partial fulfillment of the requirements for the degree of Doctor of Philosophy, with a major in Physics.

Carrol Bingham

Major Professor

We have read this dissertation
and recommend its acceptance:

Lee Riedinger

Witold Nazarewicz

Lawrence Townsend

Krzysztof Rykaczewski

Accepted for the Council:

Ann Mayhew

Vice Chancellor and Dean of
Graduate Studies

(Original signatures are on file with official student records.)

Study of The $N = 77$ Isotones Near The Proton-drip Line; Isomeric Decays of ^{140}Eu, ^{142}Tb, ^{144}Ho, and ^{146}Tm

A Dissertation
Presented for the
Doctor of Philosophy
Degree
The University of Tennessee, Knoxville

Mohammed Noor Hasan Tantawy
December 2005

Dedication

This dissertation is dedicated to my father, Dr. Hasan M. Tantawy, my mother, Maram J. Belbaisi, and my brothers Engr. Anwar, Dr. Diya, Engr. Saad, Engr. Khalid, Omar, and Abdulrahman as well as my beloved sister Dr. Lara, whom all gave me so much, supported and encouraged me to persevere through life's challenges.

Acknowledgments

First, I am grateful to God for his continuous mercy. Second, I am deeply indebted to my family. Nothing is possible without their support, love and kindness.

I additionally would like to thank my advisors and mentors, Dr. Carrol Bingham and Dr. Krzysztof Rykaczewski for their patience, tolerance and unconditional help. Their willingness to support my work and their guidance throughout my studies has allowed me to develop my skills as a researcher within a supportive team environment. I thank them for that opportunity. I would further like to thank the other members of my committee: Dr. Lee Riedinger, Dr. Witold Nazarewicz, and Dr. Lawrence Townsend. I greatly appreciate their time and input to this dissertation.

I would like to extend my thanks to all those who I have had the honor and privilege to work with at the Holifield Radioactive Ion Beam Facility (HRIBF) as well as at the University of Tennessee, Knoxville. That includes faculty members, students and staff. I would also like to thank the HRIBF staff for providing intense beams of ^{58}Ni and ^{54}Fe.

A special thanks to Dr. John Batchelder, Dr. Wojech Królas, Dr. Robert Grzywacz, and Dr. Andreas Piechaczek for their great help and support over the years. My work would have been a lot harder without them.

The work done in this dissertation was supported by the Joint Institute for Heavy Ion Research which is supported by its members, University of Tennessee, Vanderbilt University and Oak Ridge National Laboratory. ORNL is managed by UT-Battelle, LLC, for the U.S. Department of Energy under Contract No. DE-AC05-00OR22725. The work at the University of Tennessee in Knoxville, Vanderbilt University, Louisiana State University, Georgia Tech, Michigan State University and Mississippi State University was supported by the U.S. D.O.E. through Grants and Contracts No. DE-FG02-96ER40983, DE-FG05-88ER40407, DE-FG02-96ER40978, DE-FG02-96ER41006, DE-AC05-76OR00033.

Finally, I must express my appreciation to the many friends outside of my studies who have helped to relieve the sometimes stressful solitude of graduate school.

Abstract

In this dissertation, the systematics of the $\pi h_{11/2} \otimes \nu h_{11/2}$ and $\pi h_{11/2} \otimes \nu s_{1/2}$ isomeric configurations were studied for the odd-Z, $N = 77$ isotones near the proton drip line. The isomeric decays in ^{140}Eu, ^{142}Tb, ^{144}Ho and ^{146}Tm were measured by means of X-ray, γ-ray and charged particle spectroscopy at the Recoil Mass Spectrometer at the Holifield Radioactive Ion Beam Facility (HRIBF) at Oak Ridge National Laboratory (ORNL). The spin and parity of $I^\pi = 8^+$ and 5^- were deduced for the isomers in ^{140}Eu and ^{142}Tb. New decay schemes were established, and the half-lives of the 8^+ isomers were measured to be 302(3) ns for ^{140m2}Eu and 25(1) μs for ^{142m2}Tb. No evidence for the expected 1^+ ground-state was found in the ^{144}Ho decay data.

The proton emission from ^{146}Tm was restudied. Five proton transitions were assigned to two proton emitting states. The half-lives of 198(3) ms and 68(3) ms and the spin and parity values of $I^\pi = 10^+$ and 5^- were established for ^{146m}Tm and ^{146gs}Tm, respectively. For the first time for an odd-odd nucleus, the interpretation of the observed decay properties and structure of the proton-emitting states was made by accounting for deformation and proton and neutron coupling to the core excitations. A complex wave function structure was obtained, with dominating components of $\pi h_{11/2} \otimes \nu h_{11/2}$ for the 10^+ isomer and $\pi h_{11/2} \otimes \nu s_{1/2}$ for the 5^- ground state.

Details of the experimental setup and results as well as a brief description of the detectors used in the experiments and the HRIBF facility will be discussed in this dissertation.

Contents

List of Tables

List of Figures

Chapter 1

Introduction

The presence of excited isomeric states in atomic nuclei is a sign of γ-decay hindrance. The isomerism of a state is caused by the absence of energetically available states with large decay probability. Isomeric decays sometimes require a major rearrangement of nucleons, and in extreme cases it can lead to β or particle decay. Thus, the isomers are signatures of major structure changes within the nucleus. Their presence enables detailed experimental study since the stop-over in the prompt decay path allows the use of very selective time delayed correlation/tagging techniques. Isomeric states in the $N = 77$ region are a result of the high-j states that involve the $h_{11/2}$ intruding proton orbital and their associated high multipolarity decays [1].

The isomeric states in the $N = 77$ region most likely originate from the coupling of the $h_{11/2}$ proton to the $s_{1/2}$, $d_{3/2}$ and $h_{11/2}$ neutrons. The large spin values and the large spin and small energy differences between the $\pi h_{11/2} \otimes \nu h_{11/2}$ and $\pi h_{11/2} \otimes \nu s_{1/2}$ create a favorite condition for isomers to occur.

For the odd-odd $N = 77$ isotone ^{146}Tm, two proton-radioactive states are known and both exhibit fine structure in the proton emission spectra [8, 16, 17]. However, there was an ambiguity in the spin and configuration assignment and even the possibility of a third proton emitting state was considered [8]. We have restudied the decay of ^{146}Tm establishing the half-life of the 1.016 MeV proton transition and determining its origin.

The interpretation of the structures of proton-emitting nuclei often suffer from the lack of data on nuclei next to the proton drip line. In order to better understand the systematic trends of the proton-neutron states around the proton drip line, we have studied the $N = 77$ even-mass isotones next to ^{146}Tm, namely ^{144}Ho, ^{142}Tb, and ^{140}Eu (see Fig. 1.1 for previous information from the literature [1–12] and this work).

I was involved in setting up the experiments needed to study the $N = 77$ odd-Z isotones near the proton-drip line at the HRIBF. Once the data were collected, I analyzed them and the following points were determined through this analysis:

1. The observation of a new isomer, ^{140m2}Eu. The half-life of 302(3) ns, the decay scheme of this isomer, and the spins and parities of most of its levels were determined.

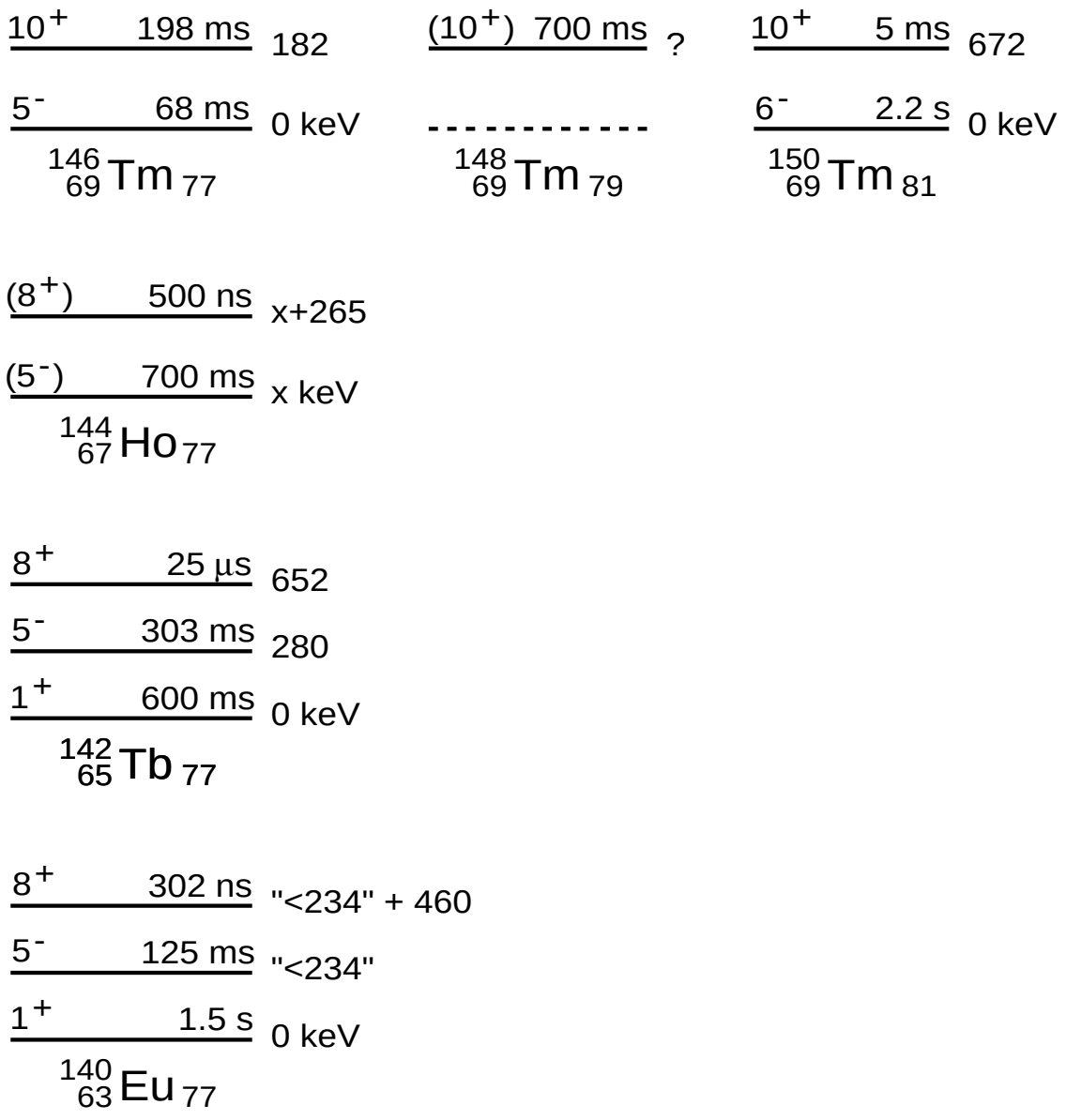

Figure 1.1: Systematics of the $\pi h_{11/2} \otimes \nu h_{11/2}$ and the $\pi h_{11/2} \otimes \nu s_{1/2}$ states in the $N = 77$ odd-Z isotones and $Z = 69$ odd-N thulium isotopes around the proton-drip line. The spin and parity assignments are from this work and from the literature [1–12].

2. The measurement of a new half-life of 25(1) μs for ^{142m2}Tb and the observation of new transitions deexciting ^{142m2}Tb.

3. The measurement of the conversion coefficients of most of the transitions deexciting ^{142m2}Tb and ^{142m1}Tb using an electron detector. The spins and parities of all the levels in ^{142}Tb up to ^{142m2}Tb were established.

4. The determination of the origin of the once ambiguous 1.016 MeV proton line emitted from ^{146}Tm by measuring its half-life.

At the end, I drew conclusions about the evolution of the $\pi h_{11/2} \otimes \nu h_{11/2}$, $\pi h_{11/2} \otimes \nu s_{1/2}$, and the $\pi s_{1/2} \otimes \nu s_{1/2}$ orbitals with mass. While the $I^{\pi} = 1^{+}$ state exists as the ground state in some of the nuclei in the $N = 77$ odd-Z region near the proton drip line, our data gives no evidence for it near the proton drip line, specifically in ^{144}Ho and ^{146}Tm. I will discuss in this dissertation why this happens.

Beams of ^{58}Ni and ^{54}Fe, targets of ^{92}Mo, efficient separators with increased selectivity for evaporation residues, large detector arrays to count rare signals of very exotic nuclei, and signal processors were all utilized in order to achieve the results we obtained at the HRIBF discussed in this dissertation.

Chapter 2

Decay Processes of the Nucleus

Short lived nuclear ground states and isomeric states have been studied for over 40 years. Information on the evolution of shell structure and the nuclear mean field especially at large isospin values can be obtained from the study of the properties of isomeric states in nuclei far from stability. In particular the onset of deformation in these nuclei can be researched.

An unstable nucleus deexcites through one or a combination of the following ways: alpha (α), beta (β), gamma (γ), proton or neutron emission, or via fission. Some of these decay processes will be described below.

2.1 Gamma Decay and Internal Conversion

A nucleus in an excited state will emit one or more γ rays if no other competing decay process takes over. The emission of γ rays allows the excited state(s) to deexcite to the ground state with energies ranging from ~ 0.1 keV up to 10 MeV depending on the energy difference between the nuclear states. The emitted wavelengths of these γ-rays range from 10000 to 100 fm. Gamma rays travel through air with negligible absorption and scattering due to the fact that they are neutrally charged electromagnetic radiation. Gamma ray radiation is easy to observe using the proper detectors such as gas filled detectors, plastic scintilators, or semiconductor detectors such as the Ge clover detectors used at the Holifield Radioactive Ion Beam Facility (HRIBF). The γ-ray energies can be measured with high accuracy and they can be used to determine excited states. This precision makes the study of γ-ray emission a standard technique of nuclear spectroscopy.

When emitting a γ-ray, the nucleus recoils with a momentum equal and opposite to that of the γ-ray. The energy at which the γ-ray is emitted can be calculated using the simple approximation

$$E_\gamma \approx \Delta E - \frac{(\Delta E)^2}{2Mc^2} \tag{2.1}$$

where ΔE is the difference between the initial and final states of the nucleus in MeV, and Mc^2 is the nucleus rest energy and is on the order of $A \times 10^3$ MeV, where A is the mass number of the nucleus.

Gamma rays can be characterized in terms of the electric and magnetic multipoles. The most common multipoles are the dipoles, which are represented by the Legendre polynomial $P_1 = cos\theta$, and the quadrupoles, $P_2 = (3cos^2\theta - 1)/2$. Weisskopf estimates are used as a guide to the transition probabilities of the multipole orders. Since in the field of intermediate energy nuclear physics we usually concentrate on the low spin states, the electric and magnetic lower order multipoles are most important. The estimated transition probabilities of these lower order multipoles are given by

$$\begin{aligned}
\lambda(E1) &= 5.625X10^{13}A^{2/3}E^3 \\
\lambda(E2) &= 4.672X10^{7}A^{4/3}E^5 \\
\lambda(E3) &= 23.61A^{2}E^7 \\
\lambda(E4) &= 8.08X10^{-6}A^{8/3}E^9 \\
\lambda(M1) &= 3.15X10^{13}E^3 \\
\lambda(M2) &= 2.24X10^{7}A^{2/3}E^5 \\
\lambda(M3) &= 11.11A^{4/3}E^7 \\
\lambda(M4) &= 3.3X10^{-6}A^{2}E^9
\end{aligned} \tag{2.2}$$

where λ is the decay constant of the excited state times the branching ratio for decay by that decay channel [18]. E_L signifies electric radiation and M_L magnetic radiation where L gives the angular momentum of the γ-ray. The lower multipoles have higher rates and the electric transitions for a given L are faster than the magnetic ones. The partial half-lives of the emitted γ-ray transitions can be obtained by using $T_{\frac{1}{2}} = 0.693/\lambda$. The parity ($\pi$) of the radiation field is given by

$$\pi(EL) = (-1)^L \tag{2.3}$$

$$\pi(ML) = (-1)^{L+1}. \tag{2.4}$$

The Weisskopf estimates are not true theoretical calculations. Hence they are not to be compared with measurements but rather to provide us with reasonable comparisons of the transition rates or multipolarities. The Weisskopf estimates for E2 transition rates are an order of magnitude less than the real experimental rates [19]. Often, Weisskopf estimates are based on the assumption that the motion of a single nucleon is responsible for the transition. E2 transitions between collective states give the enhancement. On the other hand, E1 transitions do not show similar behavior and are generally slower than the single-particle rates [19]. Higher transitions such as M4 transitions are usually in excellent agreement with the Weisskopf estimates.

The angular momentum and parity of the nuclear states are constrained by the following selection rules:

$$|I_i - I_f| \leq L \leq I_i + I_f \tag{2.5}$$

$$\Delta\pi = \text{no: even electric, odd magnetic} \tag{2.6}$$

$$\Delta\pi = \text{yes: odd electric, even magnetic} \tag{2.7}$$

where $L \neq 0$ because monopole radiation does not occur. Hence, a γ-ray cannot be emitted from a 0^+ excited state to a 0^+ ground state. Instead, internal conversion takes over in this case and an orbital electron is ejected with a multipolarity of E0. At lower energies, internal conversion competes with γ-ray emission allowing us to deduce the spins and parities of the nuclear states. Internal conversion occurs when the electromagnetic fields of the nucleus interact with atomic electrons. The nucleus transfers enough energy to one orbital electron to eject it from the atom. The electron will carry an energy of $T_e = \Delta E - B_e$ where ΔE is the energy emitted from the nucleus and B_e is the binding energy of the electron and is a positive quantity. The internal conversion process has a threshold equal to the electron binding energy in a certain shell labeled K, L, M ...etc. The internal conversion process produces a discrete energy spectrum and not a continuous one. The ratio of the conversion electron and γ-ray emission probabilities is given by:

$$\alpha = \lambda_e / \lambda_\gamma. \tag{2.8}$$

These internal conversion coefficients can be calculated using the following equations

$$\alpha(EL) \approx (\frac{1}{137})^4 (\frac{Z^3}{n^3})(\frac{L}{L+1})(\frac{2m_e c^2}{E})^{L+\frac{5}{2}} \tag{2.9}$$

$$\alpha(ML) \approx (\frac{1}{137})^4 (\frac{Z^3}{n^3})(\frac{2m_e c^2}{E})^{L+\frac{3}{2}}.$$

In practice, when an electron conversion detector such as the bellows electron spectrometer for the cards array (BESCA) is deployed, a measurement of the K/L ratios of the converted electrons as well as a measurement of the K and L conversion coefficients and even in some cases the M conversion coefficients can be determined. Determining the M conversion coefficients requires high detector resolution as the energy (T_M) is very close to that of the γ-ray energy itself and higher shell conversion lines. The K and L electron conversion coefficients, α_K and α_L, respectively, can be determined by dividing the number of counts in the K-electron peak or the L-electron peak by the number of counts in their corresponding γ-ray peak. The efficiency of the conversion electron detector and the γ-ray detector(s) must be taken into account by dividing the counts by the efficiency. In mathematical form this is:

$$\alpha_K = \frac{(C_K / eff_{besca})}{(C_\gamma / eff_\gamma)} \tag{2.10}$$

where C_K is the area of the K electron peak for a particular γ-ray, C_γ is the area of the γ-ray peak, eff_{besca} is the detection efficiency of BESCA at the K electron energy, and eff_γ is the gamma detector efficiency at the γ-ray energy. The same can be done for α_L and α_M.

Since an orbital electron is knocked out of its orbit, the atom fills the vacancy with electrons occupying the upper levels of the atom, and characteristic X-rays are emitted. If an X-ray detector is employed when studying γ-ray spectroscopy, the identification of the nucleus can be established from its characteristic X-rays. One can also determine the internal conversion coefficient experimentally by gating on a certain γ-ray energy that is in coincidence with one other γ-ray and then comparing the X-ray intensity to the γ-ray intensity in that gate. One has to normalize the number of counts in the X-ray peak and the number of counts in the γ-ray peak by dividing by the detector efficiency at each energy. Furthermore, one must divide the X-ray peak area by the fraction of K-shell vacancies that produce the X-ray. A good approximation of the multipolarity of the transition can be deduced from α_K measured in this way.

Another method of measuring the electron conversion coefficient without an electron spectrum is by comparing the γ-ray intensity of two subsequent γ-ray transitions. Suppose γ_1 feeds γ_2 in a decay scheme with no other transition in or out of the intermediate state. If the total electron conversion coefficients, $\alpha_{tot} = \alpha_K + \alpha_L + \alpha_M$ ...etc, is known for γ_2, for example, then the total electron conversion coefficient for γ_1 can be found via the equation

$$I_1(\alpha_{tot1} + 1) = I_2(\alpha_{tot2} + 1), \tag{2.11}$$

where I is the γ-ray intensity measured by dividing the area of the γ-ray peak by the γ-ray detector efficiency at that particular energy. This method of determining the electron conversion coefficient is not as precise as the previous two methods since it depends on the knowledge of the total conversion coefficient of one of the γ-rays and there is the possibility that weak transitions populating or depopulating the level are not observed. One can estimate the electron conversion coefficient of the first γ-ray if only α_K of the second γ-ray is known.

2.2 Proton Radioactivity

Study of proton radioactivity started more than 30 years ago by Jackson [20] with the discovery of the proton emitting isomer ^{53m}Co. The study of proton radioactivity provides unique information on the structure of nuclei far from stability [21–23] located in the proton drip-line region, see Fig. 2.1. The study of nuclei beyond the proton drip-line can test nuclear structure models and perhaps detect the effects of coupling to unbound continuum states which would modify the nuclear wave functions. Despite the instability of nuclei beyond the proton drip-line towards proton emission, these nuclei can still be studied experimentally. This is due to that fact that the proton has to penetrate the combined potential of the Coloumb barrier and centrifugal potential which makes the nuclear life time long enough to permit the detection of emitted protons. The rate at which the proton is emitted from the parent nucleus depends on the decay energy of the proton, its angular momentum and the

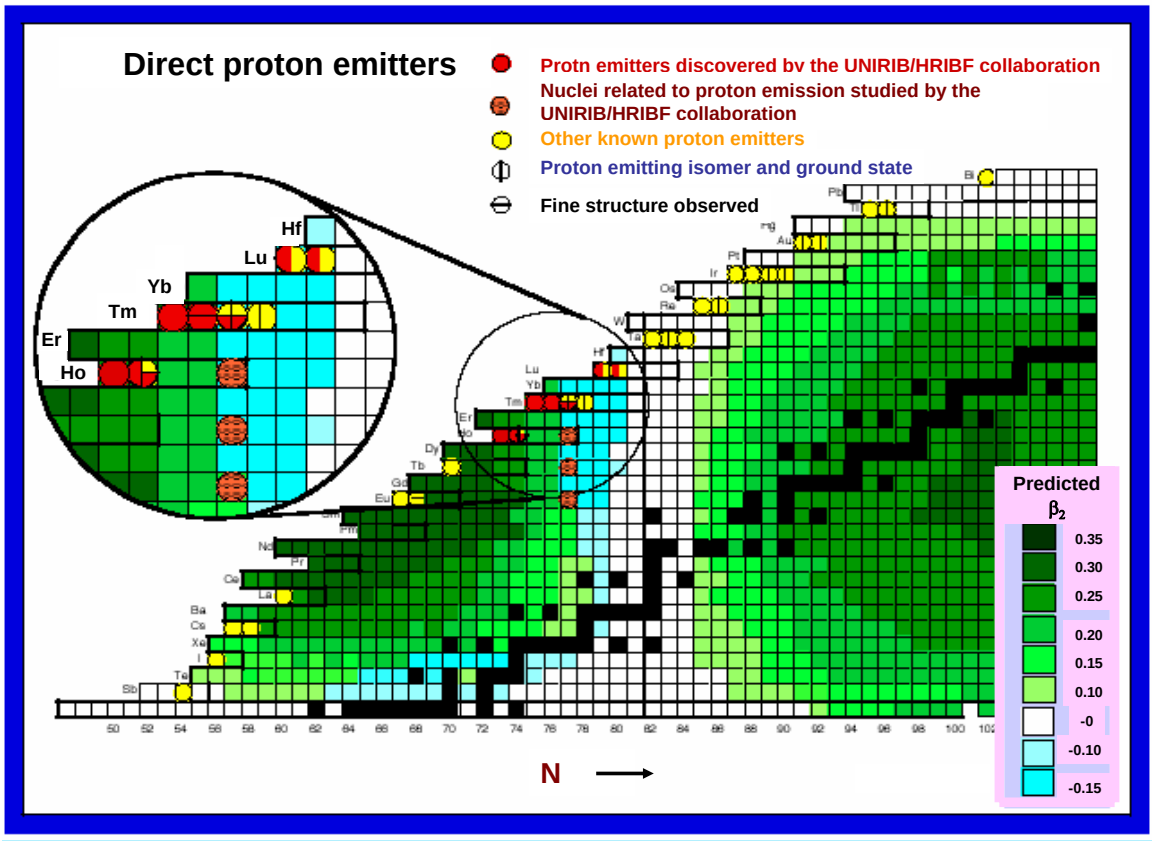

Figure 2.1: Portion of the nuclear chart showing some of the most recently studied nuclei near the proton-drip line.

deformation of the nuclear potential [24]. Proton radioactivity studies provide information on the wave functions of the parent state through the simple WKB relationship between its angular momentum, decay energy, and half-life, see next section. By measuring the decay energies of the emitted protons and their partial half-lives, we can determine and understand the relative energies, spins, and parities of single-particle proton orbitals beyond the proton drip-line, especially for spherical nuclei [25, 26].

The measurement of the proton energy gives a direct test of mass formulas at the limits of nuclear existence and enables improvements to the mass models. The proton must have sufficient energy to tunnel through the Coloumb barrier, and the orbital angular momentum barrier if it is not an $\ell = 0$ proton. The Coloumb barrier is proportional to the charge of the tunneling particle, while the orbital angular momentum term is inversely proportional to the mass. Consequently, the orbital angular momentum part is relatively more important in determining the decay rate for proton radioactivity than for α decay. For this reason, it is usually possible to identify the orbital angular momentum of the emitted proton, and thus, for regions where the spherical shell model is appropriate, the shell model wave function can be investigated.

Fine structure in proton radioactivity results from proton emission of the parent nucleus to an excited state in the daughter nucleus. The observation of fine structure in proton emission from odd-A nuclei provides another access point to nuclear structure information and allows for a more detailed description of the emitting state's wave function [27, 28]. So far, fine structure has been observed in a small number of nuclei. The first observation of fine structure was in the decay of highly deformed ^{131}Eu [29]. The first observation of fine structure from a transitional odd-A nucleus was done later at the HRIBF in the study of ^{145}Tm [24]. Fine structure was also observed in ^{141}Ho [15]. Studies done at the HRIBF allowed the first observation of fine structure of an odd-odd proton emitter, namely ^{146}Tm [8, 17] which is one of the main topics of this dissertation.

The energy and angular momentum of the emitted proton strongly influences the probability of tunneling through the barrier. If a state emits two protons with different energies but comparable intensities then the energy difference is compensated by a difference in the proton orbital angular momentum arising from different components of the emitting state. This leads to a mixed wave function of the proton emitting state. Long lived isomeric states in nuclei with potential proton emission possibilities, β-decay represents a substantial part of the decay width, while for shorter lived ground states, proton emission dominates [8], see the discussion on ^{146}Tm in section 6.4.

Chapter 3

The Holifield Radioactive Ion Beam Facility

At the HRIBF, radioactive nuclei for decay studies are produced with fusion-evaporation reactions of heavy ions plus stable targets. The nuclei are then isolated and separated using one of the mass separation stations at the HRIBF, see Fig 3.1, and are implanted into a detector, moving tape collectors (MTCs), or collection foils. The layout of the acceleration process is shown in Fig 3.2. The way beams are produced and delivered to the experimentalist at the end stations at the HRIBF is as follows (see Fig. 3.2):

1. High intensity proton, deuteron, and alpha particle beams are provided by the Oak Ridge Isochronous Cyclotron (ORIC) [30]. The particles are deflected and extracted from the cyclotron by a series of magnetic and electric components.

2. The beam extracted from ORIC bombards a thick target located at the beginning of a high voltage platform, +300 keV relative to the ground called, the Radioactive Ion Beam RIB Injector. The bombardment of the target leads to the production of radioactive nuclei. The target material depends on the type of radioactive nuclei desired for a specific experiment.

3. Once the radioactive nuclei are produced at the target chamber, they are evaporated and transported to the ion source via a Ta tube where a high electrical current flows through the tube heating it to very high temperatures, reaching up to 1800 ^oC [30].

4. At the ion source chamber, the radioactive nuclei are ionized to positively charged ions via a high temperature and high efficiency Electron-Beam-Plasma Ion Source (EBPIS). The ion source chamber itself is at a +60 keV voltage relative to the rest of the assembly in the high voltage platform. This pushes the positive ions toward the mass/isotope separator.

5. The different ions are separated isotopically in a mass/isotope separator. This is the first stage of mass separation.

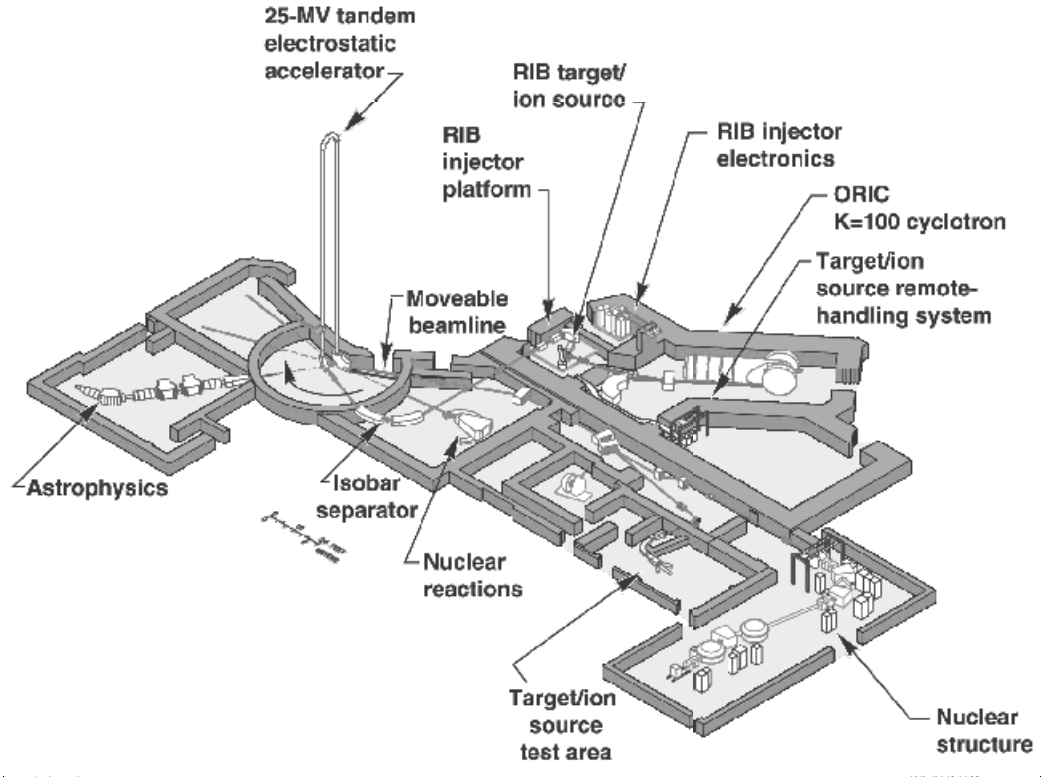

Figure 3.1: The Holifield Radioactive Beam Facility (HRIBF) at Oak Ridge National Laboratory (ORNL).

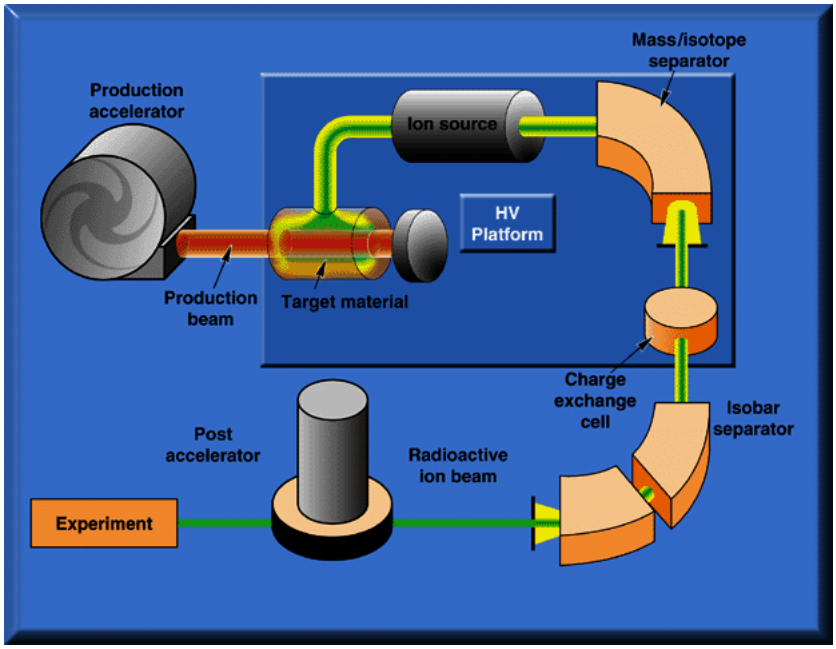

Figure 3.2: Schematic display of beam generation tools at the HRIBF.

6. The tandem accelerator is designed to accelerate negatively charged ions. Therefore, after the first stage of mass separation, the positively charged ions gain electrons in the the charge exchange cell (CEC) and become negatively charged. This is done when the positive ions collide with a collision vapor of thickness $\approx 10^{15}$ atoms/cm^2 in the CEC allowing multiple collisions [30] as displayed in the following reactions:

$$X^+(fast) + V \rightarrow X^0(fast) + V^+ \tag{3.1}$$
$$X^0(fast) + V \rightarrow X^-(fast) + V^+ \tag{3.2}$$

   where X^+ is a positive atomic RIB and V is the collision vapor. An off-axis Faraday cup is used to measure the intensity of the resulting negative ions.

7. Once the negatively charged radioactive ions leave the CEC, they go through a second stage of mass separation just outside the high voltage RIB injector platform. In the mass separators, the ions are separated according to their mass to charge ratios.

8. The desired RIB is finally injected into the 25 MV tandem.

The tandem accelerator [30] is a long column consisting of 27 conducting units, a 180 degree bending magnet, high energy and low energy acceleration tubes, three quadrupole lenses, three sets of steerers, and two charge strippers, see Fig 3.3. The column is placed in a 100 ft high, 33 ft wide pressurized vessel filled with SF_6 gas during operation to prevent sparking of the tandem with the steel walls of the vessel. Each of the conducting units can withstand one million volts. The total voltage on the high voltage terminal can reach 25 MV, the highest in the world.

Since the top of the tandem is always positively charged up to +25 MV, the negative ions coming out of the charge exchange cell are accelerated upwards. They then bombard a thin ^{12}C foil, < 10 μg/cm^2, and are stripped of their negative charge to become positive RIBs with a distribution of charge states. The 180^o bending magnet is used to select the most probable charge state (Q) of these positive RIBs. For example, $A/Q = 58/11$ is chosen at that point when accelerating ^{58}Ni beams. The positive RIBs gain acceleration going down the tandem due to the Coloumb repulsive force with the positively charged top of the Tandem. Because of the large Q, the beam gains more energy traveling down the tandem than traveling upwards. A second stripper can be used on the way down if higher charge states are needed for experiments desiring higher energies, but that will be at the price of loosing part of the beam intensity (beam current) since the the incoming beam will be distributed over a range of charge states. Finally, the resulting radioactive ions are delivered to the end stations. The tandem has the capability of accelerating masses up to $A = 80$ to energies above the Coloumb barrier.

3.1 The Recoil Mass Separator (RMS)

The RMS is a 25 m long, zero degree, device used to separate masses produced in nuclear reactions. It is mainly an assembly of a momentum separator for beam rejection and electric

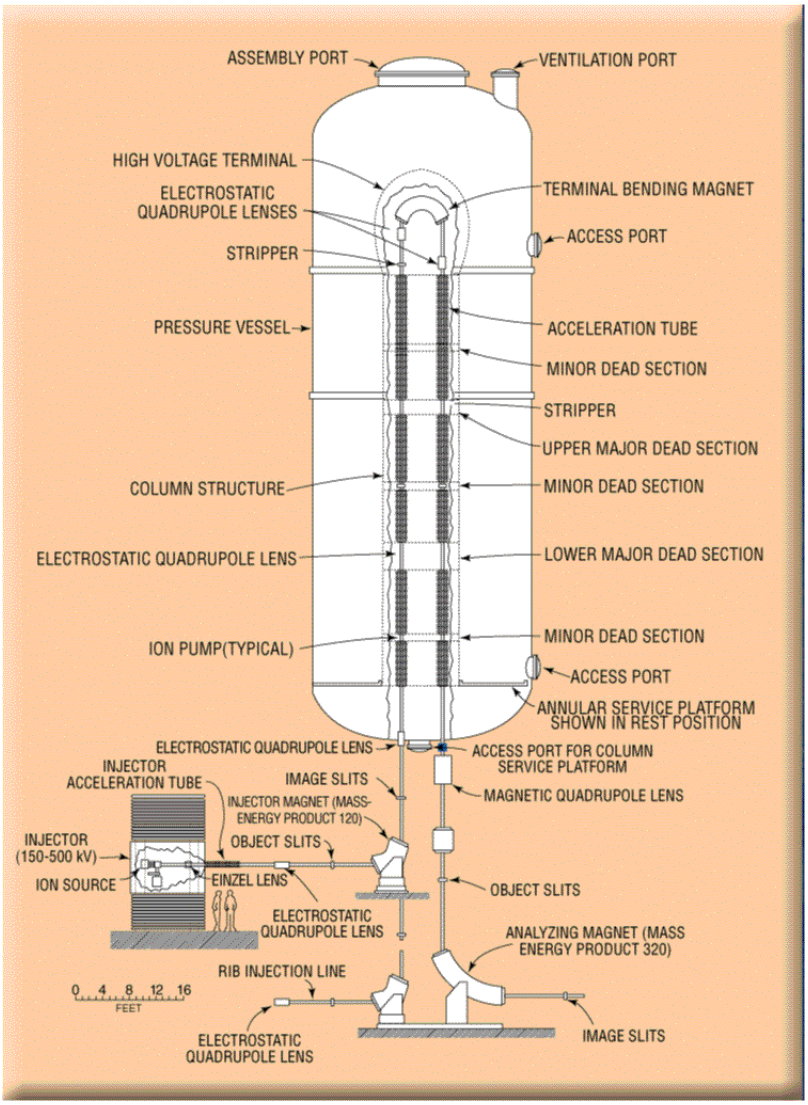

Figure 3.3: Schematic diagram of the 25 MV tandem accelerator at the HRIBF.

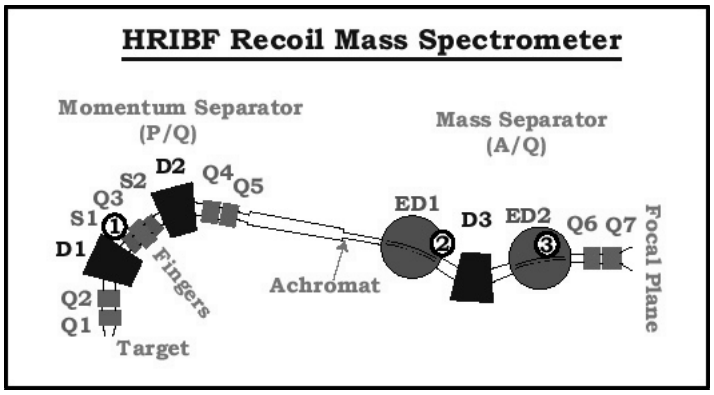

Figure 3.4: Schematic drawing of the recoil mass separator (RMS) at ORNL. The Q's are the magnetic quadrupoles labeled 1, 2, 3, ...7. The D's are the magnetic dipoles, the ED's are the electric dipoles, and the S's are the sextapoles.

and magnetic dipole mass separator [31]. The RMS consists of three magnetic dipoles labeled D1, D2 and D3, seven quadrupoles, labeled Q1, Q2, ...Q7, two sextapoles, S1 and S2, and two electric dipoles, ED1 and ED2, as shown in Fig. 3.4. A photo of the RMS is shown in Fig. 3.5. After the tandem accelerator primary beam strikes the target foil the recoils emerge from the target with a spread in energy and a large momentum. The first five quadrupoles of the RMS joined with the two sextapoles and the first two magnetic dipoles form a unit which acts as a momentum separator. If the radius r in a bending magnet with magnetic field intensity B, is given by $\omega = v/r = QB/m$ so that

$$\frac{P}{Q} = \frac{mv}{Q} = Br \tag{3.3}$$

where m is the mass of the recoiling ion and Q is the charge state of the recoil. By setting the magnetic field intensity, B, of the first five quadrupoles, Q1 - Q5 and the first magnetic dipoles, D1 and D2, to the required values, recoils with a specific momentum to charge ratio (P/Q) can be separated from other recoiling ions. The second unit of the RMS is an energy separator. It consists of two electric dipoles, ED1 and ED2, joined with the third magnetic dipole, D3, and the last two quadrupoles, Q6 and Q7, as shown in Fig. 3.4 and Fig. 3.5. This part of the RMS separates the recoils as a function of velocity of the recoiling ions. Combined together, the momentum separator and the energy separator form the complete mass separator in which the recoils are separated as a function of mass and charge (A/Q). The magnitude of the mass dispersion is then determined by the last pair of quadrupoles.

The flight time through the RMS is on the order of a few μs, depending on the energy of the recoil. This time of flight limits the capability to detect the recoils if the recoils contain isomeric transitions with $T_{1/2}$ ranging between 10 ns and 1 μs which would decay while in flight. If some of the isomeric transitions decay via the internal conversion process, then a disruption of the atomic electrons occurs which causes changes in the charge state. If the

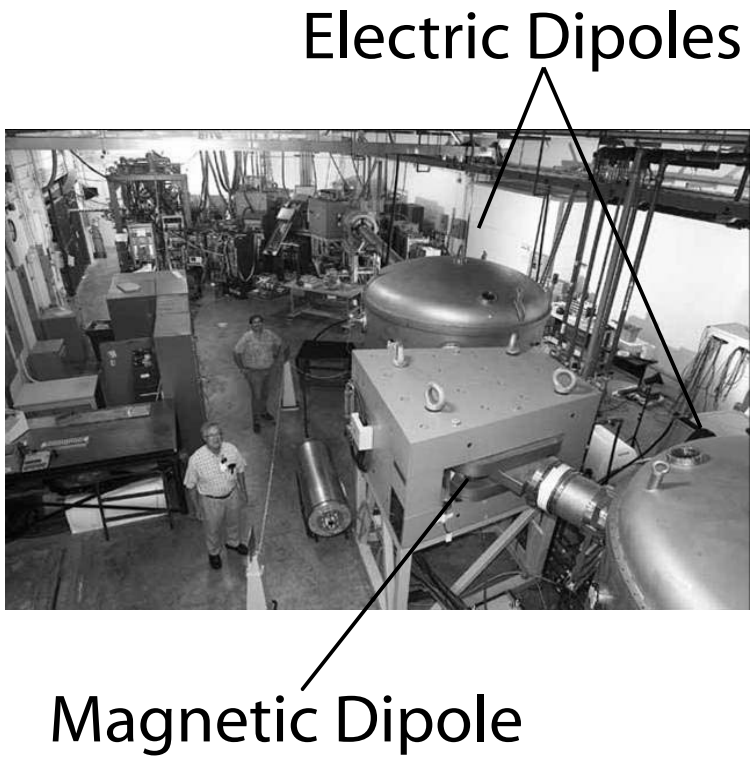

Figure 3.5: Photo of the RMS revealing the final focal plane.

isomeric decay is fast, this effect is eliminated by placing a charge resetting foil, usually ^{12}C, 10 cm away from the target. With the carbon foil a charge state equilibrium is obtained for separating all recoils. A 300-1000 μg/cm^2 target results in an RMS efficiency of <5% [31].

3.2 The Enge Spectrometer

The Enge spectrometer [30, 32, 33] shown in Fig. 3.6 was designed by Harold Enge for Scanditronix Corporation to study nuclear reactions with light-ion projectiles operating in high vacuum or gas-filled modes. It is now used by ORNL to study heavy-ion reactions as well. The focal plane of Enge showing the position sensitive avalanche detector and the energy detectors [34] is also shown in Fig. 3.6 . If the purpose of the experiment is to study particles with high energy resolution such as in proton and alpha particles spectroscopy [35], the high vacuum mode, see Fig. 3.7(a), is most suitable since the particles can be well separated by the magnetic field. However, if the purpose of the study is mainly to measure heavy ion reaction recoils [34] where the recoil products are distributed over many charge states, then the gas-filled mode, see Fig. 3.7(b), would be the appropriate mode. In this case, by adjusting the pressure in the spectrograph, all particles whose trajectories coalesce into the trajectory of the mean charge state can be collected at the focal plane of the Enge spectrometer. The mean charge state is just the average charge of the equilibrium charge distribution. The Enge spectrometer has the advantage over the RMS in that the time of flight (TOF) is 10 times less than the RMS. However, the RMS has the advantage of better mass separation of the recoils and cleaner spectra with less background. The gas-filled mode of Enge is particularly useful for reactions utilizing low intensity radioactive ion beams. The gas-filled spectrograph has the advantage here over other spectrographs at the HRIBF in that the efficiency for detecting low yield recoils at near-barrier energies is higher than other spectrographs.

At most times, a position sensitive avalanche detector (PSAC) is placed at the focal plane of Enge to provide position, timing, and energy signals. A special detector setup system consisting of a Double-sided silicon strip detector (DSSD) is now available for use at Enge. This setup was mainly designed to study proton radioactive ^{149}Lu. An off-line test using multiple alpha sources proved the setup was successful. For an online test, a microchannel plate detector (MCP) [36] was deployed along with the PSAC and two scintilator detectors. This setup was used to determine the time of flight (TOF), energy, and position of the implants to distinguish between the various mass implants. Once the desired recoil masses were identified on the TOF spectrum, the PSAC was removed and a Si detector was employed. This was a first attempt to use a Si detector at Enge. The aim of that test was to determine the possibility of using the DSSD system at Enge. For details on the MCP, PSAC, DSSD and other detectors see chapter 4.

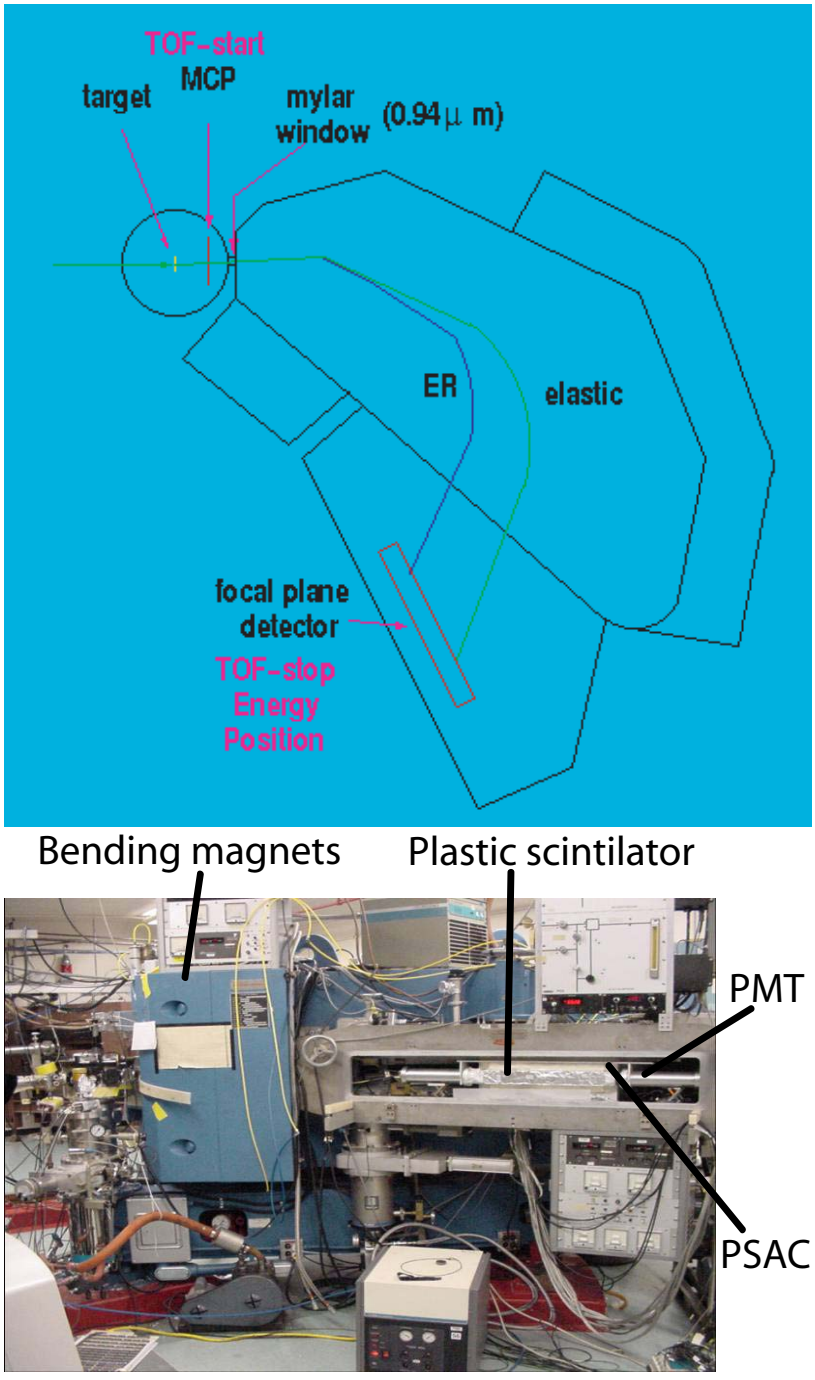

Figure 3.6: Top: The Enge gas-filled spectrometer at ORNL.
Bottom: The focal plane of the Enge spectrometer showing the Position sensitive avalanche detector and two scintilator detectors known as energy detectors which are attached to the PSAC.

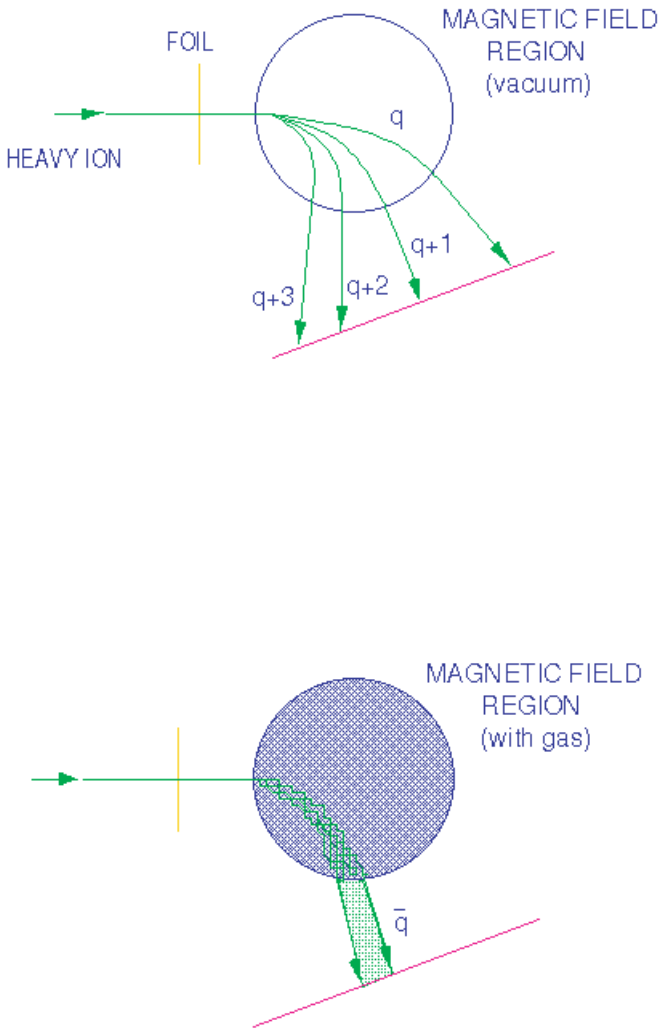

Figure 3.7: Comparison between gas-filled mode and vacuum mode of the Enge spectrometer. In the vacuum mode, the dispersion of the charge states of the recoils can be identified. In the gas filled mode, the mean of the charge states ($\bar{q}$) of the recoils is identified.

Chapter 4

Radiation Detectors at the HRIBF

The main principle of a radiation detector is to transfer part or all of the radiation energy to the detector mass which is then converted into electrical impulses [37]. We use several types of detectors at the HRIBF for various types of experiments. I will give a brief description of some of the most common detectors that I dealt with during my study period.

4.1 Position Sensitive Avalanche Counter

The position sensitive avalanche counter (PSAC) is a multi wired gas filled counter. It provides mass identification of the recoils based on their observed positions. In the first year or two of my stay at the HRIBF, we used the PSAC at the final focus of the RMS. I also got to work with the PSAC during some test runs at the Enge spectrometer. The PSAC used at the HRIBF (see Fig. 4.1) consists of five wire planes with each plane consisting of many gold plated tungsten wires 20 μm in diameter and 1 mm apart giving each plane a transmission efficiency of 98%. The planes are divided as follows; the first and last planes are anodes, the ones right next to them are the position sensing planes, i.e. X- and Y-

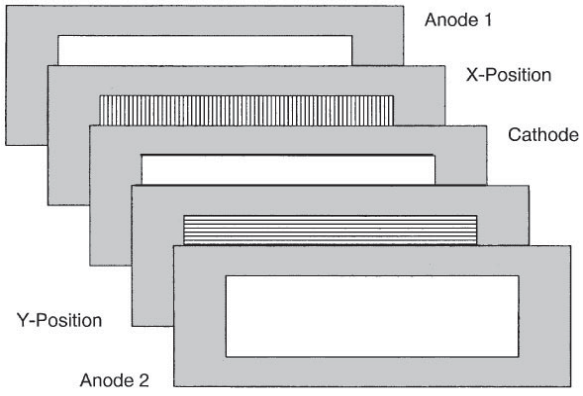

Figure 4.1: The Position Sensitive Avalanche Detector (PSAC) used at the HRIBF.

position planes with one having wires horizontally lined up (Y-position), while the other has the wires vertically lined up (X-position). The center plane is the cathode. In the case of the position planes, each two neighboring wires are connected to a single delay pin. Altogether, the pins are separated in time successively by 2 ns.

The PSAC depends on the gas ionization method where a radioactive nucleus ionizes the gas as it passes through the PSAC resulting in free negative electrons and positive ions. The electrons are then attracted towards the anode of the detector after an external voltage is applied which creates an electric field between the anode and the cathode wires in the chamber. When the primary ionization electrons gain sufficient energy from the accelerating electric field to also ionize gas molecules, they result in the release of secondary electrons which also ionizes more gas molecules and so on resulting in the formation of an electron avalanche. A signal is picked up on the wires using the center of gravity method, see the description of the multi wire proportional chamber (MWPC) in Ref. [37] for more details on this method. The induced signals are largest on the strip closest to the avalanche and diminish proportionally with distance from the avalanche point. If y_i is the coordinate of the i'th strip and Q_i is the measured charge on that strip, then :

$$Y = \frac{\Sigma(Q_i - b)y_i}{\Sigma(Q_i - b)} \tag{4.1}$$

where Y is the avalanche point (y-coordinate) and b is a small bias which is subtracted from each Q_i in order to correct for the dispersive effects of noise. The X coordinate is obtained in the same manner.

In practice, multiple wires fire due to delta rays. Because the distances to the anode differ, the wire signals are spread out over a time period corresponding to the drift times of the electrons. The desired signal is the one closest to the event and that's the one that arrives first. By adjusting the width of the gating signal in the read-out electronics, the late arriving electrons are eliminated. A test run for calibrating the PSAC is done first to produce the right selection gate width. The number of single and multiple firings are recorded. The point at which the "singles" firings are at a maximum and the multiple firings at a minimum determines the optimum gate width. Multiple firing can also be reduced by increasing the amount of electro-negative gas mixed with the chamber gas so that the electrons produced in the far regions will have a smaller probability of reaching the anodes, but this affects the chamber efficiency. The PSAC efficiency depends on the number of electron-ion pairs produced and collected in the chamber, the width of the gap, the pressure of the gas, the amount of electro-negative gas, the dE/dx of the fill gas, the threshold set on the electronics, the count rate, and most importantly the high voltage applied and the electronics.

The PSAC is no longer used at the RMS since it was replaced by the MCP (see description of this detector below). The PSAC is still used, however, at the Enge spectrometer [34].

4.2 The Microchannel Plate Detector

The MCP [36] is a position-sensitive-timing detector. It is a suitable detector for low energy heavy ions. The MCP shown in Fig. 4.2 is used for a variety of applications. It discriminates between genuine decay events and low energy implantation events. It can be used as a time trigger when it is placed a short distance from the final detector system. At the HRIBF, the MCP detector replaced the PSAC for its smaller size and better efficiency.

The MCP system is equipped with a thin foil that is used to emit secondary electrons during the interaction of the foil with heavy ions. These electrons are then accelerated towards the microchannel plate and are then multiplied. The MCP contains a position sensing plane that measures the x and y position of the emitted electron, see Fig 4.2.

Rapid acceleration of the electrons from foil to detector must be established in order to try to minimize the impact of the lateral velocity on the electrons. A strong inhomogeneous magnetic field is applied to the detector system. The magnetic field is highest near the foil and reduces as the electron travels towards the MCP detection units. A moderate electric field is applied as well. The electric field accelerates the electrons emitted from the foil linearly. Thus the accelerated electron feels an adiabatic change in the magnetic field as it travels towards the MCP detector unit. The transverse momentum changes to longitudinal under the magnetic + electric fields which causes the electron to travel in a spiral trajectory from the foil to the MCP. The electron trajectory takes on the form

$$r = \frac{v}{\omega} sin\theta \tag{4.2}$$

where v is the velocity that the electron is emitted with and $\omega = eB_i/m_e$ with e and m_e being the charge and mass of the electron and B is the applied magnetic field. The flux through each circular turn of the electron traveling in a spiral motion is just $\phi = eB_iA_i$ where A is the area of each circle given by πr^2. As the magnetic field decreases, the area of the electron orbit increases so that when the electron reaches the MCP, a magnified image [38] of where it had been emitted from the foil is registered and displayed. The position of where the heavy ion struck the foil can be determined. The position resolution of the MCP was determined to be $\approx$ 2 mm FWHM with the distance between the foil and detector being on the order of a few centimeters [36]. The assembly of the MCP is tilted at an angle of 30^o or 45^o relative to the beam axis to allow the heavy ions to pass through the system with minimum scattering. In some cases, permanent Sm magnets can be used to provide a uniform field of about 1 KG which focuses the emitted electrons and reduces image magnification.

The timing resolution depends significantly on the accelerating voltage and on filtering as the angle of the system introduces a variation in the flight path from different parts of the detectors foil. These two factors cause a spread in the time spectrum if they are not enhanced. The time resolution can reach as good as 800 ps FWHM [36].

As for the efficiency of the MCP detector, it depends on the number of electrons emitted from the foil after ion impact on it. The thickness of the foil itself does not contribute directly to the detector efficiency. However, the number of electrons emitted depend on

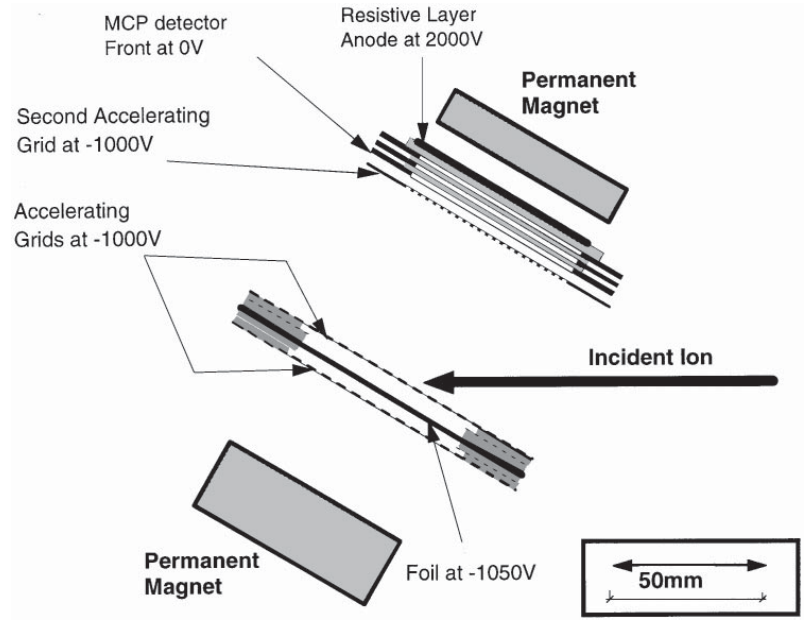

Figure 4.2: Top: The microchannel plate detector (MCP) used at the HRIBF. Usually, the MCP is placed before another detector such as the DSSD to provide a time reference as well as to distinguish between real events and accidental correlations by acquiring a coincidence condition between DSSD or the detector being used and the MCP.
Bottom: Photo of the MCP detector at the final focus of the RMS which provided implantation reference time and position signals of the recoils during the experiments used for the study of the $N = 77$ isotones at the HRIBF . In this picture, the electron emitting foil and the microchannel plate are both at an angle of 45^o relative to the beam line.

the electronic energy loss, i.e. dE/dx for the foil. The detection probability of the emitted electrons is raised by 10% with the emission of every additional electron when a magnet is placed behind the MCP. This method helps throw out the dependence on foil thickness. We obtain accurate time stamps for the ions impact on the foil using the MCP.

4.3 The Double-sided Silicon Strip Detector

The double-sided silicon strip detector (DSSD) [39] is a semiconductor detector. It was developed to first study the phenomenon of ground state proton radioactivity in 1992 [39]. The DSSD used in this work basically consists of a 65 μm thick silicon wafer that covers an area of 4 cm $\times$ 4 cm. The wafer has gold collection electrodes on each surface which are etched to provide 40 independent horizontal strips on one side and 40 independent vertical strips on the other side (see Fig. 4.3). Each strip is about 1 mm wide and the distance between two adjacent strips is less than 50 μm. Each of the 80 independent strips is equipped with a chain of electronics to analyze the collected charge pulses. The DSSD provides two dimensional position information by measuring both the x-y positions with millimeter resolution. The DSSD has a thickness that ranges from μm's to mm's depending on the type of recoils one is searching for and their decay activity. The 40 $\times$ 40 strip arrangement creates 1600 independent pixels identified by position. This enables the establishment of correlations between the implanted ions and the subsequent decays. The number of strips per face producing valid energy signals is used to calculate the front and back multiplicity for each event. Decay events produce single strip multiplicities for typically 90% of front face signals and 80% of back face signals. These percentages reduce further when accounting for effects from decay products crossing through more than one strip. The DSSD's high granularity effectively gives a large number of detectors in a given area while reducing the count rates per effective detector.

The passage of ionizing radiation creates electron-hole pairs in the DSSD rather than electron-ion pairs as is the case in gas-filled detectors. The electrons are collected on one face and the holes on the other face when an electric field is applied between the front and back faces. The high voltage applied here is 10 times smaller than the one applied to the PSAC and the amount of ionization produced for a given energy is an order of magnitude greater resulting in increased energy resolution. The electronics connected to the DSSD record the time and energy of implanted ions and their subsequent decays by proton or α emission. The different electronics settings can be found in many references [15, 40–42].

When voltage is applied to the terminals of the DSSD, a small fluctuating current flows through the DSSD junctions appearing as noise in the detector and setting a limit on the smallest signal pulse height which can be observed. The source of this leakage current could be due to the movement of minority carriers, holes, from the n-region to the p-region and vice versa. The detector temperature (T) affects the leakage current according to the equation

$$I_{leak} = T^2 e^{-\frac{constant}{kT}} \tag{4.3}$$

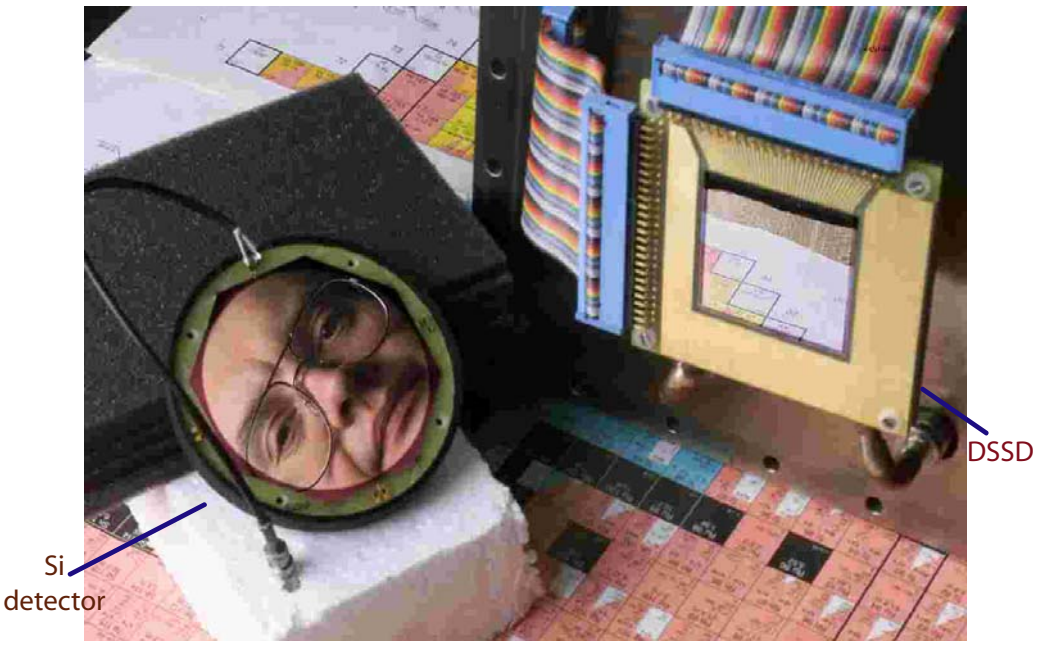

Figure 4.3: The DSSD used at the HRIBF. The Si detector shown is usually placed behind the DSSD during an experimental run. The DSSD is a 16 cm^2 silicon detector with charge collecting electrodes of 40 horizontal (X) strips and 40 vertical (Y) strips.

where I_{leak} is the leakage current in amperes, k is the Boltzmann constant, and T is the temperature of the DSSD plane in kelvins. Therefore, the strip detector is mounted on a flange connected to cold fingers which are connected to a refrigerating device filled with an anti-freeze coolant keeping the detector flange at temperatures below 0^oC. In most cases, we set the temperature to -20^oC as we found that temperature is best for our DSSD setups. The largest source of leakage current is through surface channels. When exposed to air, a SiO_2 resides on the surface. A fixed positive charge can be trapped near the Si-SiO_2 boundary. This trapped charge can have a noticeable effect if it is near a metal layer as it becomes mobile. That is why clean encapsulation is required to minimize this source of leakage current. During operation, high energy radiation damages the detector causing a linear increase in leakage current with radiation dose according to the formula:

$$\Delta I_{leak} = 3 \times 10^7 \phi V \tag{4.4}$$

where ϕ is the radiation flux and V is the applied voltage. Any conducting material that is dropped on the detector might connect two strips together causing a short circuit and a large leakage current is observed and/or very bad detector energy resolution. However, one important characteristic of the strip detector is the low leakage current compared to conventional surface barrier devices.

The DSSD makes it possible to search for proton radioactivity produced with sub-microbarn cross sections. It measures energy signals of the implantation event and of the subsequent proton and alpha decays of the nucleus. The silicon wafer of the DSSD measuring $40\ mm \times 40\ mm$ is sufficiently large to accommodate the beam image which is usually shaped as an ellipsoid.

The range of charged particles in silicon is 15 μm for 1 MeV protons and 30 μm for 5 MeV α particles. Thus, in order to avoid or minimize the occurrence of multi-strip events, the strip width is made large compared to these ranges. Yet the detector is sufficiently thin to remain transparent to low energy positrons emitted in β^+ decays. The dead time for both energy and position signals from the strip detector is only limited by the baseline restoration time of the amplifiers under overload which can be on the order of microseconds to nanoseconds.

A distinction between decay and low energy implantation events in the DSSD [39] can be made at the HRIBF by whether or not these events appeared in coincidence with signals from the PSAC or the MCP.

4.4 The Clover Array for Radioactive Decay Studies

The CARDS array [43] shown in Fig. 4.4 is a three dimensional octagonally shaped ring that can hold four to eight segmented Ge detectors, γ-X detectors, LOAX detector, and/or BESCA Si conversion electron detectors. The detectors are mounted on a support that surrounds a moving tape collector if needed. The close geometry of the array allows for angular correlations to be made between coincident gammas. Plastic scintilators or lead blocks

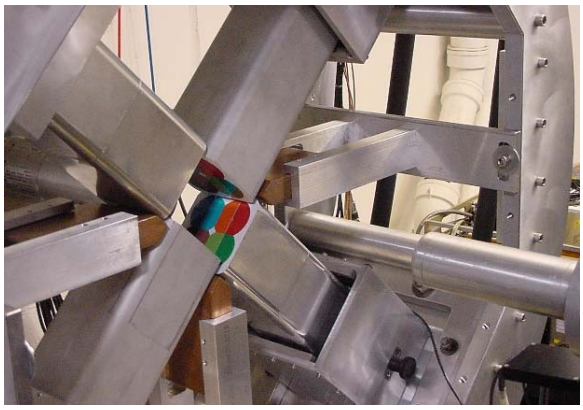

Figure 4.4: The clover array for radioactive decay studies CARDS used at the HRIBF. Also shown are four Ge clover detectors with lead blocks between them [13]. This setup was used in the study of ^{140}Eu discussed in this dissertation.

or any other material can be placed tightly in front of the detectors to allow background rejection of events from the undesired species, room background...etc [13].

Future plans for the CARDS array is to add neutron detectors to enable beta-delayed neutron emission measurements.

4.5 The BESCA conversion electron detector

The Bellows Electron Spectrometer for the Cards Array (BESCA) [43] shown in Fig. 4.5 consists of a 5 mm thick, 176-180 mm^2 high resolution Si(Li) detector mounted on a movable cold finger and cooled to liquid nitrogen temperatures. The detector is used for intermediate energy electron spectroscopy. The Si(Li) detector assembly can be pulled back via an attached motor into a large cylinder which can be isolated from the beam line by closing the entry valve. Once in its compartment, the system is valved allowing BESCA to have an independent vacuum system. When in vacuum, one must be cautious in pulling BESCA in and out of its compartment as a quick sudden move can cause one side to move faster than the other causing the system to tilt side ways which then jams the pulley system. The metal chain attached to four pulleys controlled by the motor would then need to be removed to adjust BESCA back in a straight line. This is not trivial and could be a hassle during a run. See chapter 5 and section 6.2 for details on the performance of BESCA.

4.6 The Si-box

The Si box consists of four passivated ion-implanted junction silicon detectors made by Eurisys Measures [44] and is usually mounted in front of the DSSD, see Fig. 4.6. They are basically N-type silicon wafers with high purity. The p-n junction is formed by boron implantation into the front side of each Si chip. The silicon wafer thickness is ≈ 700 μm. The

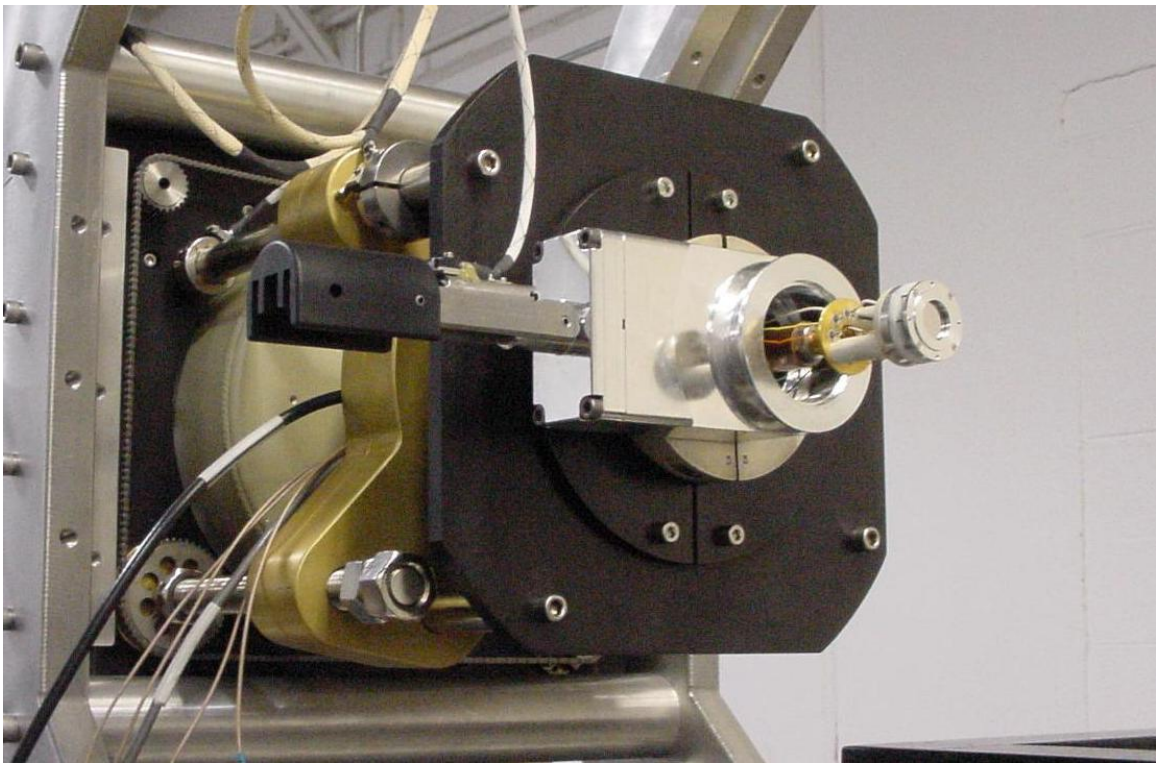

Figure 4.5: The bellows electron spectrometer for the cards array (BESCA) conversion electron detector mounted on the CARDS array at the HRIBF. When not in use, the 176-180 mm^2 Si(Li) detector is withdrawn inside the big cylindrical compartment and a special valve is then closed keeping the detector sealed in its own independent vacuum.

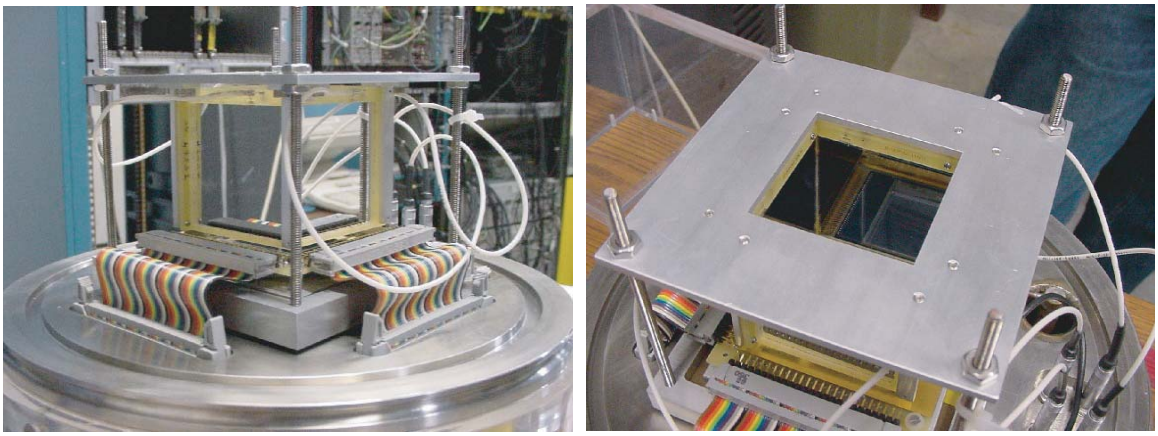

Figure 4.6: Photographs of the detection setup used during the ^{146}Tm experiment. The 65 μm thick DSSD was surrounded by four 700 μm thick Si detectors mounted in a box geometry. The left picture shows a side view of the setup while the right picture shows an angled top view. Below the DSSD is a Si(Li) detector, 45 mm by 45 mm, with an active measuring thickness of 3.9 mm.

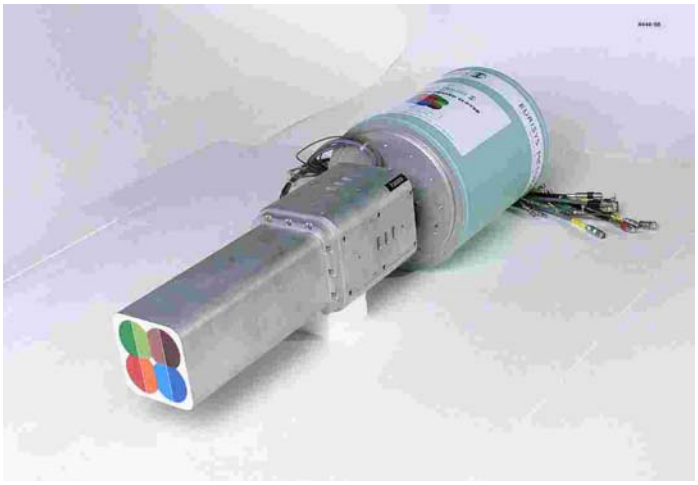

Figure 4.7: The Ge clover detector used at the HRIBF. The clover consists of four HPGe crystals. Each crystal is electronically segmented into two halves.

surroundings of the silicon wafers are originally oxidized making a layer of oxide passivation, mainly SiO_2. A window opening is then cut through the layer to allow ion implantation. The depletion depth of the detector determines the maximum energy absorbed from the ionizing particles. Each detector is placed in a metal housing for its own protection from external physical damage. The metal housing also serves as a grounding post for the front side of the detector via a conducting implantation joint. The rear side is connected to the central electrode of the radial microdot connector. A positive bias voltage of ≈ 200 V is applied to the detectors. At the HRIBF. we use the Si box in conjunction with the DSSD to veto escaping particles from the DSSD, see Chapter 5 for more details.

4.7 The HPGe Detectors: The Segmented Ge Clover Detector and The LOAX Detector

The Ge clover detector [30] is used to detect γ-rays. It consists of four individual HPGe crystals, see Fig. 4.7, with each crystal being segmented into two halves electronically. Each crystal has an efficiency of 25 % relative to a 3 $\times$ 3 inch NaI detector. All four crystals share a common cryostat. The signal of each crystal can be displayed individually, however, for best results and since a γ-ray can scatter from one crystal to any of the other three crystals, the signal from all four crystals are added up giving a total pulse height. This can be done since the dead layer between the crystals is very small. This method is called the "add-back" mode which increases the efficiency of the clover detector as a whole. The reason for dividing one detector into several crystals is to reduce the crystal opening angle, thus reducing γ-ray broadening due to the Doppler effect. Having multiple crystals also reduces detector sensitivity to neutron damage [45].

A HPGe detector, in general, is a large reverse-biased diode with either an n- or p-type Ge junction formed in a cylindrical or disk-like shapes to optimize the electric field inside the crystal for reduction of noise. Detector capacitance along with internal impedance produces radio frequencies which add to the background noise reducing resolution. The cylindrical shaped crystals, closed at one end, are called coaxials.

The LO-AX [46] detector or simply LOAX is a one crystal HPGe detector 70 mm in diameter. LOAX is a short coaxial detector with a large active area resulting in low capacitance coaxial geometry which results in very good energy resolution at low energies. The LOAX used at the HRIBF is topped with a thin Be window to allow the low energy photons to pass through with minimal attenuation. For details on the performance of the clover detectors and LOAX, refer to chapter 5.

Chapter 5

Experimental Setup for the Study of the $N = 77$ Odd-Z Isotones at the HRIBF

Three different experiments were utilized at the HRIBF at Oak Ridge National Laboratory (ORNL) to study the $N = 77$ odd-Z isotones, ^{140}Eu, ^{142}Tb, ^{144}Ho, and ^{146}Tm.

The ^{140}Eu, ^{142}Tb and ^{144}Ho nuclei were produced at the HRIBF in fusion-evaporation reactions between ^{54}Fe projectiles, at 315, 250 and 225 MeV, respectively, and a 98.7% enriched, 1 mg/cm^2, ^{92}Mo target. Recoiling ions were separated according to their mass to charge (A/Q) ratio by the RMS. The time of flight from the target to the focal plane of the RMS was about 2.2, 2.5 and 2.8 μs for ^{140}Eu, ^{142}Tb, and ^{144}Ho recoils, respectively. The recoils passed through a position sensitive MCP detector located at the final focal plane of the RMS. The MCP provided recoil implantation time reference and position signals. The electron emitting foil and the plate were both tilted at an angle of 45^o relative to the beam (see Fig. 4.2) allowing the recoils to pass through with minimal attenuation and scatter.

In the $A = 140$ setup [13], the average beam current was $\sim$ 19.5 pnA. The fusion evaporation products were collected at the final focus of the RMS operating in the diverging mode and optimized for $A/Q = 140/27$ and recoil energy of 92 MeV. The recoils were implanted in a passive catcher inside the CARDS array which consisted of four Ge clover detectors and a γ-X detector which functions similar to the LOAX detector described in chapter 4. All five detectors were set up in a closed geometry, see Fig. 4.4. Back scatter Compton suppression lead blocks were placed between each two neighboring clover detectors. The average distance between the clovers and the center of the collection foil was about 5 cm, chosen to maximize the solid angle of detection. The efficiency of the four clover array had a maximum of 18% for 80 keV γ-ray energies and was still 4% at 1.33 MeV. Since no conversion electron detector such as BESCA was available during this experiment, electron data were not collected for $A = 140$ nuclei.

In the case of ^{142}Tb and ^{144}Ho, the recoils were implanted in an aluminized mylar tape in the Moving Tape Collector (MTC) [43] located at the final focus of the RMS. To collect

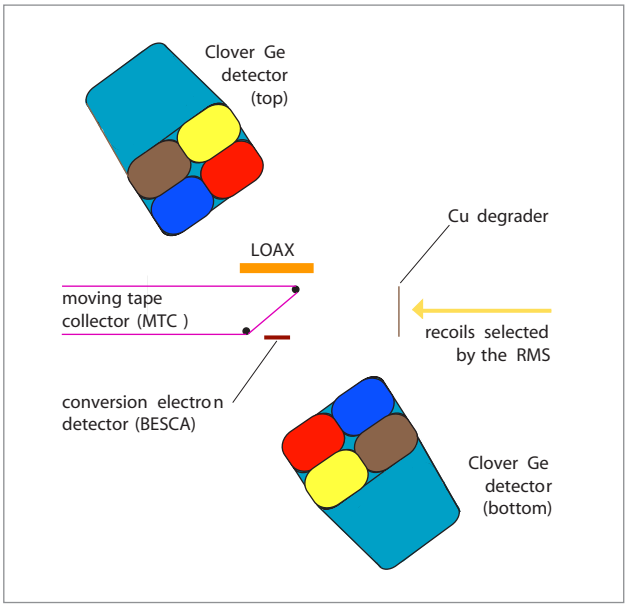

Figure 5.1: Schematic diagram of the setup used in the study of odd-Z $N = 77$ isotones ^{142}Tb and ^{144}Ho at the HRIBF. The setup was placed at the final focus of the RMS.

$A = 142$ and 144 recoils, the RMS was optimized for $A/Q = 142/24$ and recoil energy of 60 MeV after passing through a reset foil and the 45^o MCP foil, and for $A/Q = 144/23$ and recoil energy of 52 MeV, after passing through the MCP foils. A degrader copper foil (2.3 mg/cm^2) was placed in front of the implantation point of the tape. This foil slowed the 60 MeV ^{142}Tb ions to about 10 MeV, resulting in an implantation depth of about 3.3 μm. Electrons with energies below 20 keV emitted at this depth were stopped in the tape, and measured energies of 85 keV electrons were shifted down by about 3 keV. The average detection distance of the Ge detectors was approximately 5 cm from the center of the tape to maximize the solid angle of detection. The detection distance varied for BESCA. In the first attempt, it was 24 mm from the center of the beam line. In the second attempt, the Si(Li) detector was moved 3 mm closer to the beam line to maximize the solid angle and collect as much electron data as possible. The MTC was surrounded by a LOAX detector, two segmented Ge clover detectors, and a high resolution 180 mm^2 Si(Li) conversion electron spectrometer, BESCA [43], see Fig. 5.1. All four detectors were mounted on the CARDS array. The rate of recoils detected in the MCP was about 2000/second for mass 142 and an average of 600/second for mass 144.

Efficiency curves for the detectors were determined by using standard sources (see Fig. 5.2). BESCA's efficiency was measured off-line with point-like open electron sources of ^{207}Bi and ^{133}Ba to be $\approx 1.6\%$ in a close geometry and constant for the electron energies from about 50 keV to 1 MeV. The summed efficiency of the two clover detectors was about

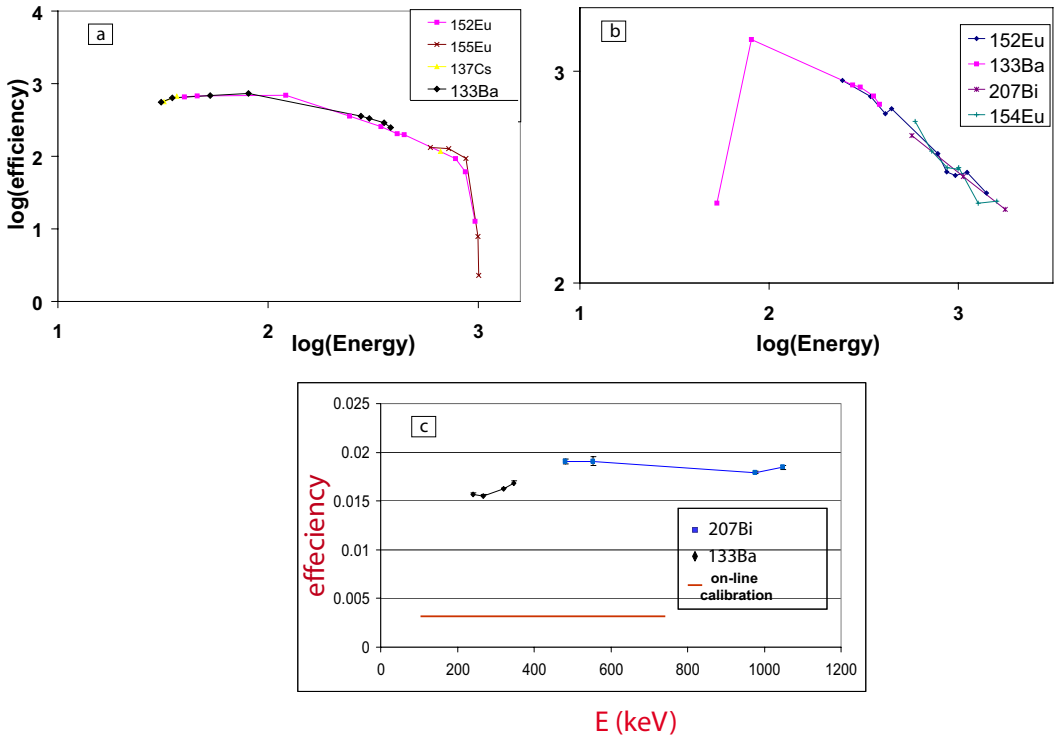

Figure 5.2: Measured efficiency curves for the (a)two Ge clover detectors, (b) LOAX low energy photon detector, and (c) BESCA conversion electron detector 21 mm away from the center of the beam line. The detectors were setup in a CARDS system to study isomeric states in ^{142}Tb and ^{144}Ho. The efficiency curves were obtained using standard sources which were then normalized to a standard ^{154}Eu source.

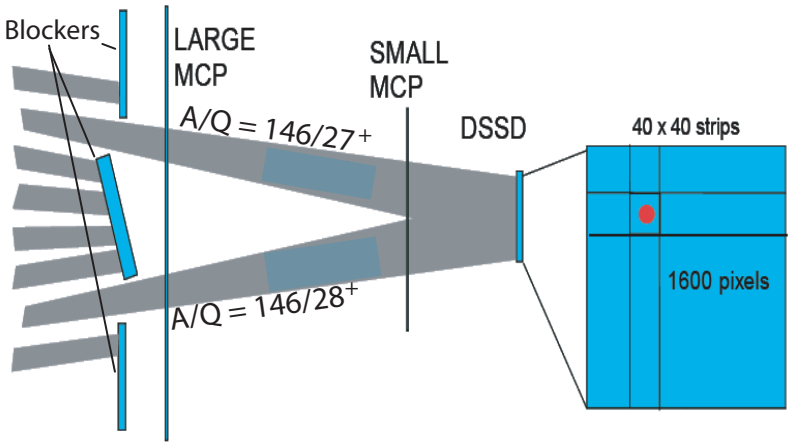

Figure 5.3: Schematic diagram of the recoils passing through the two MCP detectors and the two slit, three blockers system to be finally implanted in the DSSD at the final focus of the RMS in the ^{146}Tm proton emitter study. The large MCP was used for A/Q identification of the recoils. The small MCP was used as an additional timing reference.

13.6% at 121 keV and 2.7% at 1408 keV corresponding to γ-rays emitted from a ^{152}Eu source. The maximum efficiency of the LOAX detector was about 6.9% at 121 keV.

During the run, the BESCA pump failed. This did not only affect the vacuum of the whole BESCA + beam line negatively, but it also tilted the Cu degrader allowing the beam to be implanted deeper into the tape. The problem was noticed only towards the end of the run. Thus, the effective measurement time of ^{142}Tb with BESCA was 8 hours with an average ^{54}Fe beam current of 20 pnA. This was sufficient to determine the multipolarities of most of the transitions de-exciting the isomeric states in ^{142}Tb along with the spins and parities of all populated states. No electron data were collected for $A = 144$ nuclei.

In these experiments studying ^{140}Eu, ^{142}Tb, and ^{144}Ho, the time correlation of γ-rays with implanted ion was accomplished by software, utilizing the energies and time stamps from all detectors. The time difference between detected γ-ray and preceding ion implantation was calculated and used to construct the two dimensional matrix of time vs γ-ray energy.

A new experiment was made on the decay of proton radioactive $N = 77$ isotone ^{146}Tm at the RMS. The nuclei of interest were produced in the fusion-evaporation reaction between a 297 MeV ^{58}Ni beam and a 0.91 mg/cm^2 ^{92}Mo target. The reaction products were separated by the RMS and implanted at the final focal plane into a 65 μm thick DSSD [39]. Before implantation into the DSSD the recoils passed through two MCP detectors (see Fig. 5.3). The larger MCP was used to observe the mass dispersion of the recoils and to record the implantation time, while the smaller MCP, located closer to the DSSD, was used to give redundant information of implantation signal timing. Once the proper A/Q was identified, a two slit, three blockers system was used in front of the MCPs to select the desired A/Q, 146/27 and 146/28, ions to pass.

The DSSD was surrounded by four 700 μm thick silicon detectors forming a Si box (see Fig. 4.6). The Si box signals were used to veto escape protons and α particles which release only part of their energy in the DSSD and therefore add to the background. In Fig. 5.4 the effect of such background reduction is shown. A Si(Li) detector with an active measuring thickness of 3.9 mm was placed behind the DSSD for further vetoing of any particles escaping from the DSSD. The resolution of the DSSD detector for 5.5 MeV alpha particles from a ^{241}Am source was about 26 keV at the beginning of the run and about 30 keV by the end of the run; the degradation was caused by radiation damage from the high energy implantations. The measurement lasted 96 hours with an average ^{58}Ni beam current of about 20 pnA. In this experiment, the rate of recoils detected in the small MCP was about 1.2 kHz.

The signals from all RMS detectors in all three experiments were processed by using 40 MHz Digital Gamma Finder (DGF) modules manufactured by X-ray Instrumentation Associates (XIA) [47, 48]. Preamplifier pulses were digitized without prior shaping. The amplitude and real-time of the signals were derived using the on-board Digital Signal Processor and 40 MHZ clock. γ-ray signals were all counted in time-stamped "singles" mode [48] with no restrictions on the recoil-delayed γ-ray correlation window allowing for continuous control of background γ-rays caused by the long lived β emitting isobars in the mass 140 region.

As an example of an experimental electronic setup, Fig 5.5 shows the electronic setup designed for the study of proton emitter ^{146}Tm. The experiment used 24 DGF-4C modules placed in two separate CAMAC crates since each crate was designed to hold up to 20 modules at a time. This was a first attempt to connect 24 modules in separate crates; Dr. Robert Grzywacz and Dr. Marek Karny's work and efforts are acknowledged here. All the experimental circuit designs for any other experiment described in this dissertation used the same design but with only one crate. In the two crate setup, as shown in the figure, the BUSY and SYNC signals from the last DGF in the first crate is connected to the BUSY and SYNC signals in the first DGF module of the second crate respectively. To use a one crate system, these two cables must be disconnected. The software that runs the DGF modules must also be modified to account for a one crate system.

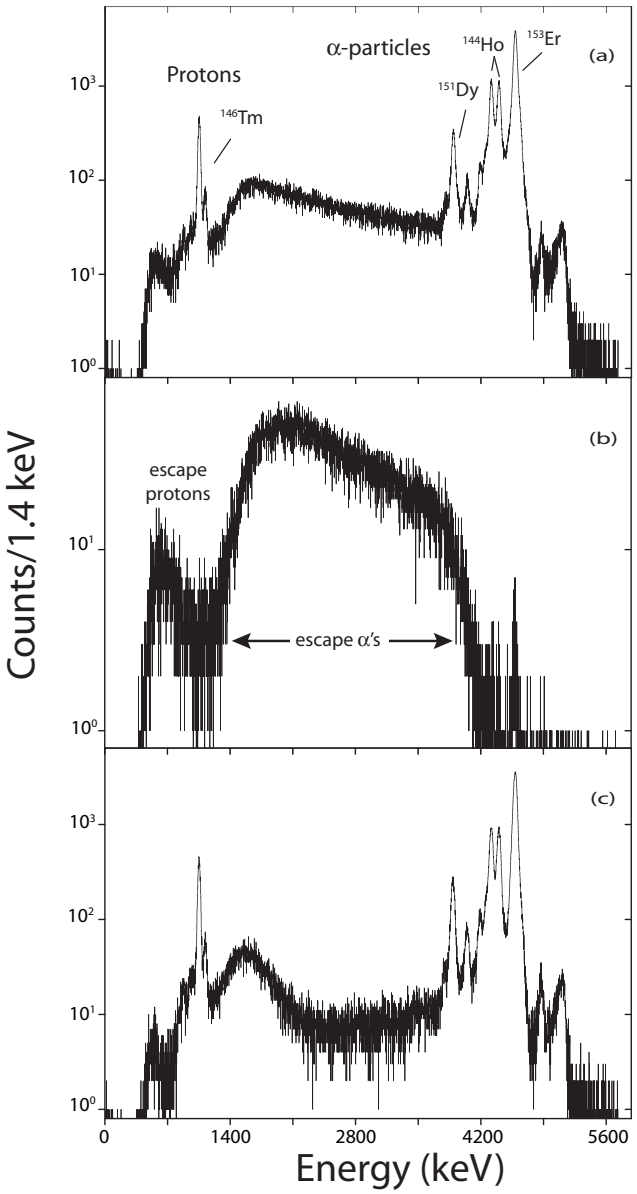

Figure 5.4: (a) Energy spectrum of protons and α-particles from the DSSD with no veto applied. (b) Energy spectrum of the particles detected in the DSSD in coincidence with any of the Si box detectors. (c) Energy spectrum of protons and α-particles from the DSSD in anti-coincidence with the Si box detectors and the SiLi detector. A rigid mass gate was also applied here and a condition that the front and back energy spectra of the DSSD be in agreement with each other within 2%.

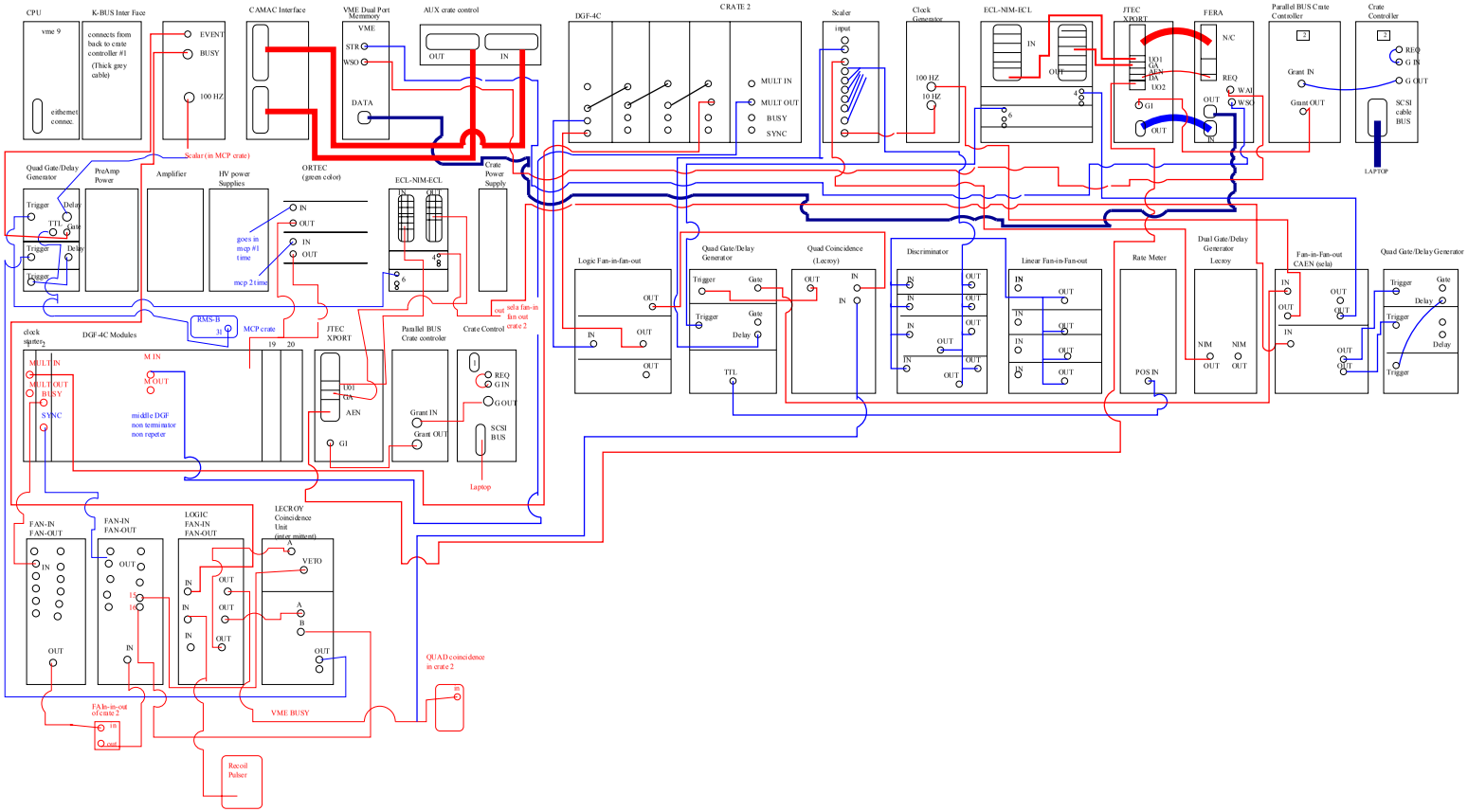

Figure 5.5: Electronic setup used in the study of ^{146}Tm with 24 DGF-4C modules placed in two separate CAMAC crates.

Chapter 6

Experimental Results

In this chapter, the results of the three experiments mentioned in the previous chapter will be discussed.

6.1 ^{140}Eu

The β decay of ^{140}Eu^{gs} was first reported by Westgard *et al.* [49], and a decay scheme was constructed by Beraud *et al.* [50]. Firestone *et al.* [1] investigated the decay of ^{140}Eu further and presented a more comprehensive picture of the decay. In Ref. [1], a meta-stable state ^{140m1}Eu with $T_{1/2} = 125$ ms was also reported.

Examination of the two dimensional γ-ray energy versus time difference between the recoil implantation and the γ-ray detection data from our experiment revealed a subset of observed γ-rays with a short decay time. By gating on the first microsecond of the two dimensional spectrum and subtracting the spectrum gated on the second microsecond, a spectrum of γ-rays correlated with the decay of the recoils with sub-microsecond half-lives was obtained, see Fig. 6.1(a).

The properties of the measured γ-ray transitions are listed in Table 6.1. The coincidence relations for γ-rays from this short lived isomer were examined by generating an E_γ-E_γ coincidence matrix. As an example, Fig. 6.1(b) shows the γ-ray spectrum obtained in coincidence with the 170.4 keV γ-line. This coincidence (and others) revealed Eu X-ray energies $K_\alpha \approx 41$ keV and $K_\beta \approx 47$ keV, thus establishing the cascade as the decay of an isomeric state in ^{140}Eu [2, 51]. The half-life, $T_{1/2} = 302(4)$ ns [51], of this new isomer, ^{140m2}Eu, was deduced from the decay pattern of the summed 98.1, 170.4, 252.0, and 422.5 keV γ-rays, see Fig. 6.2. Our $T_{1/2}$ value agrees well with two independent studies published recently [3, 4].

The excitation energy of the ^{140m1}Eu isomeric state deexciting to the 1^+ ground state via the 175 and 185 keV transitions ($T_{1/2} = 125$ ms) has been postulated to be < 234 keV with the spin and parity of $I^\pi = 5^-$ [1]. The energy limits for the non-observed transitions deexciting the 125 ms $I^\pi = 5^-$ isomer, ^{140m1}Eu, of "< 59" and "< 49" keV, were suggested in Ref. [1]. The "< 59" and "< 49" keV γ-rays are likely to be strongly L-converted

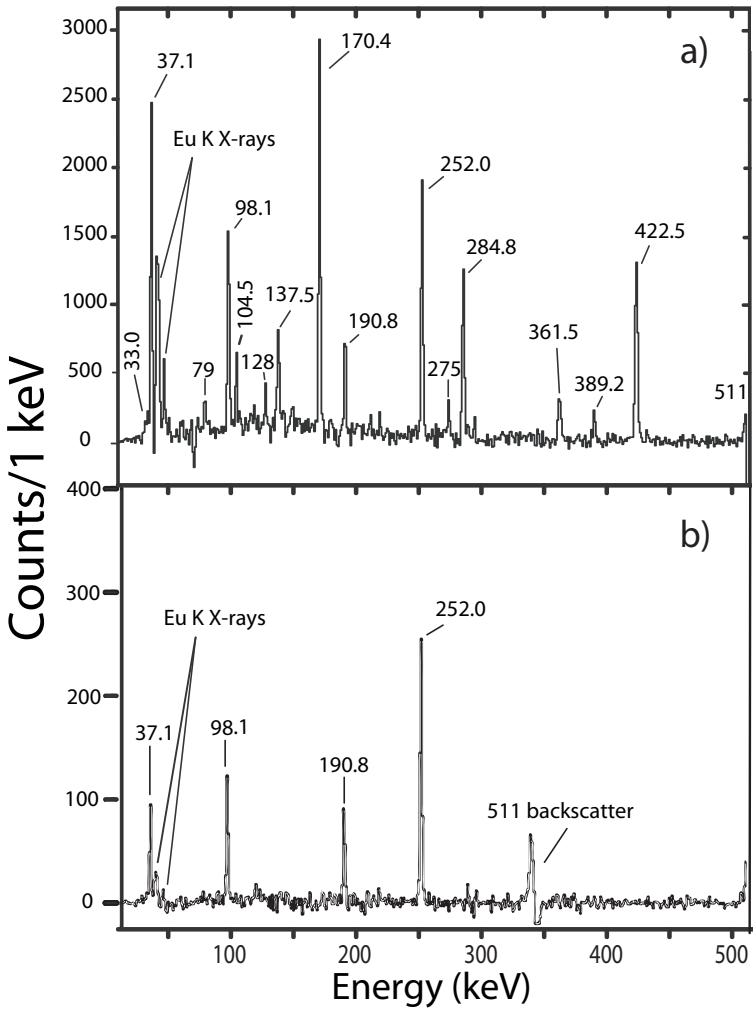

Figure 6.1: (a) Spectrum of γ-rays collected within 1 μs of an implant minus γ-rays collected between 1 and 2 μs during the $A = 140$ measurement. The 79, 128 and 275 keV lines shown in the figure are long lived impurities and are not in coincidence with the Eu X-rays. (b) Spectrum of γ-rays in coincidence with the 170.4 keV line in the decay of ^{140m2}Eu.

Table 6.1: Decay properties of the $I^{\pi} = 8^{+}$ isomer in ^{140}Eu. The energies, relative intensities, measured conversion coefficients, and multipolarities are listed for the observed γ transitions.

E_{γ} (keV)	Rel. I_{γ} (%)	measured[a] α_K, α_{Itotal}	Multipolarity (literature) [3]	Adopted multipolarity (this work)	I_{total} (%)
33.0(10)	6(3)	$\alpha_T = 7.1$		(M1)	24(12)
37.1(3)	100(9)	$\alpha_T = 0.65(28)$	M1	E1	83(8)
98.1(3)	26(3)	$\alpha_K = 0.3(1)$	E1	E1	17(2)
104.5(3)	9(2)	$1.6 < \alpha_T < 2.1$	E1	(M1/E2)	13(3)
137.5(3)	15(3)	$0.75 < \alpha_T < 0.78$	E1	(M1/E2)	13(3)
170.4(3)	53(7)	$\alpha_K = 0.4(1)$	M1	M1/E2	37(6)
190.8(3)	16(4)	$\alpha_T = 0.21(7)$	M1	M1/E2	10(2)
252.0(3)	50(7)	$\alpha_T = 0.11(5)$	(E1)	M1/E2	28(4)
284.8(3)	38(6)	$\alpha_K = 0.08(3)$	M1/E2	M1/E2	21(3)
361.5(3)	14(4)	$\alpha_T = 0.03$	E2	E2	7(2)
389.2(3)	7(3)	$\alpha_T = 0.027$	(M2)	(E2)	4(2)
422.5(3)	59(10)	$\alpha_T = 0.02$	(M2)	E2	30(5)

[a]Values of α with uncertainties are our measured values while the others are calculated values.

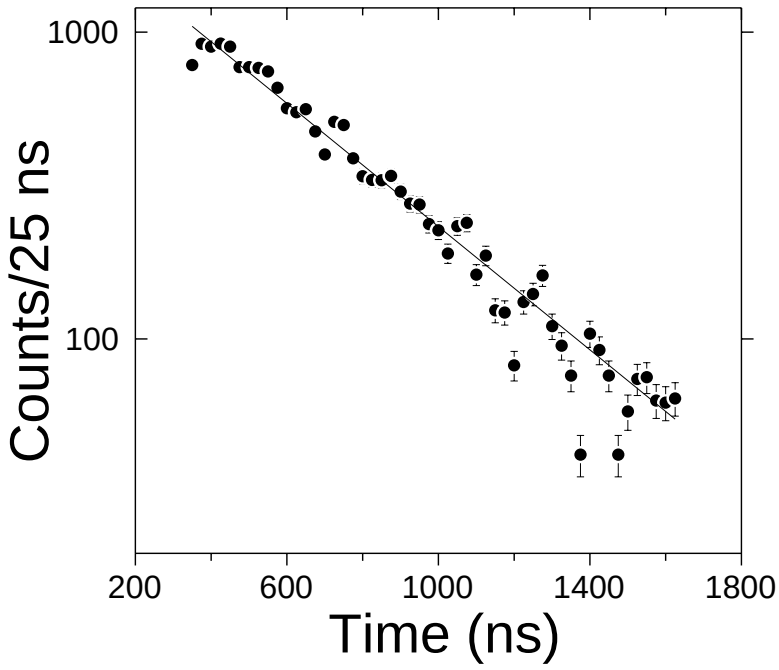

Figure 6.2: Decay pattern of ^{140m2}Eu, $T_{1/2} = 302(4)$ ns, from the sum of 98.1, 170.4, 252.0 and 422.5 keV γ-lines after subtracting the appropriate background. Time refers to the time difference between the implant signal and recorded γ-ray.

transitions. Several other transitions in ^{140}Eu were observed in the β decay of the 0^+ ground state of ^{140}Gd [1]. Many of them were observed in prompt coincidence with the 185 and 175 keV lines. We do not believe that the 302 ns short lived isomer decays to the 1^+ ground state of ^{140}Eu since the 302 ns fast decays do not include any of the known transitions feeding the ground state and none of the isomeric γ-rays were observed in the decay data [1]. This indicates that the short lived isomer has a higher spin value than the known longer lived 125 ms isomer. Due to these reasons we suggest that the 302 ns isomer feeds the 125 ms isomer. We have obtained experimental verification of the relative position of the two isomers, ^{140m2}Eu and ^{140m1}Eu, with the 302 ns level above the 125 ms activity, see Fig. 6.3. Figure 6.4 shows the 175 keV and the 185 keV transitions, known to deexcite the 125 ms level [1], in the γ-ray spectrum following the decay of the 302 ns activity within 200 ms. It confirms independently the sequence of isomeric levels given in Ref. [3,4]. Other lines appearing in Fig. 6.4 such as the 39 keV Sm K X-ray line and others are believed to be the result of random accidental correlations. Sm K X-rays represent the strongest lines in the singles γ-ray spectrum. A low energy peak appears at 59 keV in Fig. 6.4. Its appearance does not allow a conclusion that it is real since its intensity error is larger than the total number of counts in that peak. The 59 keV peak that appears in Fig. 6.4 was not observed above the background level in the first 200 ms nor in the second 200 ms, see Fig. 6.4, yet it appeared after subtraction. For the 175 and 185 keV lines, however, the number of counts are 1300(510) and 1045(440), respectively, which indicates that those lines are correlated with the transitions from the 302 ns isomeric level.

To achieve the experimental correlation between ^{140m2}Eu and ^{140m1}Eu, we observed only those events coming after the 98.1, 170.4, 252.0, and 422.5 keV γ-rays. We then gated on the first 200 ms and obtained a one dimensional spectrum carrying true events and background. In order to subtract the background we subtracted the second 200 ms multiplied by a factor of 1.017 to account for an apparent reduction in background due to count rate, see Fig. 6.5.

Using our results on ^{140m2}Eu and other available data on ^{140}Eu, we constructed a level scheme involving two isomeric states and the intermediate levels populated in their decay, see Fig. 6.3. The level scheme and the spin and parity assignments given in Fig. 6.3 are based on the coincidence relations and deduced multipolarities.

By gating on the 252 keV line in our $\gamma - \gamma$ matrix, we found the $\alpha_K = 0.4(1)$ for the 170.4 keV γ-ray by comparing the intensities of Eu K X-rays to the 170.4 keV photons. This is consistent with a parity conserving M1 (E2) transition. It is consistent with the spin assignment of 5^- for ^{140m1}Eu [1,3,4] and the $I^\pi = 6^-$ found in Ref. [4] for the $X+170.4$ keV level. The level at $X+361.5$ keV was found to have an $I^\pi = 7^-$ in Ref. [4], and decay via the E2, 361.5 keV transition to the 5^- isomer. The calculated α_{total}(361.5,E2)= 0.03. Gating on the 361.5 keV line, we measured $\alpha_K = 0.3(1)$ for the 98.1 keV line which is consistent with an E1 transition (see Table 6.1). By comparing the total intensity of the 190.8 keV line to the difference of the total intensity between the 98.1 and the 361.5 keV lines, we determined the $\alpha_{total}(190.8) = 0.21(7)$ which is consistent with a mixed M1+E2 character. This E1 assignment for the 98.1 keV line defines the spin and parity of ^{140m2}Eu as 8^+. This assignment agrees with Ref. [3], but differs from the $I^\pi = 9^+$ adopted in Ref. [4].

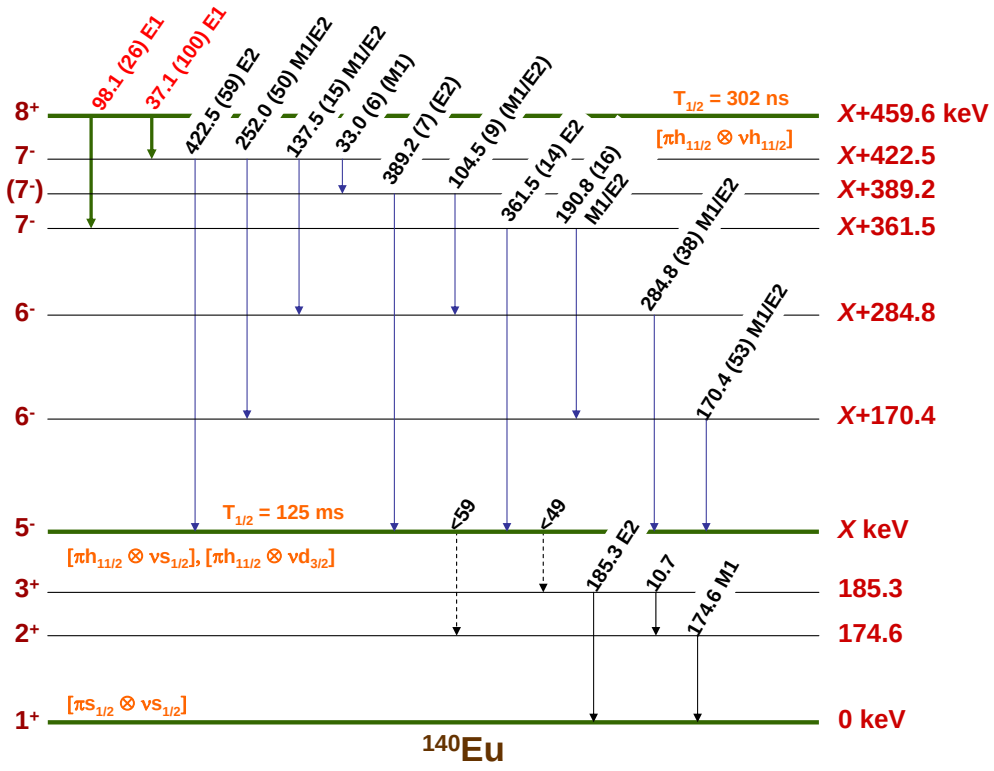

Figure 6.3: Proposed ^{140}Eu level scheme from this work. The 125 ms, $I^{\pi} = 5^{-}$ isomer in the decay scheme was copied from Ref. [1] and was not directly studied in this work. The energy of this isomer, X, was reported in Ref. [1] to be < 234 keV.

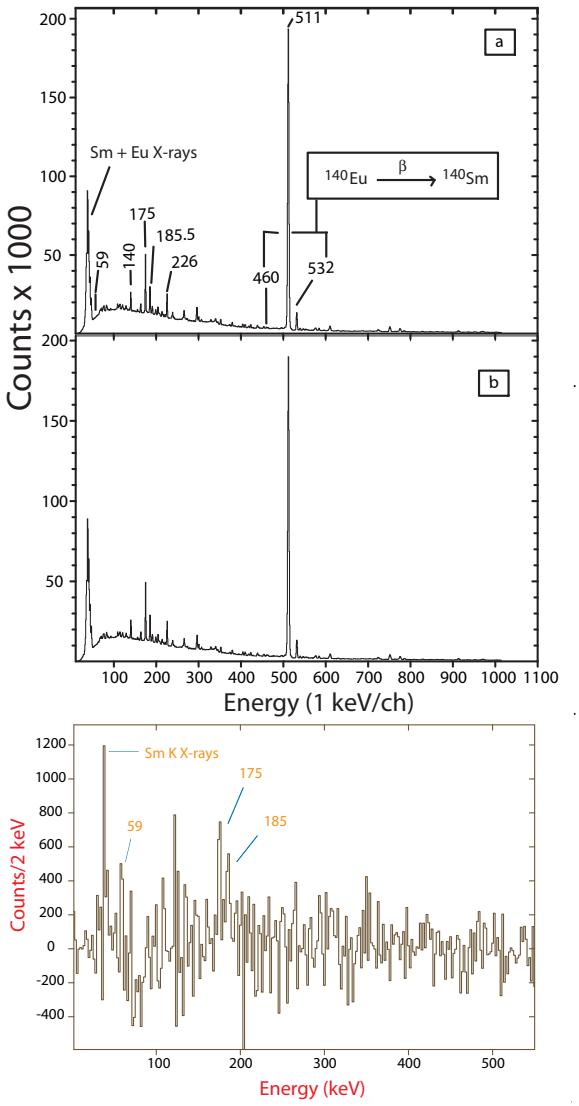

Figure 6.4: Top: Gamma rays following the decay of the 302 ns isomer, ^{140m2}Eu, within (a) 1-200 ms (b) 200-400 ms. The presence of the 460 and 532-keV lines which are the result of the β-decay of ^{140}Eu to ^{140}Sm assures that the method used for the correlation of ^{140m2}Eu and ^{140m1}Eu is correct.
Bottom: Gamma rays following the decay of the 302 ns isomer (^{140m2}Eu) within the first 200 ms, less those from the 200-400 ms time window after the isomeric decay. The presence of the 175 and 185 keV lines indicates that the 302 ns ^{140m2}Eu isomeric decay feeds the 125 ms ^{140m1}Eu level. All other lines are believed to be the result of random accidental correlation (see text).

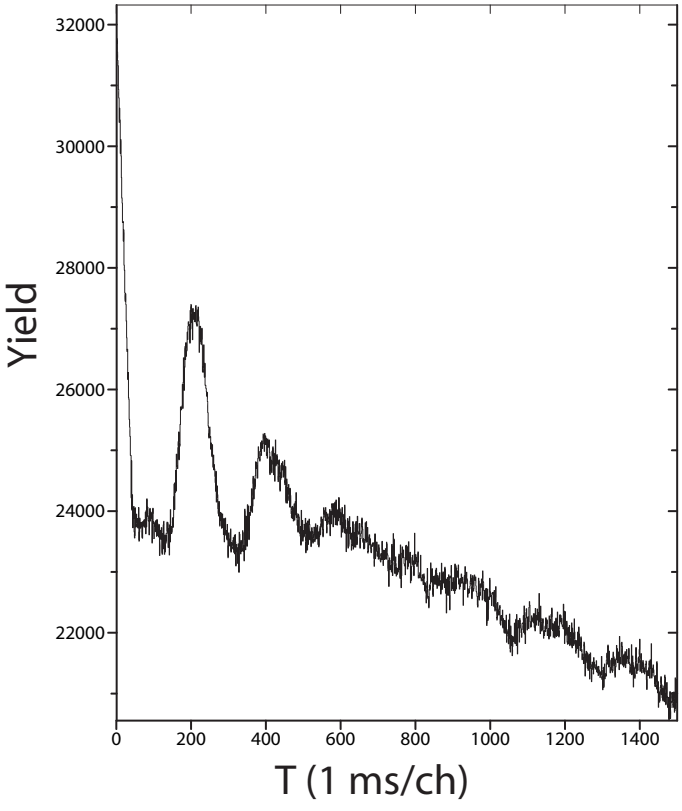

Figure 6.5: Four clover time spectrum obtained during the experiment used for the study of the correlation between ^{140m2}Eu and ^{140m1}Eu. The fluctuating behavior of the time decay is caused by the an acquisition system shutdown while data are transmitted to the acquisition computer.

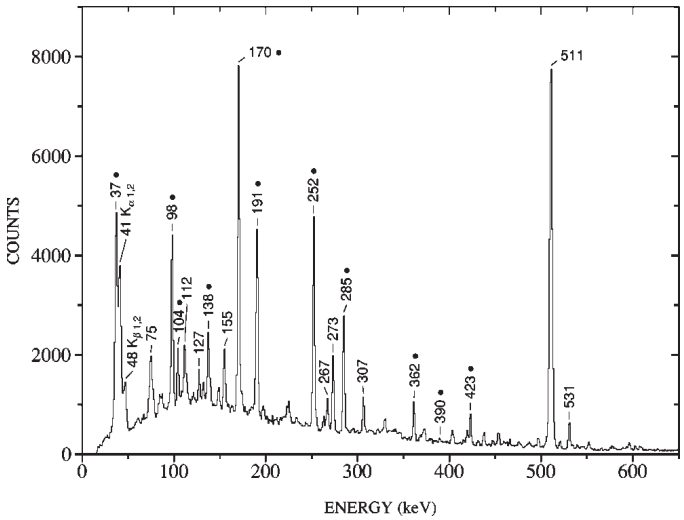

Figure 6.6: Spectrum of γ-rays taken from Fig. 1 in Ref. [3] for γ-rays deexciting ^{140m2}Eu. This spectrum is very similar to our γ-ray spectrum but the 33.0 keV line was not observed in this figure indicating that the detection threshold was too high.

Besides the transitions showing the decay pattern corresponding to 302 ns half-life, no other half-life component was observed for the gamma lines deexciting the ^{140m2}Eu isomer. This indicates that the multipolarity of these transitions is lower than 3. The multipolarity E3 or M3 would make the half-lives of the parent states in the millisecond (or longer) range, or will reduce the gamma intensity of the considered transition competing with lower multipolarity ones to the non-detectable level.

The decay of the $X + 459.6$ keV level populated by the single isomeric transition at 37.1 keV is followed by the transitions of 33.0, 104.5, 137.5, 170.4, 252.0, 284.8, 389.2, and 422.5 keV. For the multipolarity < 3, the total intensity of these transitions are too small to account for our observed intensity for the 37.1 keV transition for any multipolarity other than E1 ($\alpha_{total} = 0.7$) as compared to α_{total}(M1)= 5 and α_{total}(E2)= 139. Our finding disagrees with the relative intensity of the 37.1 keV line and the assignment of M1 multipolarity proposed in Ref. [3]. The 37.1 keV E1 line defines the spin and parity of 7^- for the $X + 422.5$ keV level. As a consequence, we assign only negative parity to the levels between the two ^{140}Eu isomers, in contrast to Ref. [3] and in agreement with Ref. [4]. The energy threshold for detecting γ-rays in our experiment was lower in comparison to Ref. [3], and even allowed us to detect the 33.0 keV transition. The line at 33.0 keV was expected but not directly observed in Ref. [3] as shown in Fig. 6.6. The higher energy threshold might be responsible for an artificial reduction of the 37.1 keV γ-ray intensity observed in Ref. [3].

The total conversion coefficient of 0.11(5) deduced for the 252.0 keV line, obtained by comparing its γ-ray intensity to that of the 170.4 and 190.8 keV lines, agrees with M1+E2 character for this transition between the $X + 422.5$ and the $X + 170.4$ keV levels. The E2

Table 6.2: Total incoming and outgoing γ intensities of the intermediate states in the decay of ^{140m2}Eu, $I^\pi = 8^+$, $T_{1/2} = 302(4)$ ns.

Level (keV)	I^π	Incoming I_{total}(%)	Outgoing I_{total} (%)
X+459.6	8^+	N/A	100(8)
X+422.5	7^-	83(8)	95(16)
X+389.2	(7^-)	24(12)	17(4)
X+361.5	7^-	17(2)	17(4)
X+284.8	6^-	26(4)	21(9)
X+170.4	6^-	38(14)	37(11)
X	5^-	99(15)	N/A

multipolarity can be assigned to the 422.5 keV deexcitation between the $X + 422.5$ keV level and the $I^\pi = 5^-$ ^{140m1}Eu.

$I^\pi = 6^-$ was found in Ref. [4] for the $X + 284.8$ keV level. It agrees with our measured value of $\alpha_K = 0.08(3)$ for the 284.8 keV line, obtained by gating on the 104.5 keV line, which indicates a mixed M1+E2 multipolarity. It also establishes the sequence of the M1+E2 137.5 keV line deexciting the $X + 422.5$ keV 7^- level, and the 284.8 keV line feeding the ^{140m1}Eu isomer - opposite to the placement adopted in Ref. [3]. We place the observed 33.0 keV (M1) transition as deexciting the 7^- state at $X + 422.5$ keV, to the new (7^-) level at $X + 389.2$ keV based on the transition intensity balance and consistency of the adopted transition multipolarities. The E2 multipolarity assignment for the 33.0 keV line would not allow for the observed γ-ray intensity.

The multipolarities listed for the transitions following ^{140m2}Eu decay in the decay scheme, see Fig. 6.3, offer a consistent picture of incoming and outgoing intensities for each intermediate level, see Table 6.2. Each cascade connecting the two isomeric states is consistent with the spin difference of 3 and opposite parities of the isomers.

We can explore other possibilities for the spins and parities of the intermediate states in ^{140m2}Eu. If the 361.5 keV line were an E1 transition with a calculated $\alpha_{tot} = 0.01$, the $X + 361.5$ keV level would have a positive parity. We would deduce an $\alpha_{tot} = 0.25$ for the 190.8 keV line which indicates an E2 transition. The sequence of M1/E2 and E2 multipolarities for the 170.4 and 190.8 keV lines, respectively, would yield a negative parity of the $X + 361.5$ keV level. Since these two assignments of the 361.5 and the 190.8 keV lines now contradict each other, this scenario has to be ruled out.

If the 361.5 keV line were an M1 transition with a calculated $\alpha_{tot} = 0.055$, then α_{tot}(190.8 keV) would come out to be 0.19 which is closest to an E2 transition. However, an M1 transition for the 361.5 keV line would not be sufficient to change the spin of the $X + 361.5$ keV level enough to be consistent with the sequence of M1/E2 and E2 for the 170.4 and 190.8 keV transitions, respectively, since with this sequence the $X + 361.5$ keV level would have to be at least an $I^\pi = 7^-$. Hence this scenario is ruled out as well.

If we now take the 361.5 keV line to be an E3 transition with a calculated $\alpha_{tot} = 0.13$ then α_{tot}(190.8 keV) would come out to be 0.19 which again is an E2 transition and would cause a contradiction of the parity of the $X + 361.5$ keV level with the sequence of M1/E2 and E2 for the 170.4 and 190.8 keV transitions, respectively. This scenario is ruled out.

The only scenario that does not cause a conflict on the $X + 361.5$ keV level other than the 361.5 keV line being an E2 transition is if the 361.5 keV line were an M2 transition with calculated $\alpha_{tot} = 0.21$. This results in an $\alpha_{tot} = 0.06$ for the 190.8 keV line which is consistent with an E1 transition. This would make the spin and parity of the $X+361.5$ keV level an $I^{\pi} = 7^{+}$ and the $X + 459.6$ keV level an $I^{\pi} = 8^{-}$ with the 98.1 keV line being an E1 transition. Such spin and parity of the $X + 459.6$ keV level is not a result of the coupling of the $h_{11/2}$ proton to the $h_{11/2}$ neutron. However, let us continue with the rest of the level scheme using the 361.5 keV line as an M2 transition. Then the measured α_{tot} for the 252.0 keV line would come out to be 0.16 which is consistent with an M1 transition where the calculated α_{tot}(252.0 keV)= 0.14, 0.02, 0.05, and 0.07 for an M1, E1, E3, and M2 transitions respectively. Now no matter what the multipolarity of the 422.4 and 389.2 keV lines are, the measured α_{tot} for the 37.1 keV line would vary from 0.7 to a maximum of 1 which is consistent with an E1 transition. The sequence of M1/E2, M1, and E1 multipolarities for the 170.4, 252.0, and 37.1 keV lines, respectively, indicates a positive parity for the $X + 459.6$ keV level starting form $I^{\pi} = 5^{-}$ for the 234 keV level. This contradicts the sequence of M2 and E1 for the 361.5 and 98.1 keV lines, respectively. So this rules out this final scenario. And as we go on trying different multipolarities for the 361.5 keV we would always end up with a contradiction at some point with the rest of the transitions except when the 361.5 keV line is an E2 transition as mentioned in the first scenario. It is difficult to determine accurately the multipolarities of all the lines in ^{140m2}Eu with our current data. The adopted multipolarities for the transitions in ^{140m2}Eu are shown in Fig. 6.3 and listed in Table 6.1.

Results from the neighboring odd-N even-Z nuclei, such as ^{139}Sm [52], suggest that the most important contribution for the negative parity states comes from the $h_{11/2}$ neutron orbital where yrast bands are built on top of it. In the odd-Z even-N nuclei, such as ^{141}Eu [53, 54], the proton is a decoupled $h_{11/2}$. Such a pattern of single-particle levels suggests for neighboring odd-Z odd-N nuclei the presence of the $\pi h_{11/2} \otimes \nu h_{11/2}$ and the $\pi h_{11/2} \otimes \nu s_{1/2}$ configurations at low energies. We interpret the ^{140m1}Eu metastable state as arising from the coupling of the $h_{11/2}$ proton to an $s_{1/2}$ neutron, with possible contribution of the $h_{11/2}$ proton coupled to the $d_{3/2}$ neutron leading to an $I^{\pi} = 5^{-}$ state. The 1^{+} ground-state results from the $\pi d_{5/2}$ and $\nu d_{3/2}$ coupling. The $I^{\pi} = 5^{-}$ identified for the 125 ms isomeric state [1], the spin difference of 3, and parity change deduced for the transitions connecting the two isomers are consistent with the spin and parity of 8^{+} for ^{140m2}Eu. The wave function of ^{140m2}Eu is likely to be dominated by the $\pi h_{11/2} \otimes \nu h_{11/2}$ component, as was also recognized in Ref. [3, 4].

The Weisskopf estimation for the half-life of the 37.1 keV and 98.1 keV E1 transitions are 5 ps and 0.27 ps, respectively. The retardation factors are about 1.2×10^{5} and 8.7×10^{6}, respectively.

In Ref. [3], the isomer tagging technique [6] was applied and a decay scheme of ^{140}Eu similar to our proposed decay scheme was established, see Fig. 6.7. In Cullen's work [3], the values of $I^{\pi} = 8^{+}$ was proposed for the $\pi h_{11/2} \otimes \nu h_{11/2}$ metastable state. However, as mentioned above, in Ref. [3] the 37.1 keV line was assigned a multipolarity of M1. There was also a difference in the decay sequence of the 284.8, 33.0, 104.5, 137.5, and the 389.2 keV γ-ray transitions between our work and that of Ref. [3]. This difference is insignificant and either way may be correct for now given the quality of the data we both have. They too were not able to assign the exact spin and parity to all of the levels of ^{140m2}Eu except via scientific predictions and assumptions similar to our way of estimating the spins and parities. The assignments were deduced from a consideration of the total transition intensity balance through a particular level based on measured and calculated internal conversion coefficients.

The isomer tagging technique is a every efficient way in studying isomers in the mass 130-140 region which is difficult to access and study with heavy-ion fusion evaporation reaction methods with stable beam and target combination, since the evaporation residues which are less neutron deficient, will be produced with larger cross sections than the nuclei of interest.

The ^{140}Eu study in Ref. [4] aimed at searching for yrast bands. They deduced the decay scheme via an in-beam experiment, see Fig. 6.8. They proposed a spin and parity of $I^{\pi} = 9^{+}$ for the $\pi h_{11/2} \otimes \nu h_{11/2}$ meta-stable state but they did not actually observe the isomer in their data directly. However, they show some γ-lines decaying to the $I^{\pi} = 5^{-}$ ^{140m1}Eu that are consistent with the γ-ray transitions we observed in the decay of ^{140m2}Eu to ^{140m1}Eu. Specifically, they show the 285 keV line feeding the $I^{\pi} = 5^{-}$, ^{140m1}Eu as was also proposed in our decay scheme, see Fig. 6.3.

The work done in Ref. [3, 4] was very significant in this mass region as they performed theoretical calculations using the Total Routhain Surface (TRS) and Woods-Saxon cranked-shell model (CSM) methods [55]. The TRS calculations in Ref. [3] predict that ^{140}Eu has a triaxial nuclear shape with $\beta_2 = 0.185$, $\beta_4 = -0.024$, and $\gamma = -25.5^{o}$. They performed the CSM calculation at those deformation values. The γ deformation was responsible for the signature splitting of the single-particle orbits for the $h_{11/2}$ protons and the $h_{11/2}$ and $f_{7/2}$ neutrons.

6.2 ^{142}Tb

^{142}Tb and ^{144}Ho have been investigated thoroughly in the past, both experimentally [1, 6] and theoretically [55]. Level schemes have been established, especially for the higher spin levels [56]. However, it was difficult to make conclusive spin assignments for the intermediate isomers in ^{142}Tb and ^{144}Ho.

The lighter terbium isotopes, ^{140,141}Tb, are predicted to have a prolate deformation ($\epsilon_2 = 0.1 - 0.2$) [54, 57] with a sharp change to oblate deformation at ^{142}Tb. Similarly, the lighter holmium isotopes, ^{141,143}Ho, are predicted to have a prolate deformation with $\beta_2 \approx 0.29$ [58–60] while ^{145}Ho [61] is predicted to be weakly deformed and ^{147}Ho [9] to be spherical with a sharp change from prolate to oblate at ^{144}Ho. As a matter of fact,

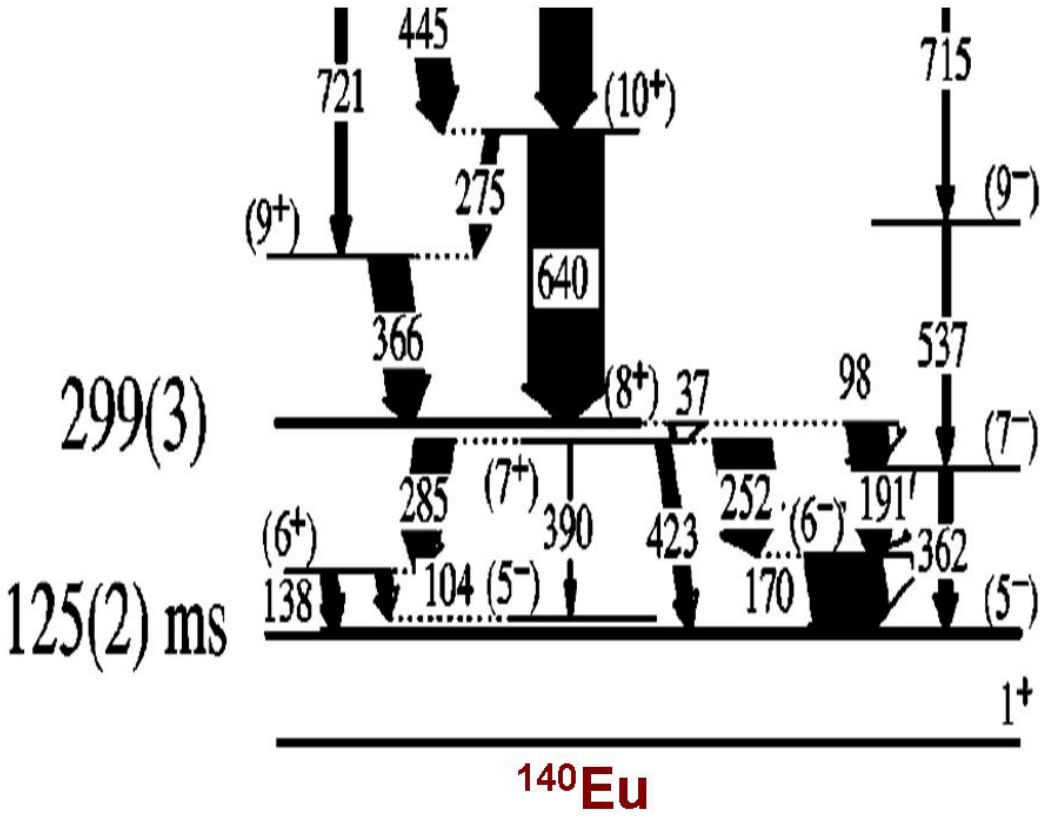

Figure 6.7: Proposed ^{140}Eu decay scheme by Cullen *et al.* [3]. It is similar to our proposed decay scheme with the difference in the decay sequence of the 284.8, 33.0, 104.5, 137.5, and the 389.2 keV γ-ray transitions.

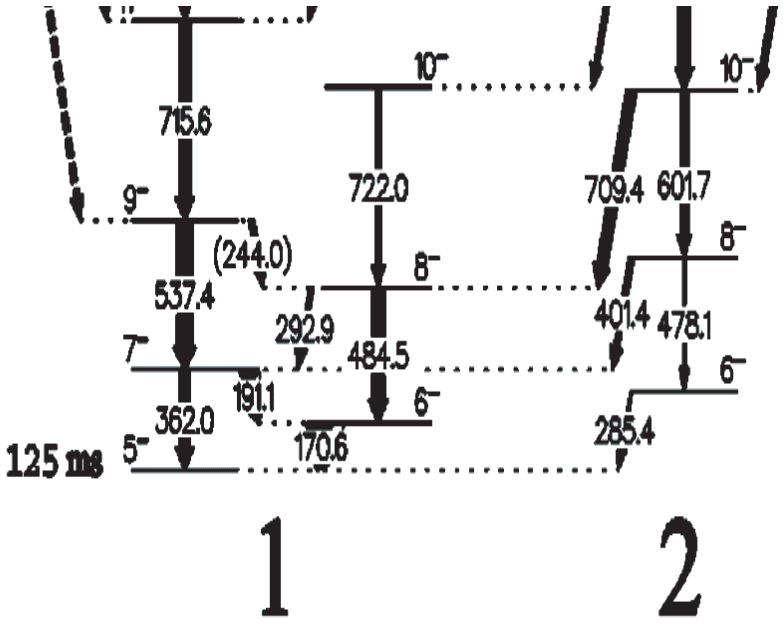

Figure 6.8: Prompt γ-rays feeding ^{140m1}Eu established by Hecht *et al.* [4]. The γ-rays dexciting from ^{140m2}Eu and feeding ^{140m1}Eu are similar to our proposed decay scheme for ^{140m2}Eu. The difference between our proposed decay scheme and Hecht's data is the spin and parity assignment of the $X + 459.6$ keV level in ^{140m2}Eu. An $I^{\pi} = 9^{+}$ was proposed in Ref. [4] while an $I^{\pi} = 8^{+}$ was proposed in our work.

changes in deformation occur near the $N = 77$ region. This change from prolate to oblate deformation is believed to be responsible for the increase in the energy gap between the $11/2^-$ and $1/2^+$ states between the $N = 79$ and $N = 77$ isotones in Ce, Nd, and Sm [54,57]. Nazarewicz *et al.* carried out theoretical calculations of the total Routhian Surface (TRS) and Wood-Saxon Cranked-Shell-Model (CSM) calculations to see how the signature splitting behaved for the $h_{11/2}$ protons and the $h_{11/2}$ and $f_{7/2}$ neutrons for ^{142}Tb and ^{144}Ho [55]. They expected rotational bands built on top of these orbits to form decoupled, $\delta I = 2$ bands with one signature of the configuration being more favored than the other. The discussion of the possibly triaxial shapes of ^{142}Tb and ^{144}Ho in their theoretical work referring to the aligned angular momentum dependence on rotational frequency is detailed and precise.

Two isomeric levels were reported earlier for ^{142}Tb: the 15(4) μs ^{142m2}Tb at 620 keV [5,6] and the 303 ms ^{142m1}Tb at 280 keV above the $I^\pi = 1^+$ ground-state [1].

The data collected with the RMS optimized for $A/Q = 142/24$ recoils revealed γ-lines of 178, 280, and 284 keV known to be transitions in ^{142}Eu [1]. The K-electron energies at 231 and 235 keV for the 280 and 284 keV transitions, respectively, were detected in the conversion electron spectrometer. The conversion coefficients of the 280 and 284 keV transitions were previously measured by Firestone *et al.* [1] in the study of the β decay of ^{142}Gd ($T_{1/2} = 70$ s). Using this information, we found that the effective BESCA efficiency was about 0.32% during the $A = 142$ measurement for the electron energies from about 50 keV to 1 MeV, i.e., it was lower by a factor of five in comparison to the off-line BESCA efficiency value of 1.6%. One can argue that the recoil implantation area on the tape was broad compared to the small open electron source used for off-line calibration and likely it was shifted from the central position on the 35 mm tape collector away from the BESCA 180 mm^2 SiLi detector. The internal efficiency calibration of BESCA was used to verify the values of the conversion coefficients for transitions in ^{142}Tb by comparing the relative intensities of K and L conversion electron lines.

The γ-ray spectrum resulting from the decay of ^{142m2}Tb, measured within a 90 μs time correlation window of the MCP recoil signals is shown in Fig. 6.9. It has considerably better statistics in comparison to the data presented in Ref. [5, 6]. We obtained a half-life of 25(1) μs, see Fig. 6.10, from the decay pattern of the summed 137.7, 165.4, 219.4 and 302.9 keV lines. Based on collected γ-ray spectra, new γ-lines with a half-life of 25 μs were observed (see Fig. 6.9) in coincidence with the known transitions given in Ref. [6]. The new transitions have the energies of 32.2, 81.5, 115.8, 197.6, 335.1 and 340.1 keV. Fig. 6.11 shows the γ-ray transitions in coincidence with the 197.6 keV line along with the decay pattern of the 197.6 keV line. The γ-ray spectrum in coincidence with the 32.2 keV line is shown in Fig. 6.12(a) while Fig. 6.12(b) shows the γ-ray transitions in coincidence with the 302.9 keV line which represents the strongest line in ^{142m2}Tb. The low energy lines at 24 keV and 27 keV shown in Fig. 6.12(b) result from the fluorescence from indium material present next to the Ge crystal in the LOAX detector.

We extended the decay scheme of Ref. [6] for ^{142m2}Tb as shown in Fig. 6.13. To account for the microsecond half-life of the isomer, none of the transitions depopulating ^{142m2}Tb can have a multipolarity higher than 2 as any γ-ray with a multipolarity of 3 and higher

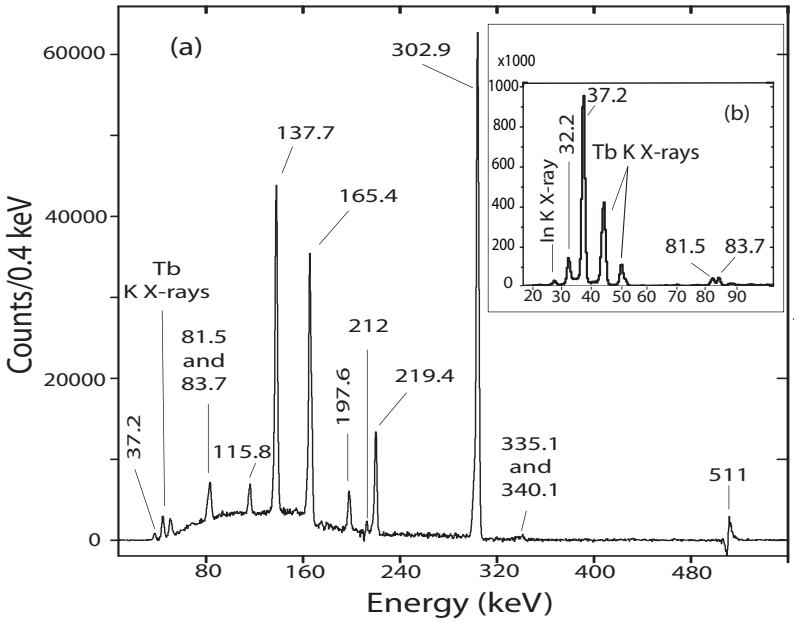

Figure 6.9: Spectrum of γ-rays measured by (a) two Clover detectors and (b) LOAX detector appearing within 90 μs after implantation of mass 142 recoils. Indium is the type of material surrounding the detectors. In K X-rays appear as a result of the fluorescence triggered by the low energy γ-rays deexciting ^{142m2}Tb.

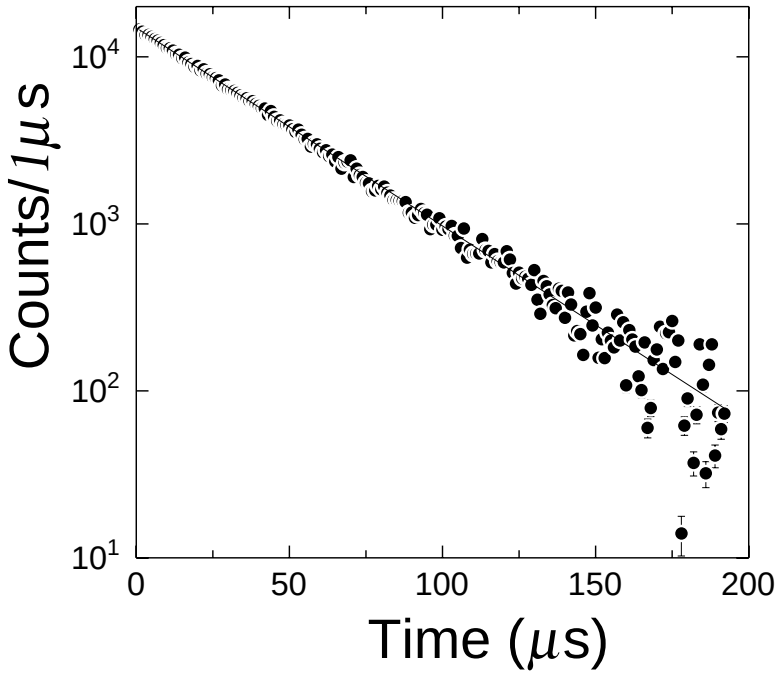

Figure 6.10: Decay pattern of the sum of the 137.7, 165.4, 219.4, and 302.9 keV γ-ray transitions after subtracting the appropriate background. The fitted curve yields a half-life of 25(1) μs for ^{142m2}Tb.

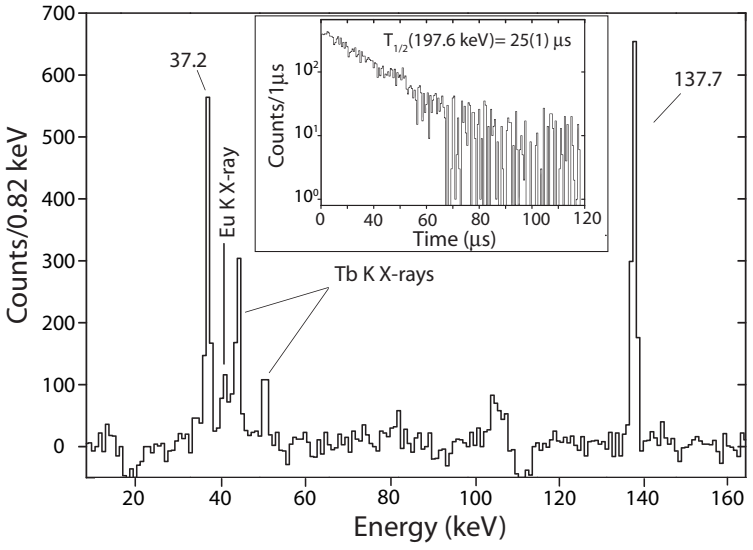

Figure 6.11: γ-ray spectrum in coincidence with the 197.6 keV line. Also shown is the decay pattern of the 197.6 keV line in ^{142m2}Tb.

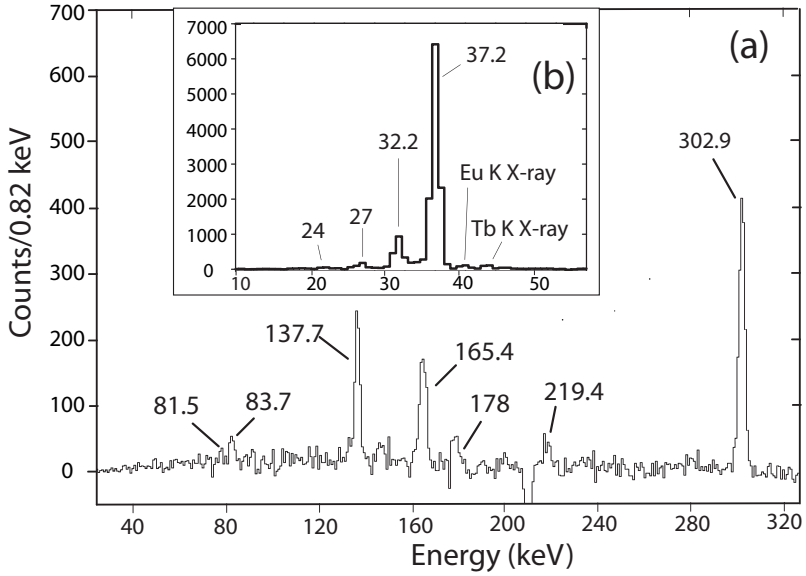

Figure 6.12: γ-ray spectrum in coincidence with (a) the 32.2 keV line, and (b) the 302.9 keV line in ^{142m2}Tb. The 24 and 27 keV lines are the In K X-rays. The 178 keV line represents the strongest line in ^{142}Eu which contaminates our data.

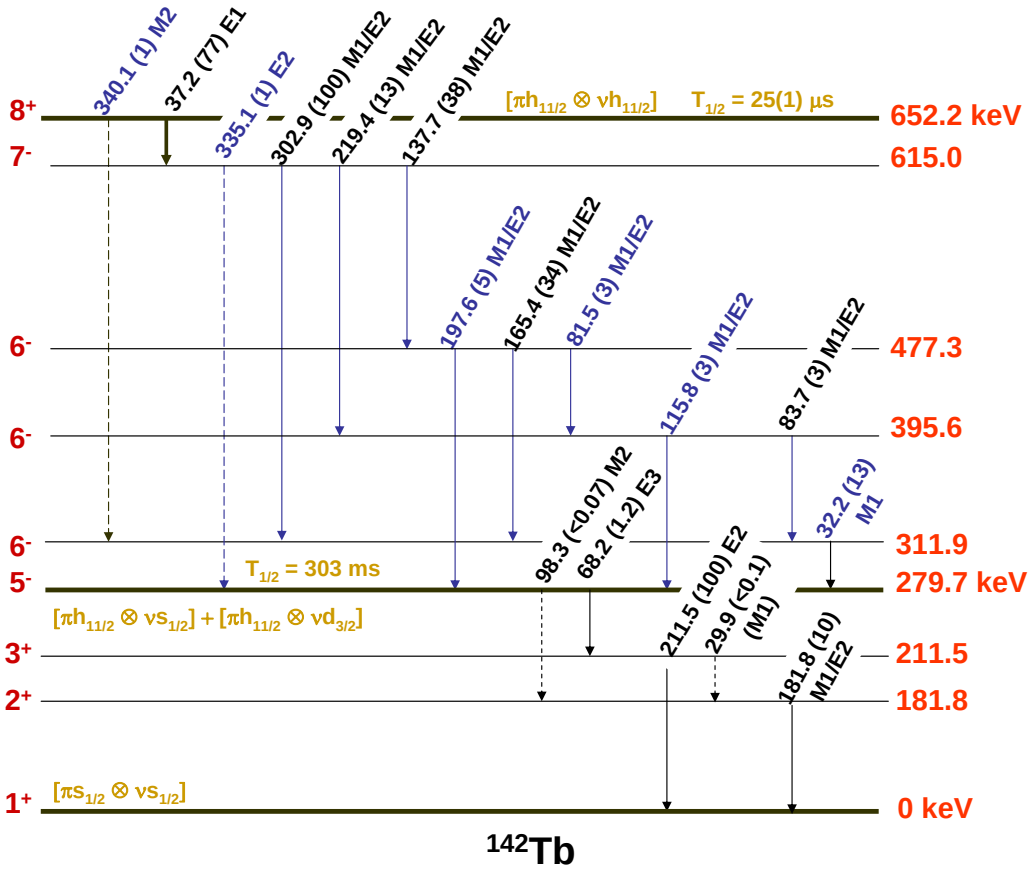

Figure 6.13: ^{142}Tb level scheme. The values in parentheses are the relative intensities.

will result in a Weisskopf partial half-life in the milli-second range and up to 2.1×10^{14} s for an M4 transition of the 32.2 keV line.

The measured conversion electron spectra, see Fig. 6.14, allowed us to determine the multipolarities of several transitions. The experimental K/L ratios and the conversion coefficients given in Table 6.3 were used to establish multipolarities for the 137.7, 165.4, 197.6, 219.4 and 302.9 keV transitions deexciting ^{142m2}Tb. The calculated values of K/L and the conversion coefficients are given in Table 6.4. No electrons of energies below 85 keV or for very low intensity γ-ray energies, such as the 335.1 and the 340.1 keV γ-ray transitions, were detected.

The 129 and 159 keV electron peaks, being the L-conversion electrons for the 137.7 and 165.4 keV γ-lines, respectively, in this μs range have some contamination from the longer lived ^{142m1}Tb and from ^{142}Eu. The K-conversion electron energies of the 181.8 and 211.5 keV γ-lines in ^{142m1}Tb are 130 and 160 keV respectively. The K-conversion electron energy for the 178 keV γ-line in ^{142}Eu is 129.5 keV. With the conversion coefficient of the 178 keV line being known [1], and that of the 181.8 and 211.5 keV ones now being measured (see below), we were able to determine how many conversion electrons in the 129 and 159 keV peaks actually did belong to the 137.7 and 165.4 keV L-conversion lines in ^{142m2}Tb.

From the transition intensity balance, the multipolarity of M1, E1, M1 and M1+E2 was deduced for the 32.2, 37.2, 81.5 and 83.7 keV lines, respectively. We deduced α_{total}(81.5 keV)= 3.4(9) by comparing its intensity to that of the 137.7, 165.4, and 197.6 keV lines. This value of α_{total}(81.5 keV) is consistent with a mixed M1+E2 character. We measured α_{total}(83.7 keV)= 6.3 ± 2.7 by comparing its intensity to that of the 81.5, 219.4, and 115.8 keV lines. The α_{total} for the 83.7 keV transition is consistent with E2, but a M1+E2 mixture cannot be ruled out. The M1+E2 character of the 115.8 keV line fixes the spin and parity of the 395.6 keV level at 6^-. By comparing the intensity of the 32.2 keV line to that of the 302.9, 165.4, 83.7, and 340.1 keV lines, we measure α_{total}(32.2 keV)= 14.6 ± 7.6. This is consistent with an M1 multipolarity (see Table. 6.4). The M1 character of the 32.2 keV lines allows for a spin and parity assignment of 6^- to the 311.9 keV level. The $I^\pi = 6^-$ of the 311.9 and 395.6 keV levels are consistent with the M1+E2 character of the 83.7 keV line. Starting from the $I^\pi = 5^-$ level at 279.7 keV, the sequence of M1, M1+E2, and E1 for the 32.2, 302.9, and 37 keV lines, respectively, leads to an assignment of $I^\pi = 8^+$ for the $\pi h_{11/2} \otimes \nu h_{11/2}$ ^{142m2}Tb isomer. Weak gamma lines at 335.1 and 340.1 keV, indicated by the dashed lines in Fig. 6.13, result at least partially from summing of stronger transitions with the 32.2 and 37.2 keV lines. The 340.1 keV line can only have the parity changing M2 character while the 335.1 keV line can only be assigned the parity conserving E2 character as shown in Fig. 6.13. The mixed multipolarities of M1/E2 observed for the 137.7, 165.4, and 302.9 keV lines agree with the level scheme displayed in Fig. 6.13 and the decay properties listed in Table 6.3. The level intensity balances of all the levels in ^{142m2}Tb are listed in Table 6.5.

The measurements of the properties of the transitions following the decay of the 303 ms isomer were more difficult. The useful range for recoil-decay correlations discriminating long-lived activities was limited to a few milliseconds because of the implantation rate of

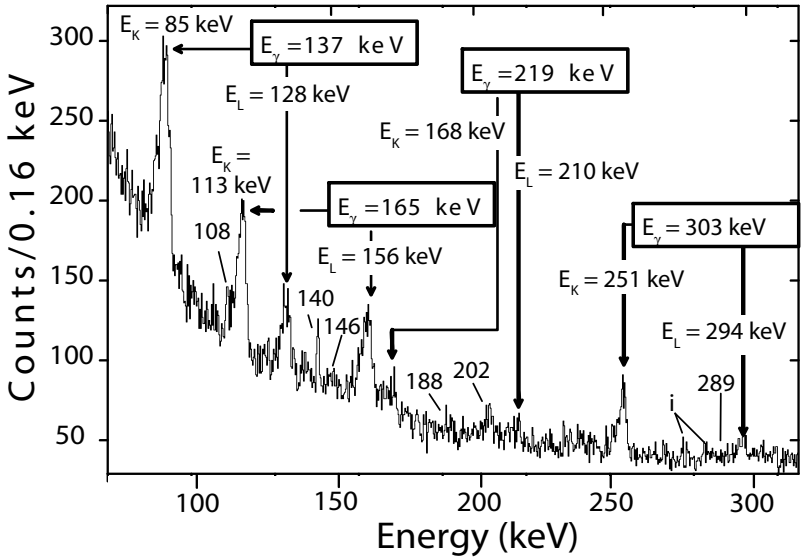

Figure 6.14: Conversion electron data measured by BESCA in the first 90 μs after the implantation of mass 142 recoils. The 108 keV line is the L conversion line for the 115.8 keV γ-ray. The 146 and 188 keV lines are the K and L lines for the 197.6 keV γ-ray transition. The 140 keV line is just the 137.7 keV γ-ray shifted by 2-3 channels. The 204 keV line is the L-conversion line for the 211.5 keV γ-ray. The lines labeled "i" are impurities from ^{142}Eu. They are the 273 and 277 keV L conversion lines for the 280 and 284 keV γ-ray transitions in ^{142}Eu which are among the strongest lines in ^{142}Eu.

Table 6.3: Relative intensities, K/L values, conversion coefficients and transition multipolarities deduced for the isomeric decays in ^{142}Tb. The upper part represents the transitions deexciting the $\pi h_{11/2}\nu h_{11/2}$ ^{142m2}Tb, $T_{1/2} = 25$ μs, $I^{\pi} = 8^{+}$. The lower part represents the transitions deexciting the $\pi h_{11/2}\nu s_{1/2}$ ^{142m1}Tb, $T_{1/2} = 300$ ms, $I^{\pi} = 5^{-}$.

E_{γ}	Rel. I$_{\gamma}$ (%)		K/L	α_K or α_{Total}	α_L	Adopted	I$_{total}$
(keV)	Present work	literature [a]	(exp)	(exp)	(exp)	Multipolarity	(this work)
32.2(3)	13(1)	N/A		$\alpha_T = 14.6(76)$		M1	178(12)
37.2(3)	77(6)	81(25)		$\alpha_T = 1.5(5)$		E1	196(11)
81.5(3)	3(1)	N/A		$\alpha_T = 3.6(9)$		M1	15(3)
83.7(3)	3(1)	N/A		$\alpha_T = 6.3(27)$		M1/E2	15(3)
115.8(3)	3(1)	N/A			0.38(3)	M1/E2	5(1)
137.7(3)	38(3)	33(4)	5.1(2)	$\alpha_K = 0.53(1)$	0.10(2)	M1/E2	71(6)
165.4(3)	34(3)	34(4)	5.0(2)	$\alpha_K = 0.33(1)$	0.07(1)	M1/E2	51(7)
197.6(3)	5(1)	N/A	4.2(6)	$\alpha_K = 0.23(2)$	0.06(4)	M1/E2	7(1)
219.4(3)	13(1)	1(1)	3.7(4)	$\alpha_K = 0.14(1)$	0.04(1)	M1/E2	16(4)
302.9(3)	100(8)	100(7)	4.8(3)	$\alpha_K = 0.05(1)$	0.011(1)	M1/E2	108(9)
335.1(6)	1(1)	N/A				E2	1(1)
340.1(6)	1(1)	N/A				M2	4(1)
29.9(9)	< 0.1	N/A				M1/E2	< 48
68.2(3)	1.20(10)	N/A		$\alpha_T = 98^{+23}_{-10}$		M2	119^{30}_{16}
98.3(9)	< 0.07	N/A		$\alpha_T <180$	<2	E3	< 3
181.8(3)	10(4)	6(2)	3.1(3)	$\alpha_K = 0.2(1)$	0.07(1)	M1/E2	14(6)
211.5(3)	100(6)	100(?)	2.6(1)	$\alpha_K = 0.11(1)$	0.04(1)	E2	199(13)

[a] The relative γ-ray intensities in the upper part of the table represnting the γ-ray transitions in ^{142m2}Tb are from Ref. [6]. The relative γ-ray intensities in the lower part of the table representing ^{142m1}Tb are from Ref. [1].

Table 6.4: Calculated K/L and α_K or α_{Total} for some of the trasnisitions deexciting ^{142m2}Tb and ^{142m1}Tb.

E_γ (keV)	K/L (calc)	α_K, α_{Total} (calc)
32.2(3)		α_T = 1.1(E1), 328(E2), 9.3(M1)
37.2(3)		α_T = 0.76(E1), 160.6(E2), 6.2(M1)
81.5(3)		α_T = 0.5(E1), 5.7(E2), 4.0(M1)
83.7(3)		α_T = 0.5(E1), 5.2(E2), 3.7(M1)
115.8(3)		α_L = 0.03(E1), 0.59(E2),0.18(M1)
137.7(3)	6.8(E1), 1.8(E2), 6.9(M1)	α_K = 0.11(E1), 0.48(E2), 0.76(M1)
165.4(3)	6.9(E1), 2.25(E2),6.9(M1)	α_K = 0.07(E1), 0.28(E2), 0.45(M1)
197.6(3)		α_K = 0.04(E1), 0.16(E2), 0.28(M1)
219.4(3)	0.03(M1), 3.1(E2),6.9(M1)	α_K = 0.03(E1), 0.12(E2), 0.21(M1)
302.9(3)	7.2(E1), 4.0(E2),7.0(M1)	α_K = 0.01(E1), 0.05(E2), 0.09(M1)
335.1(6)		α_T = 0.01(E1), 0.05(E2), 0.08(M1)
340.1(6)		α_T = 0.01(E1), 0.05(E2), 0.30(M2)
29.9(9)		α_T =11(M1)
68.2(3)		α_T = 12(E2), 93(M2),369(E3)
98.3(9)		α_T = 48(E3),23(M2),182(M3)
181.8(3)	7.0(E1), 2.5(E2),6.9(M1)	α_K = 0.05(E1), 0.2(E2), 0.4(M1)
211.5(3)	7.0(E1), 3.0(E2), 6.9(M1)	α_K = 0.04(E1), 0.13(E2), 0.23(M1)

Table 6.5: Total intensities of the intermediate levels in ^{142m2}Tb.

Level energy (keV)	I_{total} in (%)	I_{total} out (%)
279.7	200(14)	
311.9	184(14)	184(14)
395.6	29(5)	29(9)
477.3	71(6)	71(8)
615.0	196(11)	196(11)
652.2		200(11)

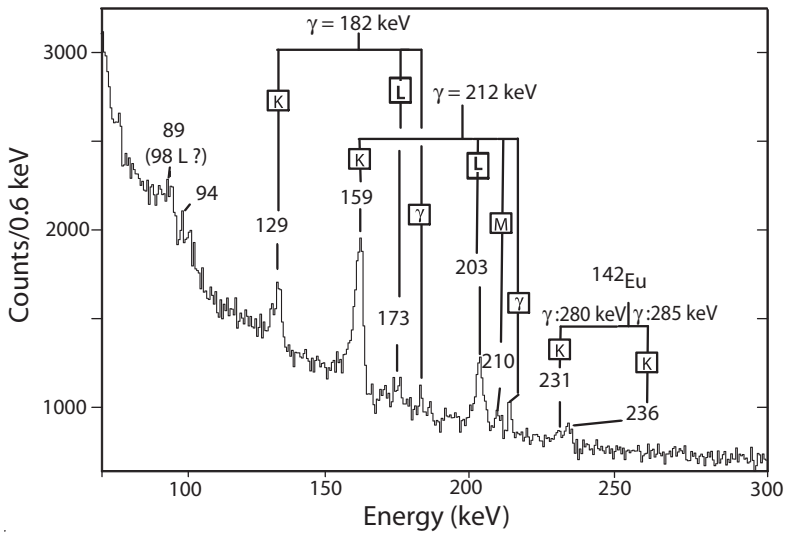

Figure 6.15: Conversion electron data measured by BESCA within the first 5 ms after a mass 142 recoil implantation.

about 200 pps. However, by applying the first 5 ms time gate after implantation, the conversion electron lines corresponding to the decay of ^{142m1}Tb were clearly identified, see Fig. 6.15. The γ-ray spectrum in this 5 ms window is shown in Fig. 6.16 and Fig. 6.17 while the γ-ray singles spectrum is shown in Fig. 6.18 with no time restrictions.

The conversion coefficients for the 181.8 and 211.5 keV transitions in ^{142m1}Tb were determined from the conversion electron data measured by BESCA and the γ-ray intensities of those transitions, see Table 6.3. The measurements allowed us to assign the multipolarity E2 to the 211.5 keV transition while the 181.8 keV transition has a mixed M1/E2 multipolarity. This points to a spin and parity of 3^+ and 2^+ for the levels at 211.5 and 181.8 keV, respectively, in agreement with Ref. [1]. The 68.2 keV line was observed in our LOAX and clovers spectrum. Its total intensity has to be at least equal to that of the 211.5 keV transition and should not be higher than the total intensity of both 211.5 and 181.8 keV transitions. The respective total conversion coefficient for the 68.2 keV line is therefore $\alpha_{total} = 98^{+23}_{-10}$ indicating an assignment of M2 multipolarity to this transition. This supports the $I^\pi = 5^-$ assignment for the 279.7 keV isomeric level in ^{142m1}Tb. We calculated α_{tot} experimentally for the 68 keV line using the equation:

$$\alpha_{tot}(68) = [\frac{I_{\gamma(212)}}{I_{\gamma(68)}}(1 + \alpha_K(212) + \alpha_L(212) + \alpha_M(212))] - 1 \qquad (6.1)$$

where I_γ is the γ-ray intensity and α is the electron conversion coefficient.

The presence of a 98.3 keV line in the decay scheme of ^{142m1}Tb [1], see Fig. 6.13, is not clear. The γ-ray transition at 98.3 keV was not observed in our γ-ray spectrum, thus, it

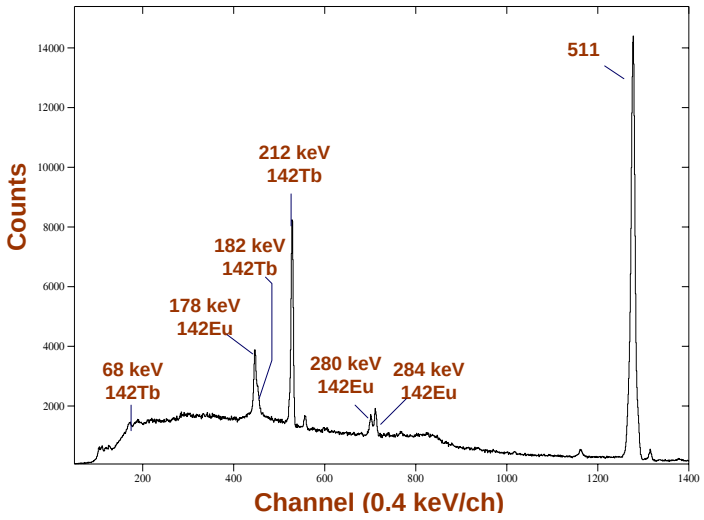

Figure 6.16: Spectrum of γ-rays (measured by the two clover detectors) appearing within 5 ms after implantation of $A = 142$ recoils. ^{142m1}Tb and ^{142}Eu γ-ray peaks appear in this spectrum. The RMS was optimized for $A/Q = 142/25$. The 178 keV γ-ray peak of ^{142}Eu and the 182-keV γ-ray peak of ^{142}Tb are not well resolved here.

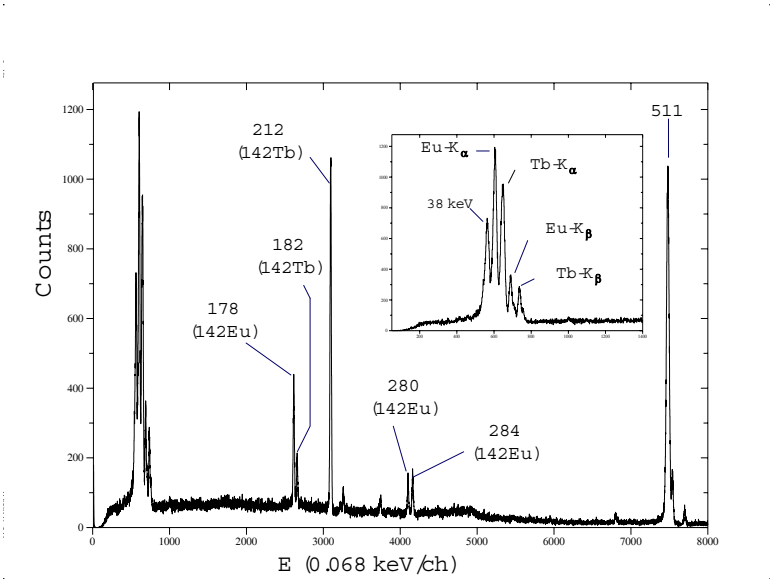

Figure 6.17: Spectrum of γ-rays (measured by the LOAX detector) appearing within 5 ms after implantation of $A = 142$ recoils. ^{142m1}Tb and ^{142}Eu γ-ray peaks appear in this spectrum. The RMS was optimized for $A/Q = 142/25$.

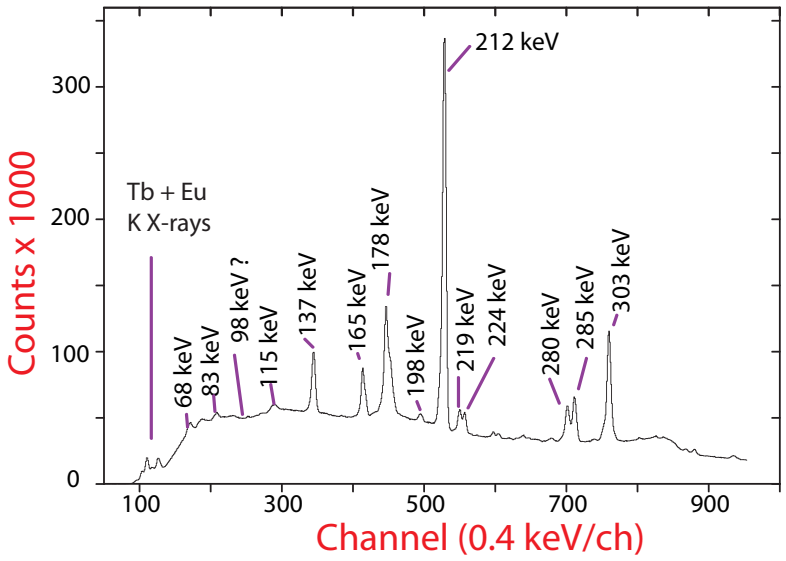

Figure 6.18: Singles γ-ray spectrum measured by the clover detectors after mass 142 implants without any time conditions. The position where the 98.3 keV γ-ray deexciting ^{142m1}Tb appears like a small valley.

must be strongly converted. The 98.3 keV peak was not observed in the γ-ray spectrum measured by the clovers, see Fig. 6.16, in the 5 ms range, nor in the γ-ray spectrum measured by the LOAX detector, see Fig. 6.17, which had better energy resolution than the clovers. We were not even able to see the 98.3 keV γ-ray deexciting ^{142m1}Tb in the singles γ-ray spectrum (see Fig. 6.18) which did not have any time restrictions on it. When gating on the 181.8 keV transition in ^{142m1}Tb as shown in Fig. 6.19, we still don't see any evidence for the existence of the 98-keV line.

Since the 181.8 keV level has an $I^\pi = 2^+$, the 98.3 keV line has to be an E3 to originate from $I^\pi = 5^-$ ^{142m1}Tb. The calculated α_{tot} for the 98.3 keV E3 transition is 49 with an α_L contribution of 34. This means that in order to account for the 181.8 keV line intensity, the 98.3 keV γ-peak would have about 700 to 800 counts and the L electron conversion peak would be much stronger than the one shown in Fig. 6.15. Unfortunately, the K electron energy for the 98.3 keV γ-ray in Tb is 46 keV. This is close to the energy of Eu K_β X-rays which are emitted by ^{142}Eu produced in the beta decay of ^{142}Gd ($T_{1/2} = 70$ s). And as mentioned above, no low energy electrons were detected by BESCA during our run. Measuring the number of counts at the energy of 98.3 keV in the LOAX spectrum gave us an upper limit of 920 counts. This is consistent with the calculated value of 760 counts for an E3 transition. A limit of $\alpha_{tot}(98.3 \text{ keV}) < 180$ could be derived assuming equal total intensities of 181.8 and 98.3 keV transitions.

The lack of evidence of the existence of the 98.3 keV transition leads us to place it in the ^{142}Tb decay scheme as a dashed line. A 29.9 keV transition was suggested in Ref. [1]. In fact, a 29.9 keV M1 transition originating from the 211.5 keV $I^\pi = 2^+$ state could account for the intensity of the 181.8 keV transition as postulated in Ref. [1].

The relative intensities of the 68.2, 181.8 and 211.5 keV γ-rays from the deexcitation of the ^{142m1}Tb isomer are listed in Table 6.3. The decay scheme of ^{142m1,m2}Tb with the multipolarities of the transitions, and spins and parities of the levels, is shown in Fig. 6.13.

The fact that we determined the multipolarity of the 211.5 keV line in ^{142m1}Tb to be an E2, as postulated in Ref. [1], provided some re-assurance about the internal BESCA efficiency measurement of 0.32%. The sequence of the E2 and M2 transitions of the 211.5 and 68.3 keV lines indicate a spin and parity of 5^- for ^{142m1}Tb.

The estimated Weisskopf partial half-life for the 37.2 keV E1 transition deexciting ^{142m2}Tb is 5 ps, while that of the 340.1 keV is 0.16 μs. A comparison to the experimental value indicates a retardation of about 1×10^7 for the half-life of the 37.2 keV transition.

6.3 ^{144}Ho

The 0.5 μs decay of the isomeric level and the excited levels built on this metastable state in ^{144}Ho were reported in Ref. [6]. We have observed four transitions, at 56.4, 59.9, 148.1, and 208.9 keV, listed in Ref. [6] as deexciting ^{144m}Ho, see Fig. 6.20. The spectrum given in Fig. 6.20 results from gating measured gamma energies by the first 1500 ns of recoil-decay correlation time and subtracting the events obtained in correlation with the second 1500 ns interval. In addition, we observed a 40.2 keV line with a sub-microsecond half-life correlated

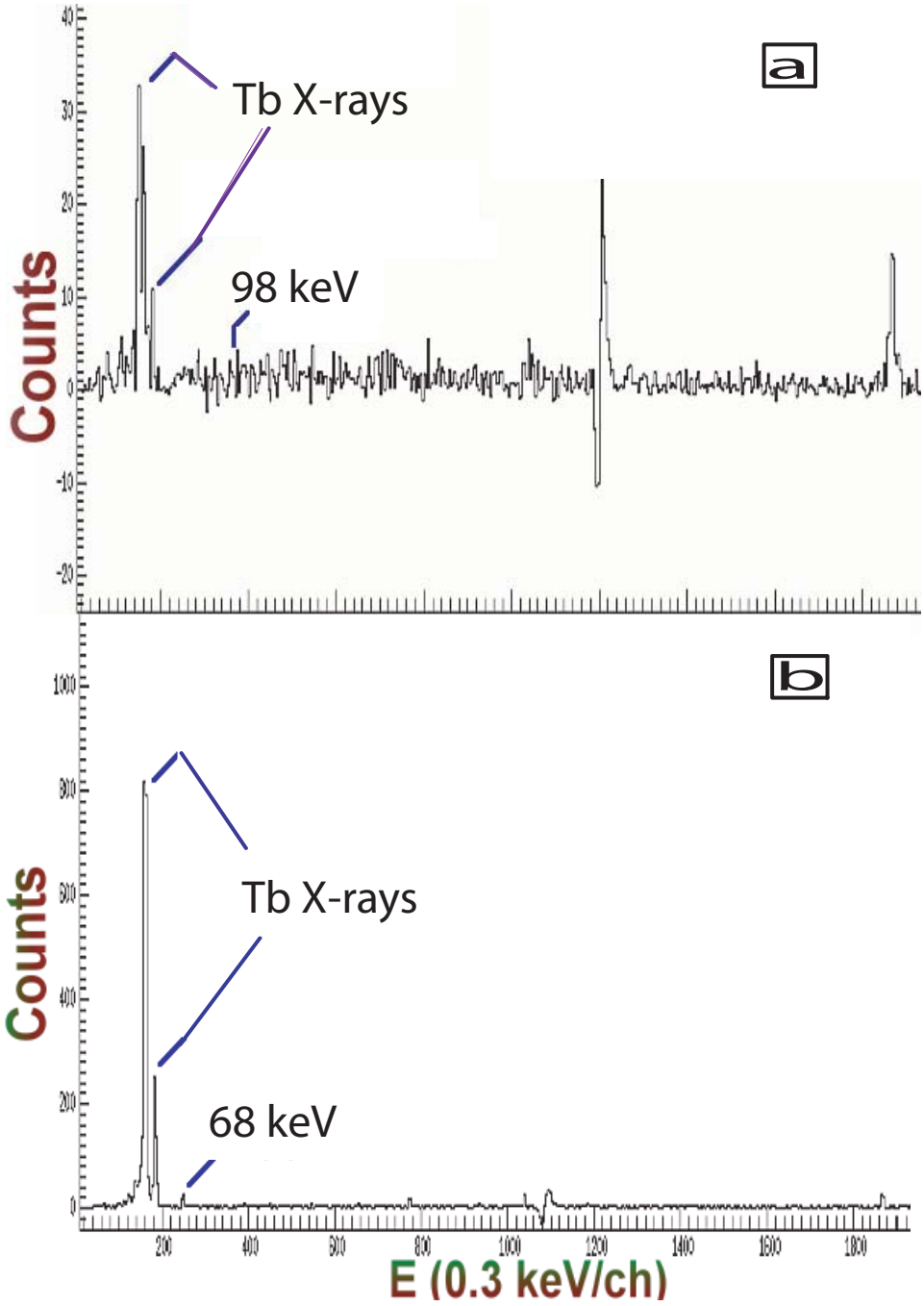

Figure 6.19: (a) $\gamma - \gamma$ coincidence spectrum gated on the 181.8 keV γ-ray in ^{142m1}Tb. (b) $\gamma - \gamma$ coincidence spectrum gated on the 211.5 keV γ-ray in ^{142m1}Tb.

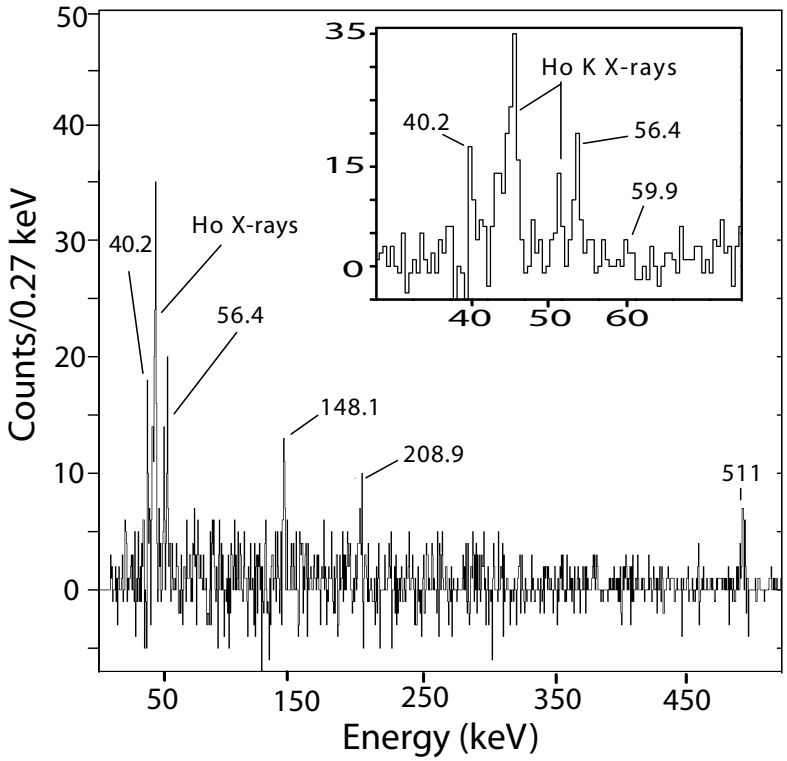

Figure 6.20: Gamma spectrum associated with the decay of ^{144m}Ho measured by the LOAX detector within 1500 ns after implantation of mass $A = 144$ recoils. The upper panel shows the X-ray and low-energy γ-ray part of the spectrum.

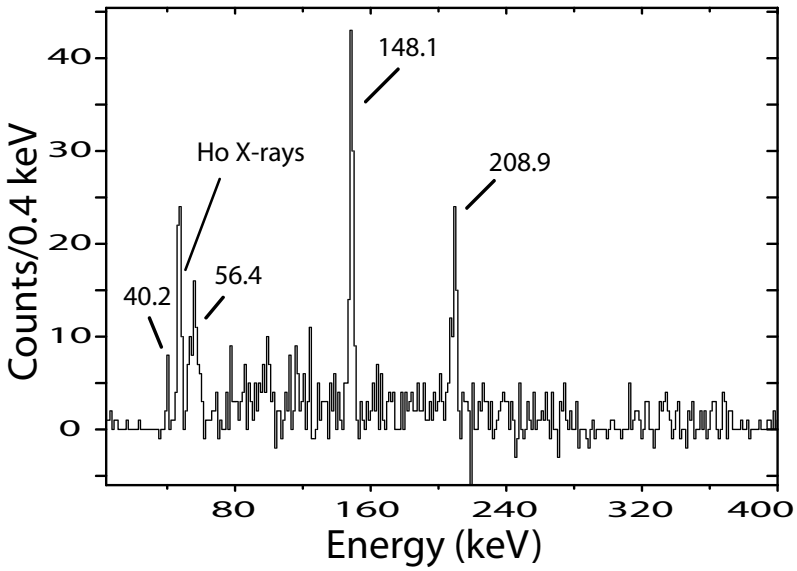

Figure 6.21: Gamma spectrum measured by the clover detectors within 1500 ns after implantation of mass $A = 144$ recoils.

with the implantation of the $A = 144$ recoils, see Table 6.6. The 40.2 keV line was observed in the spectrum measured by the low-energy LOAX detector, see Fig. 6.20, as well as in the spectrum recorded by the two clover detectors, compare Fig. 6.21. However, we were not able to place this transition in the ^{144}Ho level scheme due to low $\gamma-\gamma$ coincidence statistics. Application of shorter or longer recoil-γ correlation times did not reveal new activities.

We have measured the half-life of ^{144m}Ho to be 564(60) ns, see Fig. 6.22, in agreement with the 500(20) ns given in Ref. [6].

We follow the level sequence in ^{144}Ho as proposed in Ref. [6], see Fig. 6.23. By gating on the 59.9 keV line, we determined α_K(148.1 keV)= 0.69(15) by comparing the number of photons in the 148.1 keV γ-ray to that of the Ho K_α X-ray. This value of α_K for the 148.1 keV line is consistent with an M1+E2 multipolarity (see Table 6.6). We were unable to accurately measure an α_K value for the 59.9 transition due to a lack of sufficient γ-γ counting statistics. However, a rough estimate of α_K(59.9 keV)= 14(5) was obtained from gating on the 148.1 keV line. The calculated $\alpha_K = 1.0$, 2.3, 9.9, and 122 for an E1, E2, M1, and M2 multipolarities, respectively. With the large error bar, the measured α_K for the 59.9 keV line is consistent with a parity conserving M1+E2 transition character. By comparing the intensity of the 59.9 keV line to that of the 148.1 keV line we determined α_{total}(59.9 keV)= 12.6(46) which is also consistent with an M1+E2 multipolarity (see Table 6.6). The sequence of M1/E2 for the 59.9 and the 148.1 keV lines places a maximum spin and parity of $I^\pi = 7^-$ on the 208.9 keV level which allows a multipolarity of E2 for the 208.9 keV γ-transition with a calculated α_{total}(208.9 keV, E2)= 0.21. With the M1/E2 and E2 characters for the 148.1 and 208.9 keV transitions, the measured α_{total}(56.4 keV) has an upper limit of 1.26(43)

Table 6.6: ^{144m}Ho ($T_{1/2}$ = 564(60) ns) γ-ray transitions and intensities.

E_γ (keV)	Rel. I_γ (%)	Rel. I_γ (%) Ref. [6]	α_K, α_{total} (exp)	α_K, α_{total} (calc)	Adopted Multipolarity	I_{total} (units)
40.2(3)	91(17)					
56.4(3)	100(17)	100(9)	$\alpha_{total} < 1.3$	α_{total} = 0.3(E1), 26.2(E2), 2.3(M1)	E1	226(21)
59.9(9)	13(3)	11(1)	α_{total} = 12.6(46)	α_{total} = 1.2(E1), 21.9(E2), 11.8(M1)	M1/E2	176(76)
148.1(3)	99(18)	91(7)	α_K = 0.69(15)	α_K = 0.09(E1), 0.39(E2), 0.73(M1)	M1/E2	176(50)
208.9(3)	41(11)	54(6)		α_{total} = 0.05(E1), 0.21(E2), 0.34(M1)	E2	50(13)

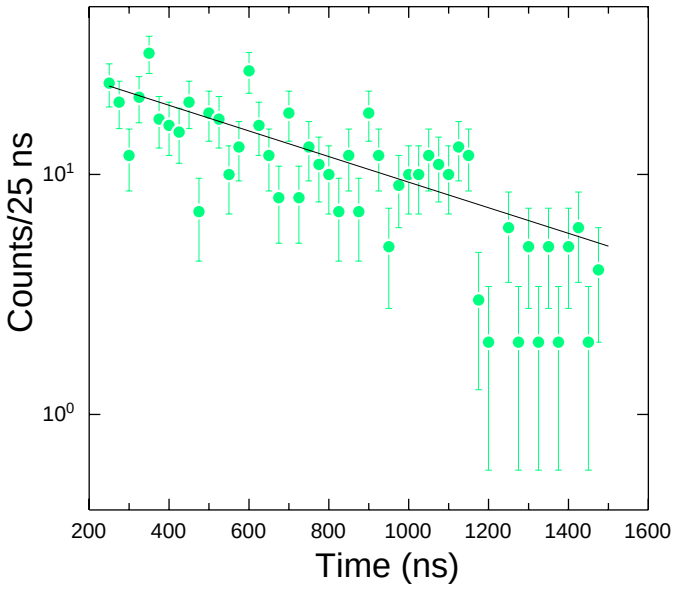

Figure 6.22: Decay pattern of the sum of the 56.4, 148.1, and 208.9 keV γ-rays in ^{144m}Ho. The fitted curve gives a half-life measurement of 564(60) ns.

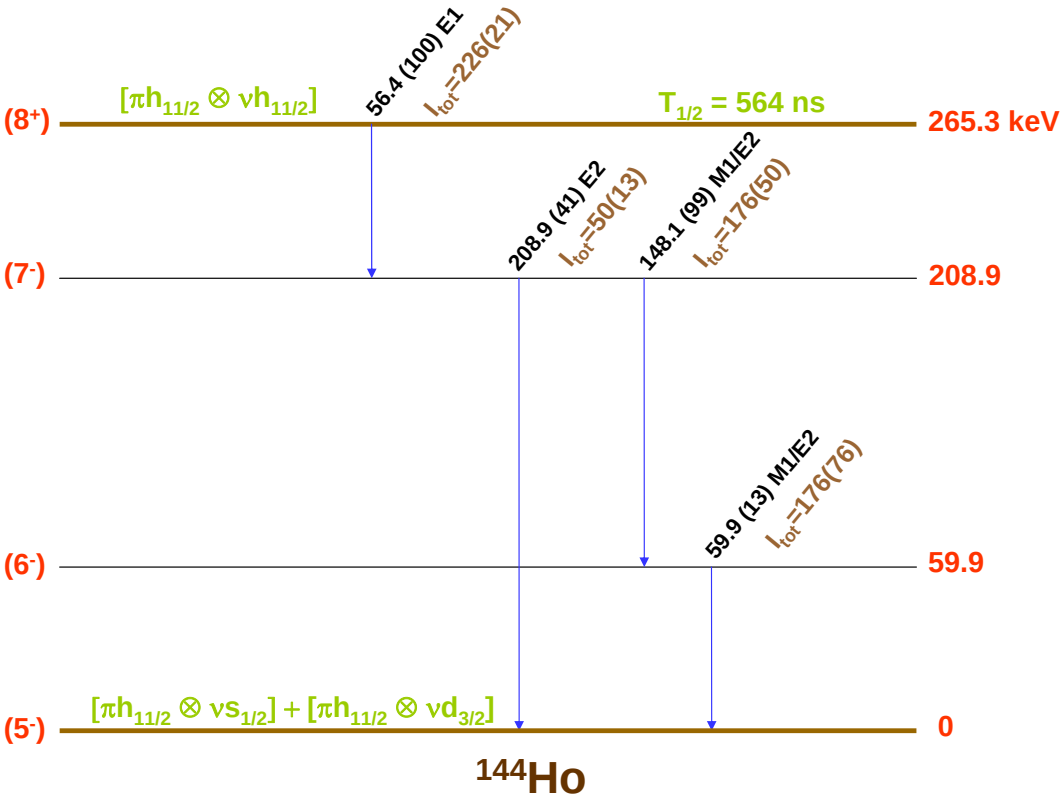

Figure 6.23: ^{144}Ho decay scheme.

which only allows for an E1 multipolarity (see Table 6.6). The E1 character of the 56.4 keV line was also postulated in Ref. [6].

In Ref. [6], the quoted γ-ray intensities for the 56.4, 59.9 and 148.1 keV lines are similar to our findings, see Table 6.6. However, the E1 multipolarities adopted in Ref. [6] for the 56.1, 59.9 and 148.1 keV lines do not produce a consistent total intensity balance. In particular, the total intensities within the 148.1 - 59.9 cascade differ by a factor of ~ 5 in Ref. [6]. The total intensity of the 56.4 keV transition cannot be reproduced by the sum of the 148.1 and 208.9 keV lines in Ref. [6]. Our measurements from the neighboring odd-Z $N = 77$ isotones, namely ^{140m2}Eu and ^{142m2}Tb, indicate that all observed levels below the 0.5 μs isomer have negative parity. This fits to the E2 character of the 208.9 keV line as postulated in Ref. [6]. The transition intensity balance is consistent now, see Table 6.6 and Fig. 6.23.

The high spin state $\pi h_{11/2} \otimes \nu h_{11/2}$ in ^{144}Ho is expected to be dominantly produced in the heavy ion fusion-evaporation reaction as suggested in Ref. [6]. Two transitions in ^{144m}Ho decay, the 56.4 keV E1 and 208.9 keV E2 change the spin by up to three units, and connect the high-spin state to the lowest observed state. The spin assignments of 8^+ for the high spin isomer and 5^- for the the medium spin state and also, 9^+ and 6^- assignments are consistent with the isomeric decay properties. We adopt the 8^+ and 5^- sequence, as in the lower mass $N = 77$ isotones, ^{140}Eu and ^{142}Tb. This suggests $I^\pi = 7^-$ and 6^- for the 208.9 keV and 59.9 keV levels, respectively (see Fig. 6.23). There was no experimental evidence obtained in our work or in Ref. [6] for a potential 1^+ ground-state. A 1^+ ground-state of ^{144}Ho can be expected from simple extrapolation of the level systematics of the neighboring lower-mass $N = 77$ isotones, ^{140}Eu and ^{142}Tb. The observations in Ref. [6] and in this work might indicate that the 1^+ $[\pi d_{5/2} \otimes \nu d_{3/2}]$ configuration identified from the Gamow-Teller beta decay studies for ^{140}Eu and ^{142}Tb does not minimize the energy of higher-Z $N = 77$ even-mass isotones at the proton drip line. The proton orbital $d_{5/2}$ is filled for $Z = 67$ ^{144}Ho and a moderate spin (5^-, 6^-) $\pi h_{11/2} \otimes \nu s_{1/2}$ level might be already the ground-state configuration.

The list of γ-ray transition and their relative intensities observed in our measurements for ^{144m}Ho decay is given in Table 6.6 and the level scheme is shown in Fig. 6.23.

The estimated Weisskopf half-life for the 56.4 keV line deexciting ^{144m}Ho with an E1 transition is 1.5 ps. A comparison with an experimental value of 0.5 μs yields a retardation factor of about 1×10^6.

6.4 Proton radioactive ^{146}Tm

Proton emission from the odd-odd $N = 77$ isotone ^{146}Tm was first reported in Ref. [62], with two proton transitions observed. The measured energies and half-lives were given as $E_p = 1.119(5)$ MeV and $T_{1/2} = 235(27)$ ms, and $E_p = 1.189(5)$ MeV and $T_{1/2} = 72(23)$ ms, respectively. Reinvestigation of the ^{146}Tm activity at the HRIBF [8] resulted in the identification of three additional proton transitions, at 1.01 MeV, $T_{1/2} = 110(50)$ ms, and at 0.94 MeV, $T_{1/2} = 80(30)$ ms, and at 0.89 MeV, $T_{1/2} = 190(50)$ ms. The decay

patterns of the 1.12 and 1.19 MeV lines yielded more accurate half-lives of 200(10) ms and 80(10) ms [8], respectively.

Based on the similarity of the measured half-lives, the transitions at 1.12 MeV and 0.89 MeV were assigned to the decay of the predominately $\pi h_{11/2} \otimes \nu h_{11/2}$ isomeric state ^{146m}Tm at 175 keV excitation energy, while the decay of the mostly $\pi h_{11/2} \otimes \nu s_{1/2}$ ground state of ^{146}Tm was postulated to deexcite by the 1.19 and 0.94 MeV transitions [8]. The spin and parities of $I^{\pi} = (8^{+})$ and $I^{\pi} = (5^{-})$ were proposed [8] for ^{146m}Tm and ^{146gs}Tm, respectively. The assignment of the 1.01 MeV line to either state was ambiguous. Even a possibility of a third proton emitting state, of $I^{\pi} = 1^{+}$, was considered, but this scenario was rejected because the lifetimes expected for the $l = 2$ or $l = 0$ proton transitions at 1.01 MeV are too short.

The wave function components for ^{146m}Tm and for ^{146gs}Tm were calculated in Ref. [8] by using a spherical approach, which was a simplification for this transitional nucleus. These ambiguities led us to the experimental and theoretical reinvestigation of proton emission from the states in ^{146}Tm.

In the present study, the acquired statistics of proton events exceeded the previous study [8] by a factor of about five. The mass spectrum recorded by the MCP at the focal plane of the RMS before closing the blockers (compare chapter 5), is shown in Fig. 6.24. It indicates that $A = 146$ and $A = 147$ recoils were transmitted with the RMS setting optimized for the $A/Q = 146/27$ and $A/Q = 146/28$ recoils. The two-slit three-blockers system was used to permit the $A = 146$ recoils in both charge states to be implanted in the DSSD while eliminating the other masses. The effect of the three blockers system is shown in Fig. 6.25. However, a small contamination of ^{147}Tm did appear in the DSSD proton spectra

Improved statistics in the proton spectrum (see Fig. 6.26) allowed us to determine the half-lives of all five proton transitions with smaller uncertainty in comparison to the earlier work [8], see Table 6.7. The half-life of each proton line was determined by fits to (1) the exponential decay of the time distribution of the events in the time interval 1-1200 ms, (2) the growth of the integrated counts with time as shown in Fig. 6.27, and (3) an independent analysis done by Dr. John Batchelder of the same data. The exponential growth data in Fig. 6.27 was fitted with the expression $C = C_o(1 - EXP(-\lambda_o t)) + C_b(1 - EXP(-\lambda_b t))$ where C_o and C_b are the number of counts of the proton peak and the background, respectively, at infinity. λ_o and λ_b are the decay constants of the proton peak and the background, respectively. All three procedures of measuring the proton half-lives gave similar results.

On the basis of the measured half-life of 66(5) ms for the 1.016 MeV transition (see Fig 6.27), we assign it to the 68 ms ground state decay of ^{146}Tm (see Fig. 6.28). The half-life of the 0.89 MeV proton decay was determined to be 200(40) ms as shown in Fig. 6.27. Thus the 0.89 MeV proton transition is assigned to the decay of the 198 ms ^{146m}Tm, as in Ref. [8].

From a simple shell-model picture, one expects that ^{146}Tm would have 5 protons above the $Z = 64$ proton sub-shell, and 5 neutron holes below the $N = 82$ closed shell. The available single particle orbitals for both protons and neutrons are therefore $h_{11/2}$, $s_{1/2}$, and $d_{3/2}$. These states, for both protons and neutrons, are known to be energetically very close, within a few hundred keV, forming a sub-shell between proton (neutron) numbers 65 and

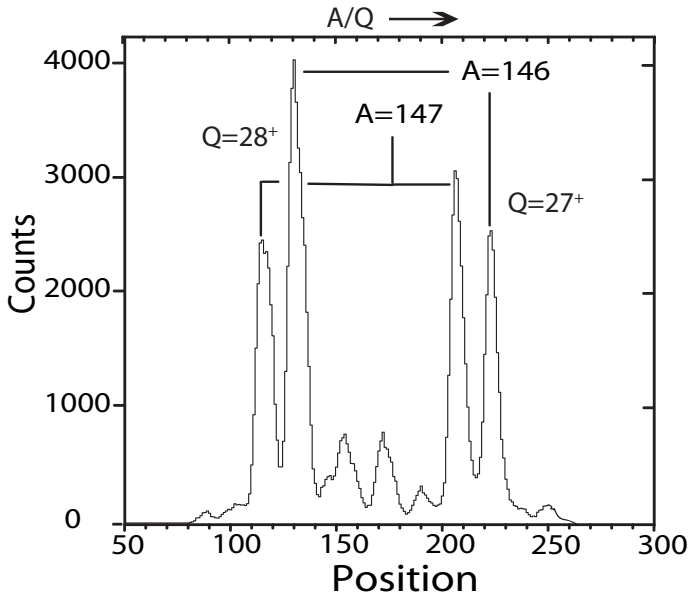

Figure 6.24: Mass spectrum for the ^{146}Tm experiment measured by the large MCP detector at the focal plane of the RMS as a function of the time of flight TOF. The RMS was optimized for $A/Q = 146/27$ and $A/Q = 146/28$ recoils.

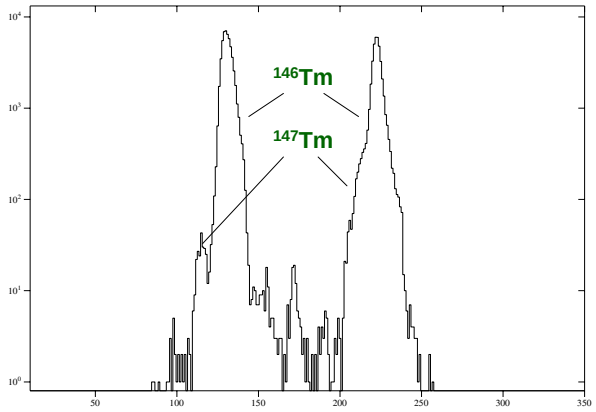

Figure 6.25: Mass spectrum for the ^{146}Tm experiment measured by the MCP detector at the focal plane of the RMS. The RMS was optimized for $A/Q = 146/27$ and $A/Q = 146/26$ recoils with the three slits now optimized to allow $A = 146$ ions to reach the DSSD with both charge states while stopping or reducing the implantation of other masses.

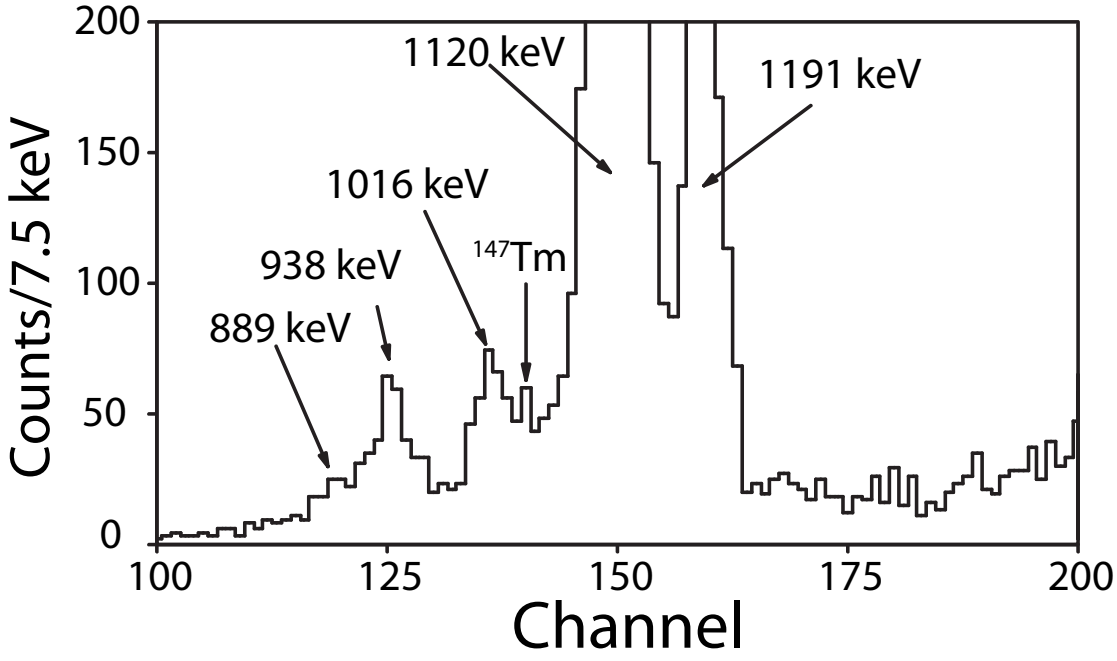

Figure 6.26: Energy spectrum of protons correlated with implanted ^{146}Tm ions. The correlation time window for this spectrum was 200 ms. The spectrum was also gated by anti-coincidence with the Si-box.

Table 6.7: Proton energy (E_p) values, relative intensities, and half-lives ($T_{1/2}$) for the transitions observed in ^{146}Tm. The first three are assigned to the $I^\pi = 5^-$ ground state, while the last two originate from the $I^\pi = 10^+$ isomeric level.

E_p (keV)	Area within 1200 ms after $A = 146$ implants	I (%)	$T_{1/2}$ (ms)
938(4)	266(16)	20.0(13)	66(4)
1016(4)	357(19)	26.8(16)	66(5)
1191(1)	1333(39)	100(3)	68(2)
889(8)	100(40)	1.0(4)	200(40)
1120(1)	10393(102)	100(1)	198(3)

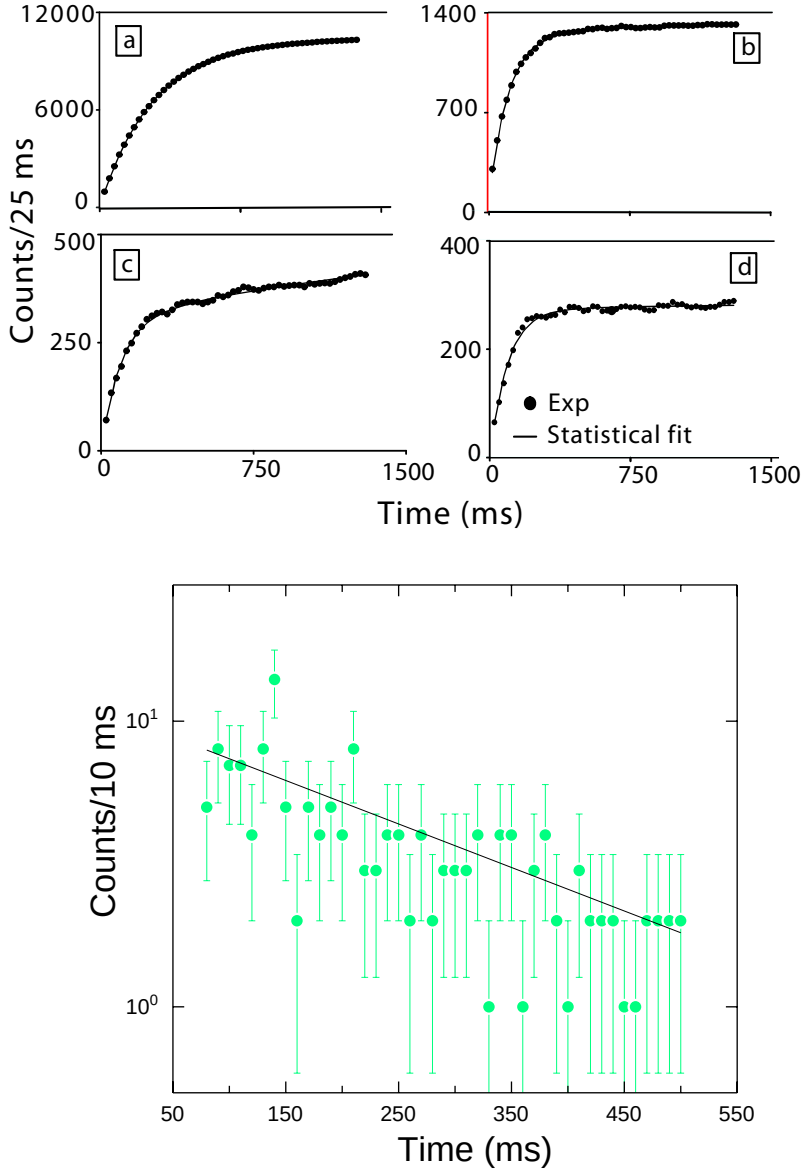

Figure 6.27: (Top) Determination of the proton half-lives in ^{146}Tm decay using the exponential rise to maximum least square fit function for the four proton energies: (a) 1.120 MeV, (b) 1.191 MeV, (c) 1.016 MeV, and (d) 0.938 MeV. The 1.016- and 0.938-MeV lines show bigger background components than the 1.120- and 1.191-MeV lines due to the close proximity of longer lived lines which are the 1.05 MeV line in ^{147}Tm and the 0.89 MeV line in ^{146m}Tm.
(Bottom) Decay pattern of the 0.889 MeV proton line deexciting ^{146m}Tm. The half-life of this line was determined to be 200(40) ms.

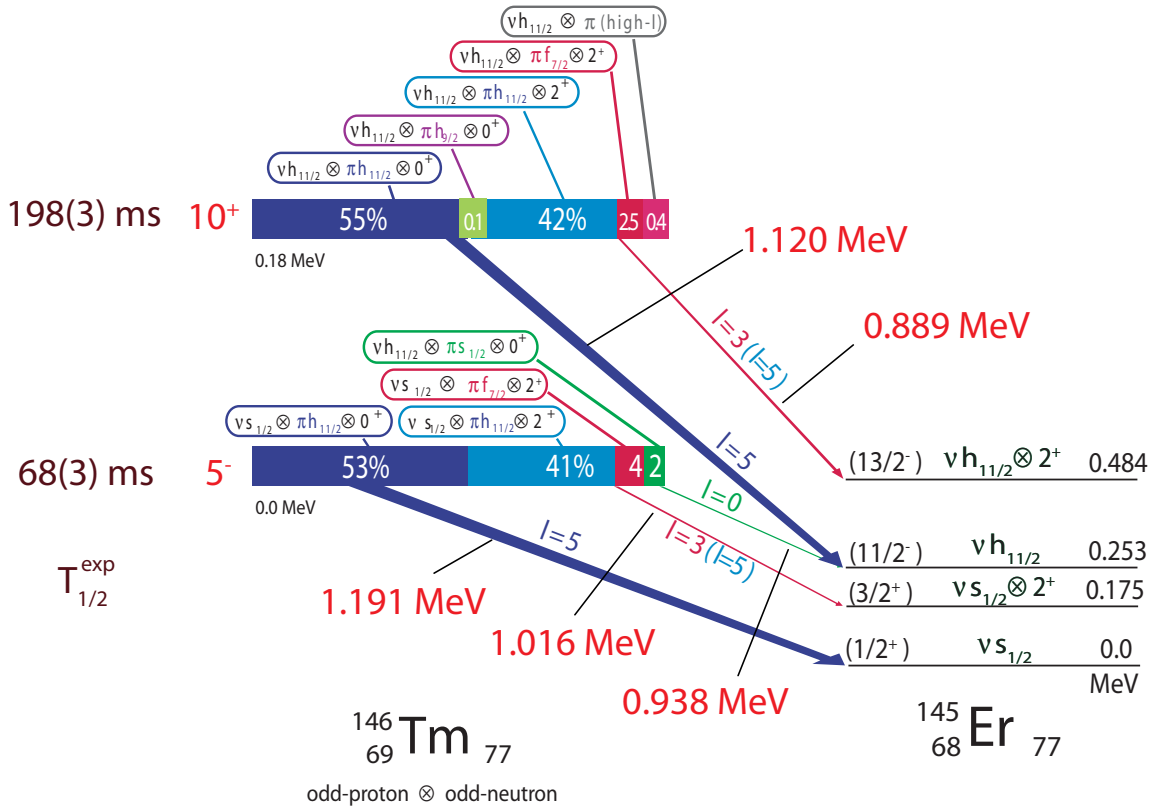

Figure 6.28: The decay scheme of ^{146}Tm established in the present work. The contribution of the wave functions given in percent were calculated using the particle-core vibration coupling model [14].

82. The $\nu s_{1/2}$ state minimizes the energy of the $N = 77$ even-Z isotones in this region (see Fig. 6.29). The $\nu d_{3/2}$ and $\nu h_{11/2}$ single particle states above the $\nu s_{1/2}$ ground-state are shown in Fig. 6.29 together with the low-energy $I^\pi = 3/2^+$ and $5/2^+$ states of a $\nu s_{1/2} \otimes 2^+$ origin.

The $\pi h_{11/2}$ orbital was observed as a ground state for the neighboring thulium isotopes, ^{145}Tm [24, 42] and ^{147}Tm [63]. The proton-emitting $\pi d_{3/2}$ states are known in ^{147}Tm and ^{151}Lu, at 60 keV [63] and 77 keV [15] above the $\pi h_{11/2}$ ground-state, respectively. The $\pi s_{1/2}$ states are known in heavier odd-mass Tm isotopes to be about 50 keV above the $\pi h_{11/2}$ orbital (see Fig. 6.30)

From the experimental level systematics of heavier odd-odd Tm isotopes and the odd-odd $N = 77$ isotones, see Fig. 1.1, one would expect an isomer with a spin and parity of 8^+ to 10^+, with a dominant configuration of $\pi h_{11/2} \otimes \nu h_{11/2}$, and a lower spin state, possibly the ground-state, of $I^\pi = 5^-$ or 6^- and main wave function component $\pi h_{11/2} \otimes \nu s_{1/2}$ in ^{146}Tm. Both states can have a complex structure with admixtures contributing to their wave functions. For example, for the lower spin state one can consider the mixing with the $\pi s_{1/2} \otimes \nu h_{11/2}$, $\pi d_{3/2} \otimes \nu h_{11/2}$, and $\pi h_{11/2} \otimes \nu d_{3/2}$ components, all coupled to the same spin of 5^- or 6^-. For both high spin and medium spin states, the $\pi h_{11/2}$ can be "substituted" by the $\pi f_{7/2}$ coupled to the 2^+ phonon representing the excited state of the ^{144}Er even-even core. Such a component in the wave function of ^{145}Tm explained the observed fine structure line in its decay [24]. The 4% admixture of the $\pi f_{7/2} \otimes 2^+$ to the dominating $\pi h_{11/2}$ is responsible for the $I_p = 10\%$ proton transition from ^{145}Tm ($I^\pi = 11/2^-$) to the 2^+ first excited state at 0.33 MeV in ^{144}Er [24]. The analysis of the ^{145}Tm wave function and proton emission process was made within a particle-core vibration coupling model [14,24]. It accounted for the deformation of the ^{144}Er core, with $\beta_2 = 0.18$ deduced from the 0.33 MeV energy of the first 2^+ state [64, 65]. This model was extended here to include coupling of the odd-neutron and is used here for the first time to interpret proton emission from an odd-odd nucleus, in our case ^{146}Tm.

High spin isomer ^{146m}Tm

We consider here the decay of the 198 ms level, populated much stronger in the fusion-evaporation reaction in comparison to the 68 ms activity. As in the earlier work [8], based on the similar half-life values of the 1.12 and 0.89 MeV proton transitions, see Table 6.7, we assume the same level of origin for these proton lines. New calculations also point to a large component of the wave function of ^{146m}Tm, the $\pi h_{11/2} \otimes 0^+ \otimes \nu h_{11/2}$, as responsible for the dominating $l = 5$, 1.12 MeV transition to the $\nu h_{11/2}$ band-head in ^{145}Er, and to a smaller component, the $\pi f_{7/2} \otimes 2^+ \otimes \nu h_{11/2}$, as the origin of a weak $l = 3$, 0.89 MeV transition to an excited level built on the $\nu h_{11/2}$ band-head. However, there is one major difference between our interpretation and that of Ref. [8]. As shown below, it is now clear that the isomer spin has to be at least 10^+, as in heavier odd-odd Tm isotopes rather than the (8^+) assignment as was suggested in Ref. [8]. It was overlooked in Ref. [8] that the coupling to the $I^\pi = 8^+$ state allows for the presence of the $\pi f_{7/2} \otimes 0^+ \otimes \nu h_{11/2}$ component in the ^{146m}Tm wave function which would trigger an $l = 3$, 1.12 MeV proton transition

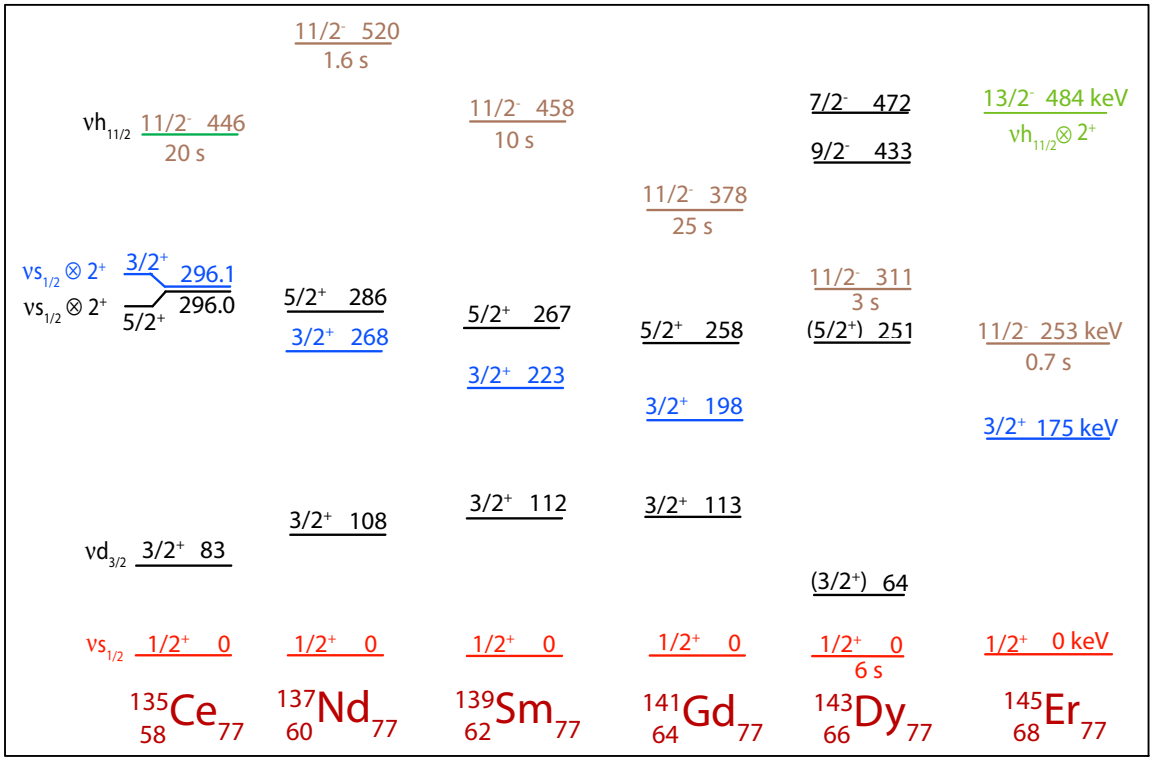

Figure 6.29: Synopsis of the experimentally determined level systematics for the lightest $N = 77$ even-Z isotones. This figure is an extension of Fig. 1 from Ref. [8]. The level energies are labeled in keV. The half-lives of the $\nu h_{11/2}$ isomeric states are also given.

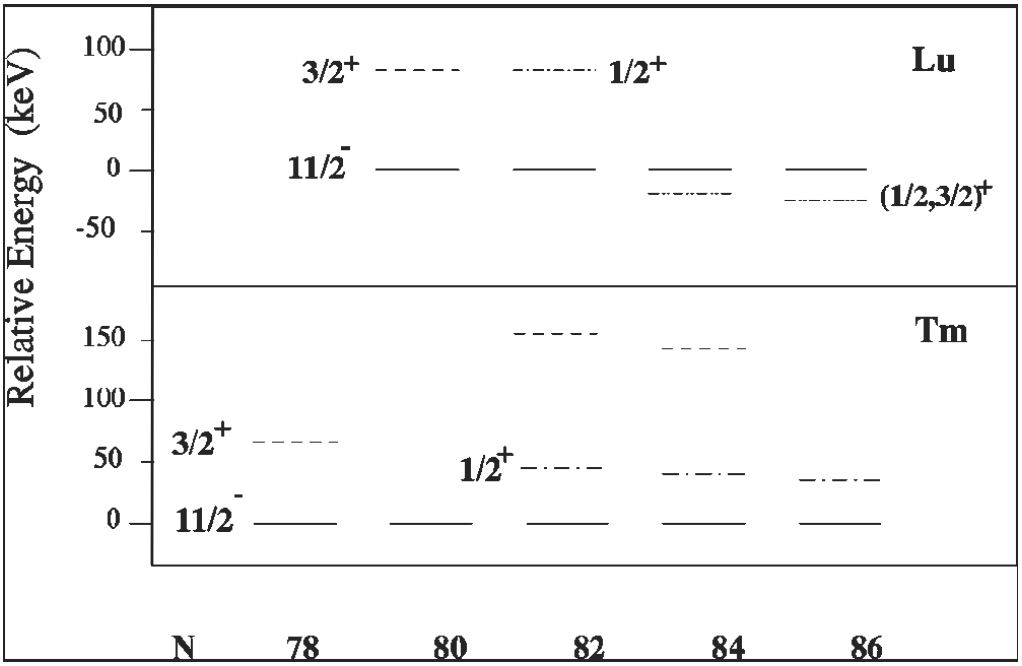

Figure 6.30: Systematics of low-lying levels in the heavy Lu and Tm isotopes as a function of neutron number. Figure taken from Ref. [15]

to the $\nu h_{11/2}$ band-head, resulting in an approximately 50 ms partial half-life. Indeed, the particle-core vibration coupling model predicts a 1.7% contribution of such a configuration, if coupling to the $I^\pi = 8^+$ or even $I^\pi = 9^+$ state occurs. The branching ratio for the $l = 3$, 0.89 MeV line would then be much smaller, at the 0.01% level. However, the coupling to the $I^\pi = 10^+$ (or to the $I^\pi = 11^+$) state excludes the $\pi f_{7/2} \otimes 0^+ \otimes \nu h_{11/2}$ component from the ^{146m}Tm wave function. The data on the half-life and fine structure branching ratio of ^{146m}Tm do not really distinguish between the $I^\pi = 10^+$ or $I^\pi = 11^+$ state, compare Table 2 in Ref. [17], and see Table 6.7. However, since the $I^\pi = 10^+$ isomeric state was identified in ^{150}Tm [66] and suggested for neighboring ^{148}Tm [11], we follow such a spin assignment for ^{146m}Tm. It means that the 0.89 MeV $l = 3$ proton line should populate a negative parity state, with a $\nu h_{11/2} \otimes 2^+$ configuration in ^{145}Er, with a spin equal to or higher than 13/2. A recent in-beam study of the neighboring $N = 77$ isotone ^{143}Dy [67] shows a possible candidate for such a state at 122 keV above the $\nu h_{11/2}$ band-head in a negative parity band but with an unassigned spin value. The known 2^+ energy in ^{144}Er is 329(1) keV [24, 68]. Therefore, the energy difference of 230 keV between the $I^\pi = 11/2^-[\nu h_{11/2} \otimes 0^+]$ band-head and the $I^\pi = 13/2^-[\nu h_{11/2} \otimes 2^+]$ state in ^{145}Er is reasonable. The calculated configuration and the proton emission probabilities of the 10^+ isomer in ^{146}Tm are given in Table 6.8.

Within the spherical approach discussed in Ref. [8], the wave function of the isomeric state was expected to be dominated by a 91% $\pi h_{11/2} \otimes \nu h_{11/2}$ configuration. The particle-core vibration coupling calculations show that 97% of the wave function contains the $\pi h_{11/2} \otimes \nu h_{11/2}$ component. However, this configuration is split into roughly equal parts by the coupling to the 0^+ and 2^+ states of the core, see Table 6.8. This means that only about 55% of the wave function contributes to the $l = 5$ proton transition to the $\nu h_{11/2}$ band-head in ^{145}Er. The remaining 42% of the $\pi h_{11/2} \otimes 2^+ \otimes \nu h_{11/2}$ component would add some negligible intensity to the $l = 3$ proton transition populating the $\nu h_{11/2} \otimes 2^+$ excited state.

Medium spin ^{146gs}Tm

The short-lived 68 ms ^{146}Tm activity was assigned earlier [8] to the level resulting from the coupling of the $\pi h_{11/2}$ to the $\nu s_{1/2}$ nucleons. Since both orbitals are known to minimize the energy in the neighboring odd-mass nuclei, it is reasonable to expect that this proton-neutron state is the ground-state of ^{146}Tm. The proton lines at 1.19 and 0.94 MeV were assigned to the decay of ^{146gs}Tm in Ref. [8]. Based on the similarity of the observed half-lives, we can now assign three observed proton transitions, at 1.19, 1.016 and 0.94 MeV, to the decay of the ground-state. It was recognized earlier [62], that the intense 1.19 MeV proton transition has $l = 5$ character, i.e., the proton originates from the $\pi h_{11/2}$ orbital. In Ref. [8] this proton line was interpreted for the first time as the ground-state to ground-state transition populating the $\nu s_{1/2}$ orbital in ^{145}Er. The particle-core vibration coupling model calculations indicate that the 1.016 MeV line originates from the 4% $\pi f_{7/2} \otimes 2^+ \otimes \nu s_{1/2}$ component of the wave function. The agreement between the observed and calculated decay probability is very good, see Table 6.8. The $l = 3$, 1.016 MeV line populates the excited state at 175 keV in ^{145}Er associated with the $\nu s_{1/2} \otimes 2^+$ structure. A spin and parity of

Table 6.8: Proton energy (E_p) values, branching ratios and wave functions for the transitions observed in ^{146}Tm along with their wave functions. The first three are assigned to the $I^\pi = 5^-$, $T_{1/2} = 68(5)$ ms ground state, while the last two originate from the $I^\pi = 10^+$, $T_{1/2} = 198(3)$ ms isomer level.

E_p (keV)	Rel. exp. proton branching ratio (%)	Wave function[a]	Contribution to the total width (%)	$\Delta\ell$	^{145}Er level energy (keV)
938	13.8(9)	2% $[\pi s_{1/2} \otimes 0^+] \otimes \nu h_{11/2}$	(15) [b]	0	253 $(11/2^-)$
1016	18.3(11)	4% $[\pi f_{7/2} \otimes 2^+] \otimes \nu s_{1/2}$	15	3	
		41% $[\pi h_{11/2} \otimes 2^+] \otimes \nu s_{1/2}$	0.003	5	175 $(3/2^+)$
1191	68.1(19)	53% $[\pi h_{11/2} \otimes 0^+] \otimes \nu s_{1/2}$	70	5	0 $(1/2^+)$
889	1.0(4)	2.5% $[\pi f_{7/2} \otimes 2^+] \otimes \nu h_{11/2}$	1.2	3	
		0.4% π $(\ell > 5)$ $\otimes \nu h_{11/2}$			
		42% $[\pi h_{11/2} \otimes 2^+] \otimes \nu h_{11/2}$	0.04	5	484 $(13/2^-)$
1120	99(1)	55% $[\pi h_{11/2} \otimes 0^+] \otimes \nu h_{11/2}$	98.6	5	253 $(11/2^-)$
		0.1% $[\pi h_{9/2} \otimes 0^+] \otimes \nu h_{11/2}$	0.2	5	

[a] Based on the particle-core vibration coupling model [14]

[b] This value was inferred from experimental data but was not predicted by the particle-core vibration coupling model.

$3/2^+$ or $5/2^+$ are possible options. The low energy of 182 keV suggests the $3/2^+$ assignment based on the systematics shown in Fig. 6.29. If this is adopted, it means that the initial spin and parity of ^{146gs}Tm is $I^\pi = 5^-$ (the lowest spin populated by the $l = 3$ proton originating from $I^\pi = 6^-$ is $5/2^+$).

The 0.94 MeV line was identified in the previous work [8] as having $l = 0$ character resulting from a 4% "isospin-mirror" component in the ground-state wave function, the $\pi s_{1/2} \otimes 0^+ \otimes \nu h_{11/2}$. The calculated structure of the wave function, which now includes the $\pi f_{7/2} \otimes 2^+ \otimes \nu s_{1/2}$ part, requires about 2% of the isospin-mirror admixture to explain the relative intensities of the proton lines at 1.19, 1.016 and 0.94 MeV.

We have inspected theoretically the possibility of an $l = 3$ character for the 0.94 MeV transition feeding the $5/2^+$ level of $\nu s_{1/2} \otimes 2^+$ configuration (instead of $l = 0$ feeding the $\nu h_{11/2}$ band head). The calculated intensity ratio of the 1.016 MeV and 0.94 MeV transitions was 96:1, as one would expect for two proton transitions carrying the same orbital angular momentum l and having 78 keV energy difference. The observed intensities for the 1.016 and 0.94 MeV lines are similar to each other (see Table 6.7) which rules out this scenario.

The wave function composition and decay width for both possible spin couplings, 5^- and 6^-, are listed in Table 6.8.

Alternative decay pattern for ^{146}Tm

The assignment of the observed proton lines to only two decaying states in ^{146}Tm was made based on the similarity of the observed half-lives. Since the half-life uncertainties are relatively large for the weakest line at 0.89 MeV, one can at least consider the possibility for a third proton decaying state, below the discussed $I^\pi = 5^-$ state, with a half-life around 200 ms, but different from 198(3) ms. This possibility was suggested recently in Ref. [69, 70] and supported by the recoil decay tagging measurements, where the γ-ray transitions correlated with the 1.12 MeV proton transition did not appear to be correlated with the weak 0.89 MeV transition.

The 1^+ ground state known in the odd-odd $N = 77$ isotones ^{140}Eu and ^{142}Tb was not observed for heavier ^{144}Ho (see Section 6.3). These known 1^+ states were identified as the Gamow-Teller pairs [1] with $\pi d_{5/2} \otimes \nu d_{3/2}$ configurations. For heavier nuclei like ^{144}Ho and ^{146}Tm this state likely appears above the ground-state since the $\pi h_{11/2}$ and $\nu s_{1/2}$ orbitals are closer to the Fermi surface than the respective d-orbitals.

The $\pi d_{3/2} \otimes \nu s_{1/2}$ excited state in ^{146}Tm would decay via an $l = 2$ transition to the $\nu s_{1/2}$ ground-state. Assuming a pure $\pi d_{3/2} \otimes \nu s_{1/2}$ configuration, and accounting for the spectroscopic factor of the $d_{3/2}$ protons, one gets $\approx$ 400 ms for the partial half-life of the 0.89 MeV proton decay. The beta decay contributing to the decay width of this state can reduce the half-life to the 200 ms level and make such a scenario feasible. However, as it was pointed out above, the $\pi d_{3/2} \otimes \nu s_{1/2}$ configuration is unlikely to minimize the total energy of ^{146}Tm, so the proton transition from the $\pi d_{3/2} \otimes \nu s_{1/2}$ state to the $\nu s_{1/2}$ ground-state of ^{146}Tm should have an energy greater than 1.19 MeV.

The ground-state of ^{146}Tm is expected to be the point of change from prolate to oblate deformation as was the case for the neighboring $N = 77$ odd-Z nuclei [59]. It is not obvious

that such an effect can reduce the energy of the $\pi d_{3/2} \otimes \nu s_{1/2}$ configuration by 400 keV with respect to the $\pi h_{11/2} \otimes \nu s_{1/2}$ state, and create the $\pi d_{3/2} \otimes \nu s_{1/2}$ ground-state. However, it is an interesting problem worth further investigation. An in-beam study of the structure of ^{145}Er would be helpful to independently verify the properties of excited states populated by proton transitions. Also, to confirm the decay scheme of ^{146gs,m}Tm given in Fig. 6.28, it would be important to observe the gamma transitions in prompt coincidence with the 0.89 MeV and 1.016 MeV proton lines.

The decay of a 1045 keV proton from ^{146gs}Tm?

A proton with an energy of 1045-keV and a half-life of $\approx$ 70 ms in ^{146}Tm would decay from the 68 ms ground state to a 145 keV, $\nu d_{3/2}$ $3/2^+$ single-particle state in ^{145}Er completing the level systematics for $N = 77$ even-Z isotones shown in Fig. 6.29. Using the particle-core vibration coupling model, it is predicted that this 1045 keV proton would have a partial wave function of $\pi h_{11/2} \otimes \nu d_{3/2}$ and a $\Delta l = 5$. The contribution of the $\pi h_{11/2} \otimes \nu s_{1/2} \otimes 2^+$ wave function would have to be reduced to less than 41%. With two $\Delta l = 5$ transitions from ^{146m}Tm having the same fraction of the wave function of the 1191 and 1045 keV lines, their intensity ratio would be 59:1. This means that the number of counts that a 1045-keV proton peak emitted from the $I^\pi = 5^-$ ^{146gs}Tm would be $\approx$ 20 counts. Since the branching ratio of the wave function of the 1.19 MeV proton transition is 53%, and that of the 1.016 MeV is 4% while the branching ratio of the wave function of the 0.94 MeV transition is 2%, that would mean that the number of counts for a 1045-keV proton peak, if it existed in our data, would be even less than 15 counts. Since the proton decay rate is very sensitive to angular momentum coupling to the final state, it is likely that the intensity would be higher but not by a factor of 10 which is needed in order to see the proton peak above the background and instrumental threshold. The strong presence of ^{147}Tm in our data, as shown in Fig. 6.24 and Fig. 6.26, has a proton energy of 1055(10) keV. Thus, a weak 1045 keV line, if it existed, would lie in the background of ^{147}Tm. We attempted to make a very sharp cut on the mass to include only those protons decaying from mass 146 without any trace of mass 147. This was done by gating one only one charge state, $Q = +28$ and taking a few channels in that charge state that might not contain ^{147}Tm. With this cut, the statistics were reduced by more than half of what they were before the cut as shown in Fig. 6.31. From these figures, no conclusive evidence of the existence of a 1045 keV proton in ^{146}Tm exists. If the 1045 keV proton does exist, it would have very low statistics and a much longer run time with a more efficient DSSD detector is needed.

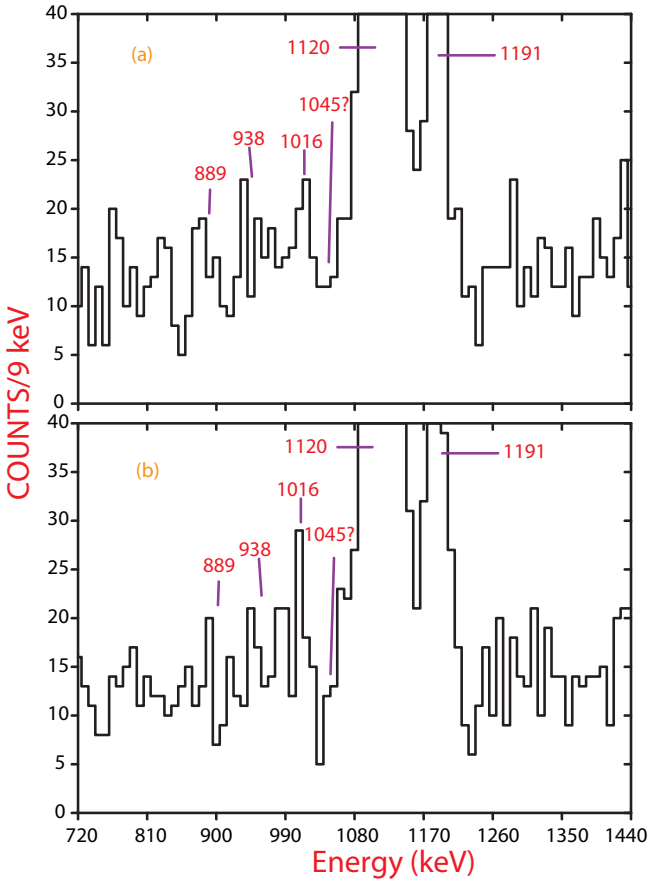

Figure 6.31: ^{146}Tm proton spectrum measured by (a) the front face and (b) the back face (of the DSSD after making a sharp cut on mass 146 and taking only one charge state, $Q = 28$, to prevent any contamination from mass 147. There is no evidence of a 1045 keV proton line emitted from ^{146gs}Tm or ^{146m}Tm.

Chapter 7

Summary and Conclusion

The systematics of the properties of the metastable $\pi - \nu$ states in proton-rich odd-odd $N = 77$ isotones were established by using decay spectroscopy methods. A 302 ns level in ^{140}Eu was found to be an $I^{\pi} = 8^{+}$ isomer arising from the coupling of the $h_{11/2}$ proton to the $h_{11/2}$ neutron. Its decay path terminates in the known $\pi h_{11/2} \otimes \nu s_{1/2}$ ^{140m1}Eu state. This sequence of metastable levels, with the ^{140m2}Eu state feeding the ^{140m1}Eu one, was determined experimentally. Most spin and parity values for the levels populated in the ^{140m2}Eu decay were firmly established, and we conclude that the isomer decays through retarded E1 transitions.

A half-life of 25(1) μs was measured for the decay of the high-spin isomer in ^{142}Tb replacing the earlier reported value of 15(4) μs [5]. New transitions were found to deexcite ^{142m2}Tb in this work and the level scheme of ^{142m2}Tb given in Ref. [6] was extended to account for these new transitions. Spins and parities of 5^{-} and 8^{+} for the isomeric levels in ^{142}Tb were unambiguously deduced from measured transition multipolarities. These states should have large components of the $\pi h_{11/2} \otimes \nu h_{11/2}$ and $\pi h_{11/2} \otimes \nu s_{1/2}$ configurations in their wave function, respectively. However, a respective "isospin mirror" admixture, namely the $\nu h_{11/2} \otimes \pi s_{1/2}$ configuration, may also be present in the wave function of the medium spin isomer, as indicated in Ref. [1].

The decay scheme of the 0.5 μs ^{144m}Ho state was verified and found to be in agreement with the level pattern given in Ref. [6]. The 59.9, 148.1, and 208.9 keV γ-ray transitions in ^{144m}Ho were found to have parity conserving M1+E2, M1+E2, and E2 character, respectively, opposite to the E1 multipolarity reported in Ref. [6].

The observed half-lives of ^{140m2}Eu, ^{142m2}Tb, and ^{144m}Ho indicate a strong hindrance of the E1 strength by a factor ranging from 10^5 to 10^7 with respect to the Weisskopf estimates. This hindrance could be related to shape difference or to residual effects of the $Z = 64$ shell. Similar behavior was observed by Gilat's group in their study of the odd-A nuclei near the $N = 77$ region [54]. One should note that direct γ-decay between the negative parity $\nu h_{11/2}$ orbital and the states related to the positive parity $\nu d_{3/2}$ and $\nu s_{1/2}$ orbitals does not occur in odd-mass $N = 77$ isotones near the proton drip line, see Fig. 7.1. These $\nu h_{11/2}$ states are known to decay via β-transitions. The coupling of odd neutron particles to the

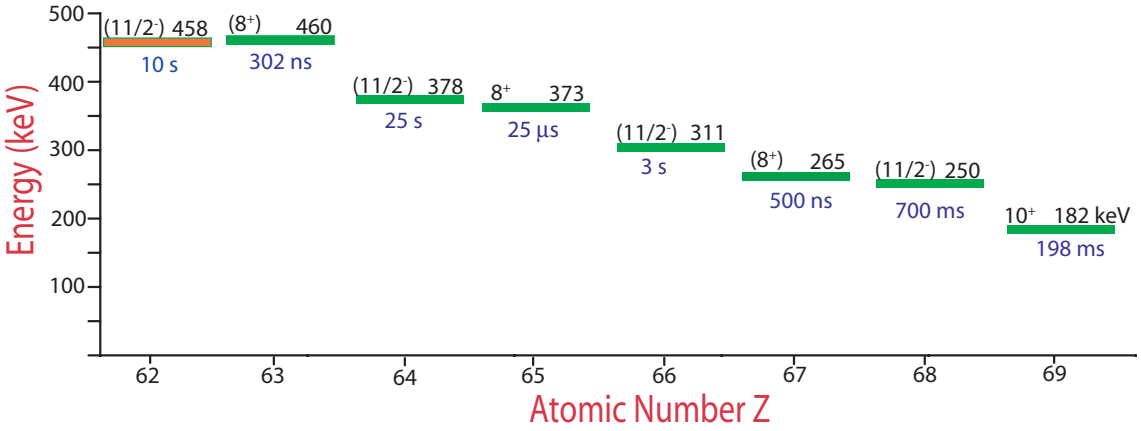

Figure 7.1: Comparison of the energy differences between the $\pi h_{11/2} \otimes \nu s_{1/2}$ and the $\pi h_{11/2} \otimes \nu h_{11/2}$ configurations with the energy difference of the $\nu s_{1/2}$ versus $\nu h_{11/2}$ configurations in the $N = 77$ isotones. The even-Z, $N = 77$ isotones decay via β emission only. On the other hand, the odd-Z, $N = 77$ isotones decay via γ-ray and particle emission.

$h_{11/2}$ proton facilitates the presence of strongly retarded E1 γ-ray transitions connecting the positive parity and negative parity states, see Figs. 6.3, 6.13, and 6.23.

The 1.016 MeV proton line, observed earlier [8] but not placed in the decay scheme of ^{146}Tm, was assigned to the decay of the shorter-lived ^{146gs}Tm with a half-life of 68(3) ms. This state is interpreted, within the particle-core vibration coupling model allowing for proton, neutron, and core coupling and accounting for the moderate deformation ($\beta_2 = 0.18$), as dominated by the $\pi h_{11/2} \otimes \nu s_{1/2}$ configuration coupled to the 0^+ and 2^+ states of the ^{144}Er core. The properties of proton emission do not distinguish between two possible spin couplings, to the $I^\pi = 5^-$ or 6^-. However, the state at 182 keV in ^{145}Er populated by the $l = 3$ proton transition from ^{146gs}Tm is more likely to be $3/2^+$ according to the level systematics, which supports the $I^\pi = 5^-$ assignment. The relative intensities of proton lines originating from the short-lived state are well reproduced within the particle-core vibration coupling model calculations. The calculated partial proton half-life of ^{146gs}Tm is about 79 ms, close to the measured value. This indicates that the decay width of this state is dominated by proton emission, with only about 14% contribution from β-decay. The resulting partial half-life $T^{\beta}_{1/2}$ of 490 ms is on the order of 220 ms predicted for the β-decay of ^{146}Tm [71].

The ^{146m}Tm, $T_{1/2} = 198(3)$ ms, was found to have spin and parity of $I^\pi = 10^+$, while the $I^\pi = (8)^+$ proposed earlier [8] is excluded by comparison to the particle-core vibration coupling model calculations. The wave function of ^{146m}Tm is dominated by the $\pi h_{11/2} \otimes \nu h_{11/2}$ component coupled to the 0^+ and 2^+ core states. A small 2.5% admixture of the $\pi f_{7/2} \otimes 2^+ \otimes \nu h_{11/2}$ configuration results in a branching ratio of 1.2% for the 0.89 MeV proton transition. This is close to the experimental value of $\approx 1\%$. The calculated partial

proton half-life of the ^{146m}Tm is about 750 ms. As recognized earlier [8], the Gamow-Teller beta decay, i.e., an allowed transformation of the $\pi h_{11/2}$ proton into a $\nu h_{9/2}$ neutron, governs the decay probability of ^{146m}Tm.

The observed sequence of levels in ^{144}Ho seems to resemble the basic properties of ^{146}Tm, with an apparent absence of the 1^+ ground-state known for lower-mass $N = 77$ isotones. Also, a simple analysis of the energies of the single particle orbitals near the Fermi surface in the ^{146}Tm region rather points to the existence of an excited 1^+ state. The 1^+ ground-state of ^{140}Eu and ^{142}Tb recognized earlier as the "Gamow-Teller pair" 1^+ $[\pi d_{5/2}^{-1} \otimes \nu d_{3/2}^{1}]$ configuration [1] is likely to appear as an excited state in heavier $N = 77$ isotones, since the $\pi h_{11/2}$ and $\nu s_{1/2}$ states are closer to the Fermi surface.

The evolution of the energy difference between the $\pi h_{11/2} \otimes \nu s_{1/2}$ and $\pi h_{11/2} \otimes \nu h_{11/2}$ configurations is given in Fig. 7.1 and shown to compare well with the $\nu h_{11/2}$ versus $\nu s_{1/2}$ energies in neighboring nuclei.

The decay of ^{146}Tm is an example of proton radioactivity study which contributes to the knowledge of neutron states in very exotic nuclei.

Bibliography

Bibliography

[1] R. B. Firestone *et al.*, Phys. Rev. C **43**, 1066 (1991).

[2] K. P. Rykaczewski, Eur. Phys. Journal **A15**, 81 (2002).

[3] D. M. Cullen *et al.*, Phys. Rev. **C66**, 034308 (2002).

[4] A. Hecht *et al.*, Phys. Rev. **C68**, 054310 (2003).

[5] I. Zychor *et al.*, GSI report **No.89-1**, (1989).

[6] C. Scholey *et al.*, Phys. Rev. C **63**, 034321 (2001).

[7] J. Gilat *et al.*, Proc. 5th Int. Conf. on Nuclei Far from Stability, Rosseau Lake, Canada 1987, ED., I. S. Towner 463 (1988).

[8] T. N. Ginter *et al.*, Phys. Rev. C **68**, 034330 (2003).

[9] E. Nolte *et al.*, Z. Phys. **A306**, 223 (1982).

[10] A. Gadea *et al.*, Z. Phys. **A355**, 253 (1996).

[11] J. M. Nitschke *et al.*, Phys. Rev. **C37**, 2694 (1988).

[12] K. S. Toth *et al.*, Phys. Rev. **C35**, 620 (1987).

[13] W. Królas *et al.*, Phys. Rev. C **65**, 031303R (2002).

[14] K. Hagino *et al.*, Phys. Rev. **C64**, 041304R (2001).

[15] C. R. Bingham *et al.*, Phys. Rev. **C59**, 2984R (1999).

[16] K. P. Rykaczewski *et al.*, American Institute of Physics **764**, 223 (2005).

[17] J. C. Batchelder *et al.*, Eur. Phys. J. **A25**, s01, 149 (2005).

[18] K. S. Krane, Introductory Nuclear Physics (1988).

[19] S. J. Skorka *et al.*, Nucl. Data **2**, 347 (1966).

[20] K. P. Jackson *et al.*, Phys. Lett. **33B**, 281 (1970).

[21] S. Hofman, Radiochim. Acta **70/71**, 93 (1995).

[22] C. N. Davids *et al.*, Ann. Rev. Nucl. Part. Sci. **47**, 541 (1997).

[23] K. P. Rykaczewki *et al.*, Eur. Phys. Journal **A15**, 81 (2002).

[24] M. Karny *et al.*, Phys. Rev. Lett. **90**, 012502 (2003).

[25] S. Aberg *et al.*, Phys. Rev. **C56**, 1762 (1997).

[26] S. Aberg *et al.*, Phys. Rev. **C58**, 3011 (1998).

[27] B. Barmore *et al.*, Phys. Rev. **C62**, 054315 (2000).

[28] A. T. Kruppa *et al.*, Phys. Rev. Lett. **84**, 4549 (2000).

[29] A. A. Sonzogni *et al.*, Phys. Rev. Lett. **83**, 1116 (1999).

[30] http://www.phy.ornl.gov/hribf .

[31] C. J. Gross *et al.*, Nucl. Inst. and Meth. **A450**, 12 (2000).

[32] J. E. Spencer and H. A. Enge, Nucl. Inst. and Meth. **49**, 181 (1967).

[33] M. Paul *et al.*, Nucl. Inst. and Meth. **A277**, 418 (1989).

[34] J. F. Liang *et al.*, Nucl. Inst. and Meth. **A435**, 393 (1999).

[35] J. L. C. Ford *et al.*, Nucl. Phys. **A226**, 189 (1974).

[36] D. Shapira *et al.*, Nucl. Inst. and Meth. **A454**, 409 (2000).

[37] W. R. Leo, Techniques For Nuclear and Particle Physics Experiments, A How-to-Approach **2nd edition**, 141 (1994).

[38] O. H. Odland *et al.*, Nucl. Inst. and Meth. **A378**, 149 (1996).

[39] P. J. Sellin *et al.*, Nucl. Inst. and Meth. **A311**, 217 (1992).

[40] K. Rykaczewski *et al.*, Phys. Rev. **C60**, 011301R (1999).

[41] T. N. Ginter *et al.*, Phys. Rev. **C61**, 014308 (1999).

[42] J. C. Batchelder *et al.*, Phys. Rev. **C57**, 1042R (1998).

[43] J. C. Batchelder *et al.*, Nucl. Inst. and Meth. **B204**, 625 (2003).

[44] http://www.eurisysmesures.com .

[45] http://www.canberra.com .

[46] http://www.orteconline.com .

[47] http://www.xia.com .

[48] R. Grzywacz *et al.*, Nucl. Inst. and Meth. **B204**, 649 (2003).

[49] L. Westgard *et al.*, the ISOLDE collaboration, Bull. Am. Phys. Soc. **17**, 907 CB13 (1972).

[50] R. Beraud *et al.*, Centre de Publications de L'Universit/'e de Caen,France 3 (1988).

[51] M. N. Tantawy *et al.*, APS April meeting, Albuquerque NM (2002).

[52] C. R. Alvarez *et al.*, Phys. Rev. **C54**, 57 (1977).

[53] J. Deslauriers *et al.*, Z. Phys. **A283**, 33 (1977).

[54] J. Gilat *et al.*, Phys. Rev. **C40**, 2249 (1989).

[55] W. Nazarewicz *et al.*, Nucl. Phys. **A503**, 285 (1989).

[56] R. B. Firestone, Table of Isotopes (2001).

[57] N. Redon *et al.*, Z. Phys. **A306**, 223 (1982).

[58] K. Rykaczewski *et al.*, Phys. Rev. **C60**, 011301R (1999).

[59] P. Möller *et al.*, At. Data Nucl. Data Tables **59**, 185 (1995).

[60] D. Seweryniak *et al.*, Nucl. Phys. **A682**, 274c (2001).

[61] K. S. Vierinen *et al.*, Phys. Rev. **C39**, 1972 (1989).

[62] K. Livingston *et al.*, Phys. Lett. **B312**, 46 (1993).

[63] D.Seweryniak *et al.*, Phys. Rev. **C55**, R2137 (1997).

[64] L. Grodzins *et al.*, Phys. Lett **2**, 438 (1972).

[65] S. Raman *et al.*, At. Data Nucl. Data Tables **78**, 1 (2001).

[66] R. Broda *et al.*, Z. Phys. **A334**, 11 (1989).

[67] J. R. B. Oliveira *et al.*, Phys. Rev. **C62**, 064301 (2000).

[68] D.Seweryniak *et al.*, Eur. Phys. J. **A25**, s01, 159 (2005).

[69] A. P. Robinson *et al.*, AIP Conf. Proc. **764**, 217 (2005).

[70] A. P. Robinson *et al.*, Eur. Phys. J. **A25**, s01, 155 (2005).

[71] P. Möller *et al.*, At. Data Nucl. Data Tables **66**, 131 (1997).

Vita

Mohammed N. Tantawy, born on October 4th, 1974, graduated from Mutah University with a Bachelor of Science degree majoring in Physics in the fall of 1995. He went on to study at the graduate school at the University of Jordan and received a graduate diploma in Medical Physics in the summer of 1998. He worked at a variety of hospitals during that period. In 1999, Mohammed Tantawy began his studies at the University of Tennessee, Knoxville, in pursuit of a PhD in experimental nuclear physics. He worked as a graduate teaching assistant for the Department of Physics and Astronomy at the University of Tennessee in Knoxville for the first part of his graduate years. His research took place at Oak Ridge National Laboratory where he gained a wealth of knowledge in the experimental field through the help of the HRIBF staff. He received his Doctor of Philosophy degree in the fall of 2005.

In the future, Mohammed Tantawy hopes to continue his path in science and study nuclei beyond the drip lines in the nuclear chart. He hopes to put his knowledge of the structure of the nuclei for good use.